Theory and Simulations of Time-Resolved X-Ray Scattering

Simmermacher, Mats

Publication date:
2018

Document Version
Publisher's PDF, also known as Version of record

PhD Thesis

Theory and Simulations
of
Time-Resolved X-Ray Scattering

written by
Mats Simmermacher

supervised by
Klaus B. Møller and Niels E. Henriksen

Department of Chemistry
Technical University of Denmark
2800 Kongens Lyngby
Denmark

July 2018

Abstract

Recent advances in the preparation of intense and ultrafast hard X-ray pulses permit the observation of dynamical changes in atoms and molecules in real time *via* non-resonant scattering. The analysis and interpretation of these experiments, however, require a sound and elaborate theoretical framework as well as advanced numerical simulations. In this doctoral thesis, the quantum electrodynamical description of time-resolved non-resonant X-ray scattering by atoms and molecules in non-stationary states is reviewed. A unified and coherent rederivation is presented. Different contributions to the scattering signal are identified and discussed. Particular attention is paid to inelastic scattering and to scattering related to electronic coherences. A general analytic solution to one-electron scattering matrix elements of the hydrogen atom is derived. These solutions allow a computationally efficient and mathematically exact evaluation of the X-ray scattering signal of the atom in any non-stationary state.

Based on the developed framework, the time-resolved X-ray scattering signals of two systems are simulated.

First, the analytic solutions are applied to an electronic wave packet of the hydrogen atom. Previously published results that involved numerical integration are reproduced. It is shown that the time-dependence of the scattering signal stems solely from the contributions related to the electronic coherence, whereas the elastic and inelastic signals are independent of time. The effect of the pulse duration on the X-ray scattering signal is revised and explained differently than in the published work. It is shown that the existence of an optimum pulse duration at which the scattering signal displays the strongest time-dependence is entirely due to a restriction on the range of photon energies that are accepted by the detector.

Second, the scattering signal of the hydrogen molecule subsequent to UV excitation from its $X^1\Sigma_g^+$ ground state to its $B^1\Sigma_u^+$ excited state is simulated. To the best of the author's knowledge, this is the first full simulation of two-dimensional time-resolved X-ray scattering patterns of a molecule. All contributions to the scattering signal are evaluated. The separability of the contribution related to the electronic coherence from the total scattering signal is discussed.

Resume

Nylige fremskridt i genereringen af intense og ultrakorte hårde røntgenpulser muliggør tidsopløste iagttagelser af dynamiske forandringer i atomer og molekyler ved hjælp af ikke-resonant spredning. Analysen og fortolkningen af disse eksperimenter kræver en velfunderet og detaljeret teoretisk ramme samt avancerede numeriske simulationer. I denne ph.d.-afhandling bliver den kvanteelektrodynamiske beskrivelse af tidsopløst, ikke-resonant røntgenspredning fra atomer og molekyler i ikke-stationære tilstande drøftet. En forenet og sammenhængende genudledning bliver præsenteret. De forskellige bidrag til spredningssignalet bliver identificeret og diskuteret. Særlig opmærksomhed bliver lagt på uelastisk spredning og på spredning i sammenhængen med kohærenser imellem elektroniske tilstande. En generel analytisk løsning af en-elektron spredningsmatrixelementer af brintatomet bliver udledt. Disse løsninger muliggør en beregningsmæssig effektiv og matematisk eksakt evaluering af røntgenspredningssignalet af atomet i en ikke-stationær tilstand.

Baseret på den udledte teoretiske ramme bliver de tidsopløste røntgenspredningssignaler fra to systemer simuleret.

Først anvendes de analytiske løsninger til en elektronisk bølgepakke af brintatomet. Tidligere offentliggjorte resultater, som involverede numerisk integration, bliver reproduceret. Der vises, at tidsafhængigheden af spredningssignalet udelukket stammer fra bidragene, som er relateret til kohærenser imellem elektroniske tilstande, hvorimod de elastiske og uelastiske signaler er tidsuafhængige. Den effekt, pulsvarigheden har på røntgenspredningssignalet, bliver revideret og forklares på en anden måde end i den tidligere publikation. Der vises, at eksistensen af en optimal pulsvarighed, for hvilken spredningssignalet udviser den største tidsafhængighed, udelukkende kan tilbageføres til en begrænsning af fotonenergierne, som observeres af detektoren.

Dernæst bliver spredningssignalet af brintmolekylet efterfølgende UV excitationen fra dens $X^1\Sigma_g^+$ grundtilstand til dens $B^1\Sigma_u^+$ exciterede tilstand simuleret. Efter forfatterens bedste overbevisning er dette den første komplette simulation af todimensionelle, tidsopløste røntgenspredningsmønstre fra et molekyle. Alle bidrag til spredningssignalet bliver evalueret. Der

bliver diskuteret, hvorvidt kohærensbidraget kan adskilles fra det totale spredningssignal.

Preface

This doctoral thesis has been submitted to the Department of Chemistry at the Technical University of Denmark in partial fulfilment of the requirements to receive a PhD degree in the subject of Chemistry. The work presented herein was carried out by me at the Department of Chemistry at the Technical University of Denmark from April 2015 to July 2018 under supervision of Klaus B. Møller and co-supervision of Niels E. Henriksen. In addition, parts of the work were done during several research stays at the School of Chemistry at the University of Edinburgh in the group of Adam Kirrander in October 2016, in April and May 2017, and from January until April 2018.

Copenhagen, July 2018

Mats Simmermacher

Acknowledgements

This work would never have been possible without the vast support and inspiration I received from others. Sincere thanks are particularly given to the following people:

- ◇ to my supervisors **Klaus B. Møller** and **Niels E. Henriksen** for giving me the opportunity to learn from them, for their openness to my interests, for their encouragement, support, and trust, as well as for their instructive and inspiring perspectives and advice
- ◇ to **Adam Kirrander** for repeatedly welcoming me in his group, for his kindness and matchless hospitality, for his enthusiasm, as well as for his ideas and a productive, ongoing collaboration
- ◇ to **Andrés M. Carrascosa** for his collegiality and friendship, for a stimulating and fruitful teamwork, for the impressive work on his code, as well as for numerous calculations of scattering matrix elements
- ◇ to **Mátyas I. Pápai** for his company, support, and friendship, for our collaboration, for granting me asylum in his flat when I had no place to stay, as well as for our versatile discussions and our daily *kávé idő*
- ◇ to **Ildikó Pápai** for her friendship, for granting me asylum in her flat when I had no place to stay, as well as for her pharmaceutical advice
- ◇ to my amiable and talented colleagues at the Technical University of Denmark **Gianluca Levi**, **Asmus O. Dohn**, **Mostafa Abedi**, **Esben F. Thomas**, **Xusong Li**, **Alexandre P. Voute**, **Marta L. Vidal**, and **Rasmus Faber** for their company, for discussions that broadened my horizon, as well as for their friendships
- ◇ to my amiable and talented colleagues at the University of Edinburgh **Nikola Zotev**, **Darren Bellshaw**, **Minas Stefanou**, and **Haiwang Yong** for their company, for discussions that broadened my horizon, as well as for their friendships

- to all members of the Staff at DTU Chemistry, most notably to **Erling H. Stenby**, **Sonia Coriani**, **Kasper P. Kepp**, **Jingdong Zhang**, **Mette Hansen**, and **Betina M. F. Roesdahl** for creating a great working atmosphere as well as for plenty of other reasons I cannot all name by themselves
- to the HPC-Europa3 team at the EPCC, in particular to **Weronika Filinger**, **Catherine Inglis**, and **Mario Antonioletti** for their hospitality and support
- to **Elke Faßhauer** for her belief in me, for her emotional support, for her patience, for her critical feedback on my research, for her scientific advice, as well as for "covering 100 pages with red ink"
- to **Dietrich Krebs** for his long-lasting friendship, for his interest in my research, my progress, and my general well-being, for his critical feedback on my research, as well as for several prolific discussions
- to my former Master's supervisor **Stephan P. A. Sauer** for his ongoing interest in my work and career as well as for the advice he has given me on different occasions
- to my mother and stepfather **Cornelia** and **Fred Radtke** for their emotional support and encouragement, for their appreciation of higher education, as well as for our recreational sailing holidays
- to my father and stepmother **Henner** and **Anja Simmermacher** for their emotional support and encouragement as well as for their appreciation of higher education
- to my grandparents **Bruno** and **Ursula Schmedemann** for their emotional support and encouragement, for their appreciation of higher education, as well as for the positive influence they have on me

I furthermore acknowledge the financial support I have received from the **Department of Chemistry** at the **Technical University of Denmark** and from the **HPC-Europa3 Transnational Access Programme**.

Publications

The theoretical framework of time-resolved X-ray scattering by atoms in non-stationary states discussed in section 2, the analytic solution to the one-electron scattering matrix elements of the hydrogen atom derived in section 6, and the simulation presented in section 7 led to the publication of the manuscript:

- **M. Simmermacher**, N. E. Henriksen, and K. B. Møller, *Time-resolved X-ray scattering by electronic wave packets: analytic solutions to the hydrogen atom*, Phys. Chem. Chem. Phys. **19**, 19740 (2017).

The theoretical framework of time-resolved X-ray scattering by molecules in non-stationary states discussed in section 3, the properties of the one-electron scattering matrix elements scrutinised in section 5, and the simulation presented in section 8 led to the preparation of two manuscripts that will be submitted soon:

- **M. Simmermacher**, A. M. Carrascosa, A. Kirrander, N. E. Henriksen, and K. B. Møller, *Electronic coherence in ultrafast x-ray scattering from molecular wavepackets*, submitted, (2018).
- A. M. Carrascosa, **M. Simmermacher**, N. E. Hendriksen, K. B. Møller, and A. Kirrander, *Evaluation of one- and two-electron scattering matrix elements in two dimensions*, to be submitted, (2018).

Additional work that is not discussed in this doctoral thesis led furthermore to the publication of the manuscript:

- M. Pápai, **M. Simmermacher**, T. J. Penfold, K. B. Møller, and T. Rozgonyi, *How to Excite Nuclear Wavepackets into Electronically Degenerate States in Spin-Vibronic Quantum Dynamics Simulations*, J. Chem. Theory Comput. **14**, 3967 (2018).

Contents

Introduction

A century after Max von Laue was awarded the Nobel Prize in Physics "for his discovery of the diffraction of X-rays by crystals" [1] and William and Lawrence Bragg were honoured "for their services in the analysis of crystal structure by means of X-rays" [2], novel sources of X-rays permit experiments neither von Laue nor one of his contemporaries could have dreamt of. In comparison to conventional X-ray tubes that are used since their times, modern X-Ray Free-Electron Lasers (XFELs) provide a peak brilliance that is more than 20 orders of magnitude larger. The radiation XFELs emit is furthermore pulsed and durations of less than 100 fs are currently available. [3–6] X-ray scattering is therefore no longer confined to the determination of static structures of crystalline matter. Due to the large brilliance of XFELs it is now possible to conduct experiments with dilute samples of molecules in the liquid or gas phase where the intensity of the scattering signal is not enhanced by constructive interference as in Bragg diffraction by periodic systems. Moreover, the ultrafast pulses allow an investigation of structural changes and chemical reactions in real time, since nuclear motion in molecules typically occurs on a timescale of tenths or hundreds of femtoseconds. [7–15] In addition, even faster electronic motion may be tracked in the future, because a further decrease of the pulse duration to attoseconds at XFELs seems possible [16–19].

In one remarkable example of these experiments, non-resonant scattering of hard X-rays from the Linac Coherent Light Source [3], an American XFEL that started commissioning in 2009, were used to identify reaction paths of the electrocyclic ring-opening of 1,3-cyclohexadiene to 1,3,5-hexatriene. [8,9] Time-resolved X-ray scattering thus proved to provide insights into chemical reaction mechanisms. These insights are complementary to the information accessible *via* spectroscopy which addresses transitions between states. [14,20]

In these scattering experiments a target, generally referred to as the material system, interacts with two subsequent pulses of electromagnetic radiation. The pulses are called the pump and the probe pulse, respectively. The pump pulse excites the material system and thereby induces dynamics such as photoinduced chemical reactions or photophysical relaxation processes. The probe pulse, which has a mean photon energy in the hard X-ray regime,

is scattered by the non-stationary material system onto a detector. By variation of the pump-probe delay, *i.e.* the time the probe pulse lags behind the pump pulse, the scattering signal is measured at different points in time. The resulting series of the snapshots contains time-resolved information about the dynamics invoked by the pump pulse.

Extracting the desired information from the experimental data is a non-trivial task, though. Inversion procedures that transform the scattering signal directly into the one-electron density and thereby reveal the molecular structure rely on rough approximations such as the independent atom model and its underlying assumption that the signal is purely elastic.[21–23] Inelastic scattering that involves a transfer of energy between the photons and the molecule is neglected. The validity of these approximations is questionable and not generally ensured. The elastic and the inelastic signals are usually inseparable and the inelastic contribution can be significant. It is furthermore impossible to account for any reorganisation of the one-electron density due to covalent bonding[24] or electronic excitation in the framework of the IAM. These aspects are briefly discussed in sections 3 and 8.

A particularly dramatic failure of the assumption that the scattering signal is purely elastic was demonstrated in a seminal paper by Dixit, Vendrell, and Santra.[25] The authors have shown that the scattering signal of an electronic wave packet in the hydrogen atom deviates substantially from from a signal that simply probes the time-dependent one-electron density. Their main results are reproduced, discussed, and partially reinterpreted in section 7. Different contributions to the scattering signals are identified and additional insights are provided.

The fact that no generally applicable direct inversion procedure is available necessitates that time-resolved scattering experiments are accompanied by advanced numerical simulations. It is likely that the desired information about the dynamics of the material system can be obtained only by comparison of the experimental and the simulated data. A strictly empirical analysis and interpretation of the experiments without such *in silico* support seems impossible. The simulations, in turn, require a sound and elaborate theoretical framework to be based upon.

Pioneering work that addressed the theoretical description of time-resolved X-ray scattering was published by Wilson *et al.* already in the 1990s.[21,26,27] Without explicitly treating the X-ray pulse and its interaction with the material system in terms of electrodynamics, the authors have extended the theory of conventional static scattering to the case of time-dependent states. Remarkably, their approach led to equations very similar to those obtained by more recent and fundamental derivations. Most notably, Cao and Wilson could distinguish the three contributions to the scattering signal in their expressions: elastic scattering, inelastic scattering, and scattering

related to electronic coherences.[21] These contributions are also identified in sections 2 and 3 where they are discussed in greater detail.

In 2002, Bratos *et al.* discussed time-resolved X-ray scattering by incorporating the X-ray pulse in terms of classical electrodynamics.[28] Six years later, Henriksen and Møller provided a fully quantised description by use of quantum electrodynamics.[29] They were the first who accounted for the quantum natures of both the material system and the X-ray pulse. In three other publications, the authors reviewed and further simplified their expressions.[22,23,30] The theory that is derived in Part I follows their approach.

The above-mentioned paper by Dixit *et al.* also utilised quantum electrodynamics and showed the first simulation of a time-resolved X-ray scattering experiment that fully employed the quantum description.[25] In a similar study a year later, Dixit and Santra computed the scattering patterns of an electronic wave packet of decoupled electrons in the helium atom.[31]

Most recently, Mukamel *et al.* calculated the X-ray scattering signal of sodium fluoride subsequent to UV excitation from its $X^1\Sigma$ ground state to its $A^1\Sigma$ excited state.[32,33] Both states were non-adiabatically coupled in a narrow range of interatomic distances around an avoided crossing. When the nuclear wave packet on the excited state potential passed through the avoided crossing, a short-lived electronic coherence was created that led to a distinct contribution to the scattering signal. The authors thus demonstrated that time-resolved X-ray scattering can carry signatures of electronic coherences or non-adiabatically coupled avoided crossings. Mukamel *et al.* considered only the two electronic states already occupied by the wave packet. Inelastic scattering to other bound states was neglected both in their simulations and in their formalism. The scattering signal was furthermore reduced to a single dimension in reciprocal space. Two-dimensional scattering patterns were not presented and the question whether the signatures of the electronic coherences were visible in or even separable from the total scattering signal remained untouched. These aspects require further investigation and are addressed in the simulation presented in section 7.

Despite the effort and all important contributions that have been made so far, various aspects of the theory of time-resolved X-ray scattering remain opaque. A recent debate about heterodyne interferences in the scattering signal of photoexcited molecules in the gas phase revealed that even key aspects of time-resolved X-ray scattering were misunderstood.[33–37] It is therefore necessary that the theory is discussed in greater detail and that the nature and meaning of the different contributions to the scattering signal are illustrated by further simulations.

In this regard the theoretical framework of Henriksen and Møller[22,23,29,30] is reviewed in Part I. A unified and coherent rederivation of their expressions is presented. Various elements that were not or only briefly explicated in

the published literature are explained in detail. Section 1 introduces the differential scattering signal which is the key quantity that is measured in X-ray scattering experiments. An expression for a general material system is derived. In sections 2 and 3 this expression is further simplified for non-stationary states in atoms and molecules, respectively. Scattering matrix elements are introduced, different contributions to the scattering signal are identified, and several aspects and consequences are discussed.

Part II deals with technical issues that facilitate the evaluation of one-electron scattering matrix elements and thus the simulation of differential scattering signals. Section 4 provides geometric relations of the coordinates in reciprocal space which are the arguments of the scattering matrix elements and of the scattering signal itself. In section 5 three important properties of the matrix elements which are used in the simulations later on are scrutinised. In section 6 an analytic approach for a computationally efficient and mathematically exact evaluation of one-electron scattering matrix elements of the hydrogen atom is derived. A formula published by Schnaidt in 1934 [38] that yields analytic solutions to matrix elements that involve the $1s$ ground state is generalised to any combination of eigenstates of the hydrogen atom.

Part III presents two extensive simulations of time-resolved X-ray scattering where all contributions to the differential scattering signal are considered.

In section 7 the results of Dixit, Vendrell, and Santra [25] are reproduced within the theoretical framework of sections 1 and 2 and by means of the analytic approach derived in section 6. Thereby, the general equivalence of the formalisms published by Dixit *et al.* and by Henriksen and Møller as well as the applicability of the analytic approach are illustrated. Moreover, the fundamental expressions are simplified further than in the published literature which permits a more transparent presentation that is possibly easier to comprehend. The three contributions to the scattering signal that were already identified by Cao and Wilson [21] are discussed individually. Finally, the effect of the pulse duration on the scattering signal is revised and an explanation that deviates from the one of Dixit *et al.* is given.

A simulation of the differential scattering signal of the hydrogen molecule subsequent to UV excitation from its $X^1\Sigma_g^+$ ground state to its $B^1\Sigma_u^+$ excited state is presented in section 8. It is, to the best of my knowledge, the first full simulation of time-resolved X-ray scattering by a molecule. All contributions to the scattering signal are evaluated and more electronic states than just the two occupied by the wave packet are taken into account. Two-dimensional scattering patterns are displayed and the separability of the contribution from the electronic coherence is discussed. Section 8 provides insights that extend the seminal work by Mukamel *et al.* and foster the understanding of time-resolved X-ray scattering by molecules.

Part I

Theory of Time-Resolved X-Ray Scattering

The theoretical framework of time-resolved non-resonant X-ray scattering that was developed in several publications by Henriksen and Møller [22,23,29,30] is reviewed in this Part. A unified and coherent rederivation of their expressions is presented. Various elements that were not or only briefly explicated in the published literature are explained in detail. The expressions serve as a basis for the simulations presented in Part III.

Section 1 introduces the differential scattering signal $dS/d\Omega$ which is the key quantity that is measured in X-ray scattering experiments. An expression for a general material system is derived. In sections 2 and 3 this expression is further simplified for non-stationary states in atoms and molecules, respectively. Scattering matrix elements are introduced, different contributions to the scattering signal are identified, and several aspects and consequences are discussed.

1 Scattering by General Material Systems

In time-resolved non-resonant X-ray scattering experiments the differential scattering signal $dS/d\Omega$ is measured. It refers to the number of scattered photons per solid angle Ω. In this section an expression for the differential scattering signal by a general material system is derived.

Subsection 1.1 provides the basic equations that describe the differential scattering signal in terms of first-order perturbation theory. In subsection 1.2 the quantum states of the incident and scattered X-ray photons are discussed. Theses states are used in subsection 1.3 to derive the perturbation operator that couples the X-ray photons to the material system. With the perturbation operator, the expression for the differential scattering signal is further simplified in subsection 1.4

1.1 Scattering in First-Order Perturbation Theory

In the framework first-order perturbation theory [29,39–42], the differential scattering signal $dS/d\Omega$ can be expressed as:

$$\frac{dS}{d\Omega} = \int_0^{+\infty} \rho(\omega_{\boldsymbol{k}_\mathrm{s}}) \lim_{t\to\infty} \left\langle \Psi^{(1)}(t) \,\middle|\, \Psi^{(1)}(t) \right\rangle d\omega_{\boldsymbol{k}_\mathrm{s}}. \tag{1.1}$$

Equation (1.1) contains the angular frequency of the scattered photons $\omega_{\boldsymbol{k}_\mathrm{s}}$ and their density of states:

$$\rho(\omega_{\boldsymbol{k}_\mathrm{s}}) = \frac{\omega_{\boldsymbol{k}_\mathrm{s}}^2 V}{8\pi^3 c^3}, \tag{1.2}$$

where c is the speed of light and V is an artificial quantity that is used in the quantum electrodynamical treatment of the electric X-ray field. It is the finite volume in which the electric field is quantised, therefore termed quantisation volume.

Equation (1.1) also contains the time-dependent first-order wave function $\left|\Psi^{(1)}(t)\right\rangle$ of the material system coupled to the photons. The limit of the matrix element as t approaches infinity ensures that the interaction with the entire X-ray pulse is taken into account. The expression is integrated over the angular frequencies $\omega_{\boldsymbol{k}_\mathrm{s}}$ to include scattered photons at all energies $\hbar\omega_{\boldsymbol{k}_\mathrm{s}}$. In the framework of time-dependent perturbation theory [39,40,43], the coupling of the material system and the electric X-ray field can be described by the first-order correction to the unperturbed time-dependent wave function of the material system $\left|\Psi(t)\right\rangle$:

$$\left|\Psi^{(1)}(t)\right\rangle = -\frac{\iota}{\hbar} \cdot \int_{-\infty}^{t} \hat{U}(t,t')\, \hat{O}(t') \left|\Psi(t')\right\rangle dt'. \tag{1.3}$$

Equation (1.3) contains the imaginary unit ι, the time-evolution operator $\hat{U}(t,t') = \exp\left[-\iota\hat{H}_\mathrm{M}(t-t')/\hbar\right]$ where $\hat{H}_\mathrm{M}$ is the time-independent field-free Hamiltonian of the unperturbed material system, as well as the perturbation described by the operator $\hat{O}(t)$. In case of non-resonant X-ray scattering, $\hat{O}(t)$ is the matrix element of the interaction Hamiltonian $\hat{H}_\mathrm{int}(t)$ and the states of the incident and scattered photons $\left|\psi_{u\boldsymbol{k}_0}\right\rangle$ and $\left|\psi_{v\boldsymbol{k}_\mathrm{s}}\right\rangle$, respectively:

$$\hat{O}(t) = \left\langle \psi_{v\boldsymbol{k}_\mathrm{s}} \,\middle|\, \hat{H}_\mathrm{int}(t) \,\middle|\, \psi_{u\boldsymbol{k}_0} \right\rangle. \tag{1.4}$$

The matrix element in equation (1.4) couples the states of the incident and the scattered radiation *via* interaction with the material system. In the scheme of minimal coupling and Coulomb gauge, $\hat{H}_\mathrm{int}(t)$ is:

$$\hat{H}_{\mathrm{int}}(t) = \sum_{\alpha} \left(\frac{q_\alpha^2}{2m_\alpha}\, \hat{\boldsymbol{A}}^2(\boldsymbol{r}_\alpha, t) + \frac{\hbar q_\alpha}{\iota m_\alpha}\, \hat{\nabla}_{\boldsymbol{r}_\alpha}\, \hat{\boldsymbol{A}}(\boldsymbol{r}_\alpha, t) \right). \tag{1.5}$$

The sum in equation (1.5) runs over all charged particles of the material system with their corresponding charge q_α and mass m_α. $\hbar = h/(2\pi)$ is the reduced Planck constant. The operator $\hat{\nabla}_{\boldsymbol{r}_\alpha}$ denotes the derivative with respect to the coordinates of the particle with index α and $\hat{\boldsymbol{A}}(\boldsymbol{r}_\alpha, t)$ is the operator of the quantised vector potential of the X-ray radiation at position $\boldsymbol{r}_\alpha$ and time t. In terms of plane waves, $\hat{\boldsymbol{A}}(\boldsymbol{r}_\alpha, t)$ is given as[39,41,44,45]:

$$\begin{aligned} \hat{\boldsymbol{A}}(\boldsymbol{r}, t) &= \hat{\boldsymbol{A}}^{(+)}(\boldsymbol{r}, t) + \hat{\boldsymbol{A}}^{(-)}(\boldsymbol{r}, t) \\ &= \sum_{u} \sum_{\boldsymbol{k}} \sqrt{\frac{\hbar}{2\epsilon_0 V \omega_{\boldsymbol{k}}}} \cdot \Big(\boldsymbol{\epsilon}_u\, \hat{a}_{u\boldsymbol{k}}\, e^{\iota(\boldsymbol{k}\cdot\boldsymbol{r} - \omega_{\boldsymbol{k}} t)} \\ &\qquad + \boldsymbol{\epsilon}_u^*\, \hat{a}_{u\boldsymbol{k}}^\dagger\, e^{-\iota(\boldsymbol{k}\cdot\boldsymbol{r} - \omega_{\boldsymbol{k}} t)} \Big). \end{aligned} \tag{1.6}$$

The sums in equation (1.6) refer to the polarisation u and the wave vector $\boldsymbol{k}$ of the quantised X-ray field modes. $\boldsymbol{\epsilon}_u$ and $\omega_{\boldsymbol{k}}$ denote the polarisation vector and angular frequency of a particular mode, respectively. The quantity ϵ_0 is the vacuum permittivity and V the quantisation volume. $\hat{a}_{u\boldsymbol{k}}^\dagger$ and $\hat{a}_{u\boldsymbol{k}}$ are bosonic creation and annihilation operators. They create or annihilate X-ray quanta in their corresponding field modes.

1.2 Quantisation of X-Rays

As equation (1.4) already implies, every non-resonant X-ray scattering event can be understood as a transfer of a photon from its initial state $\left|\psi_{u\boldsymbol{k}_0}\right\rangle$ to another state $\left|\psi_{v\boldsymbol{k}_\mathrm{s}}\right\rangle$. For convenience, it can be assumed that both states are single-photon states and that no photon is in $\left|\psi_{v\boldsymbol{k}_\mathrm{s}}\right\rangle$ initially. The scattered photon is thus described by a simple single-photon number state:

$$\left|\psi_{v\boldsymbol{k}_\mathrm{s}}\right\rangle = \left|v\boldsymbol{k}_\mathrm{s}\right\rangle = \hat{a}_{v\boldsymbol{k}_\mathrm{s}}^\dagger \left|\mathrm{vac}\right\rangle. \tag{1.7}$$

The vector $\left|\mathrm{vac}\right\rangle$ in equation (1.7) is the vacuum state that contains zero photons. By action of $\hat{a}_{v\boldsymbol{k}_\mathrm{s}}^\dagger$ upon $\left|\mathrm{vac}\right\rangle$, a photon in state $\left|v\boldsymbol{k}_\mathrm{s}\right\rangle$ is created.

The state of the incident X-ray photon $\left|\psi_{u\boldsymbol{k}_0}\right\rangle$ should represent a pulse. It is shown in the following that a linearly polarised pulse can be expressed as a single-photon, multimode wave packet[44,46]:

$$\left|\psi_{u\boldsymbol{k}_0}\right\rangle = \sum_k \; c_{k-k_0} \; \left|u\boldsymbol{k}\right\rangle = \sum_k \; c_{k-k_0} \; \hat{a}^\dagger_{u\boldsymbol{k}} \; \left|\mathrm{vac}\right\rangle. \tag{1.8}$$

The wave packet in equation (1.8) is a superposition of field modes $\left|u\boldsymbol{k}\right\rangle$ with the same polarisation vector $\boldsymbol{\epsilon}_u$ and the same direction of propagation but different angular frequencies $\omega_{\boldsymbol{k}} = kc$. The wave packet describes a polarised, polychromatic pulse of electromagnetic radiation. The coefficients c_{k-k_0} define the distribution of the photon over its superposed modes $\left|u\boldsymbol{k}\right\rangle$. The distribution is peaked at $k = k_0$ and the absolute squares of its individual coefficients c_{k-k_0} add up to unity.

The wave packet is an eigenstate of the photon number operator $\hat{N}$[39,46]:

$$\begin{aligned}
\left\langle \psi_{u\boldsymbol{k}_0} \right| \hat{N} \left| \psi_{u\boldsymbol{k}_0} \right\rangle &= \left\langle \psi_{u\boldsymbol{k}_0} \right| \sum_u \sum_{\boldsymbol{k}} \; \hat{a}^\dagger_{u\boldsymbol{k}} \; \hat{a}_{u\boldsymbol{k}} \left| \psi_{u\boldsymbol{k}_0} \right\rangle \\
&= \sum_u \sum_{\boldsymbol{k}} \sum_{k'} \sum_{k''} \; c^*_{k'-k_0} \; c_{k''-k_0} \\
&\qquad \times \left\langle \mathrm{vac} \right| \; \hat{a}_{u'\boldsymbol{k}'} \; \hat{a}^\dagger_{u\boldsymbol{k}} \; \hat{a}_{u\boldsymbol{k}} \; \hat{a}^\dagger_{u'\boldsymbol{k}''} \; \left| \mathrm{vac} \right\rangle \\
&= \sum_u \sum_{\boldsymbol{k}} \sum_{k'} \sum_{k''} \; c^*_{k'-k_0} \; c_{k''-k_0} \; \delta_{uu'} \; \delta_{\boldsymbol{k}\boldsymbol{k}'} \; \delta_{\boldsymbol{k}\boldsymbol{k}''} \\
&= \sum_k \; \left| c_{k-k_0} \right|^2 = 1,
\end{aligned} \tag{1.9}$$

with eigenvalue 1, meaning that the wave packet in equation (1.8) is indeed a single-photon state. The matrix element $\left\langle \mathrm{vac} \right| \; \hat{a}_{u'\boldsymbol{k}'} \; \hat{a}^\dagger_{u\boldsymbol{k}} \; \hat{a}_{u\boldsymbol{k}} \; \hat{a}^\dagger_{u'\boldsymbol{k}''} \; \left| \mathrm{vac} \right\rangle$ in the third line of equation (1.9) is easily evaluated by application of Wick's theorem, using the bosonic commutation relation:

$$\hat{a}_{u'\boldsymbol{k}'} \; \hat{a}^\dagger_{u\boldsymbol{k}} = \hat{a}^\dagger_{u\boldsymbol{k}} \; \hat{a}_{u'\boldsymbol{k}'} + \delta_{uu'} \; \delta_{\boldsymbol{k}\boldsymbol{k}'}, \tag{1.10}$$

where $\delta_{uu'}$ and $\delta_{\boldsymbol{k}\boldsymbol{k}'}$ are Kronecker deltas. Moreover, matrix elements in which a creation operator $\hat{a}^\dagger_{u\boldsymbol{k}}$ acts directly to the left upon $\left\langle \mathrm{vac} \right|$ vanish, since they imply that a non-existing field mode in the vacuum state is annihilated.

The expectation value of the single counting rate or light intensity operator $\hat{I}(\boldsymbol{r}, t) = \hat{\boldsymbol{E}}^{(-)}(\boldsymbol{r}, t) \cdot \hat{\boldsymbol{E}}^{(+)}(\boldsymbol{r}, t)$ yields the absolute square of the field strength of the wave packet at a particular coordinate $\boldsymbol{r}$ and time t.[44–46] The operators $\hat{\boldsymbol{E}}^{(-)}(\boldsymbol{r}, t)$ and $\hat{\boldsymbol{E}}^{(+)}(\boldsymbol{r}, t)$ are the positive and negative frequency components of the electric field operator $\hat{\boldsymbol{E}}(\boldsymbol{r}, t)$ in the Heisenberg picture. In Coulomb gauge and in the absence of charged particles, $\hat{\boldsymbol{E}}(\boldsymbol{r}, t)$ is related to the operator of the vector potential $\hat{\boldsymbol{A}}(\boldsymbol{r}, t)$ in equation (1.6) by:

$$\begin{aligned}\hat{\boldsymbol{E}}(\boldsymbol{r},t) &= -\frac{\partial}{\partial t}\,\hat{\boldsymbol{A}}(\boldsymbol{r},t) = \hat{\boldsymbol{E}}^{(+)}(\boldsymbol{r},t) + \hat{\boldsymbol{E}}^{(-)}(\boldsymbol{r},t) \\ &= \iota \cdot \sum_{u}\sum_{\boldsymbol{k}} \sqrt{\frac{\hbar\omega_{\boldsymbol{k}}}{2\epsilon_0 V}} \cdot \Big(\boldsymbol{\epsilon}_u\ \hat{a}_{u\boldsymbol{k}}\ e^{\iota(\boldsymbol{k}\cdot\boldsymbol{r}-\omega_{\boldsymbol{k}}t)} \\ &\qquad\qquad - \boldsymbol{\epsilon}_u^*\ \hat{a}_{u\boldsymbol{k}}^\dagger\ e^{-\iota(\boldsymbol{k}\cdot\boldsymbol{r}-\omega_{\boldsymbol{k}}t)} \Big).\end{aligned} \tag{1.11}$$

Hence, the light intensity operator is:

$$\hat{I}(\boldsymbol{r},t) = \sum_{u}\sum_{u'}\sum_{\boldsymbol{k}}\sum_{\boldsymbol{k}'}\ \mathcal{E}_{uu'\boldsymbol{k}\boldsymbol{k}'}(\boldsymbol{r},t)\ \hat{a}_{u\boldsymbol{k}}^\dagger\ \hat{a}_{u'\boldsymbol{k}'}, \tag{1.12}$$

where

$$\mathcal{E}_{uu'\boldsymbol{k}\boldsymbol{k}'}(\boldsymbol{r},t) = \frac{\hbar}{2\epsilon_0 V}\ \sqrt{\omega_{\boldsymbol{k}}\ \omega_{\boldsymbol{k}'}}\ \boldsymbol{\epsilon}_u^* \cdot \boldsymbol{\epsilon}_{u'}\ e^{-\iota(\boldsymbol{k}\cdot\boldsymbol{r}-\omega_{\boldsymbol{k}}t)}\ e^{\iota(\boldsymbol{k}'\cdot\boldsymbol{r}-\omega_{\boldsymbol{k}'}t)}. \tag{1.13}$$

With equation (1.12), the intensity of the incident X-ray pulse described by the multimode wave packet defined in equation (1.8) is given as:

$$\begin{aligned} I_E(\boldsymbol{r},t) &= \left\langle \psi_{u\boldsymbol{k}_0} \,\middle|\, \hat{I}(\boldsymbol{r},t) \,\middle|\, \psi_{u\boldsymbol{k}_0} \right\rangle \\ &= \sum_{u}\sum_{u'}\sum_{\boldsymbol{k}}\sum_{\boldsymbol{k}'}\ \mathcal{E}_{uu'\boldsymbol{k}\boldsymbol{k}'}(\boldsymbol{r},t) \cdot \left\langle \psi_{u\boldsymbol{k}_0} \,\middle|\, \hat{a}_{u\boldsymbol{k}}^\dagger\ \hat{a}_{u'\boldsymbol{k}'} \,\middle|\, \psi_{u\boldsymbol{k}_0} \right\rangle \\ &= \sum_{u}\sum_{u'}\sum_{\boldsymbol{k}}\sum_{\boldsymbol{k}'}\sum_{k''}\sum_{k'''}\ \mathcal{E}_{uu'\boldsymbol{k}\boldsymbol{k}'}(\boldsymbol{r},t)\ c_{k''-k_0}^*\ c_{k'''-k_0} \\ &\quad \times \left\langle \mathrm{vac} \,\middle|\, \hat{a}_{u''\boldsymbol{k}''}\ \hat{a}_{u\boldsymbol{k}}^\dagger\ \hat{a}_{u'\boldsymbol{k}'}\ \hat{a}_{u''\boldsymbol{k}'''}^\dagger \,\middle|\, \mathrm{vac} \right\rangle \\ &= \sum_{u}\sum_{u'}\sum_{\boldsymbol{k}}\sum_{\boldsymbol{k}'}\sum_{k''}\sum_{k'''}\ \mathcal{E}_{uu'\boldsymbol{k}\boldsymbol{k}'}(\boldsymbol{r},t)\ c_{k''-k_0}^*\ c_{k'''-k_0} \\ &\quad \times \delta_{uu''}\ \delta_{u'u''}\ \delta_{\boldsymbol{k}\boldsymbol{k}''}\ \delta_{\boldsymbol{k}'\boldsymbol{k}'''} \\ &= \sum_{k}\sum_{k'}\ \mathcal{E}_{uu\boldsymbol{k}\boldsymbol{k}'}(\boldsymbol{r},t)\ c_{k-k_0}^*\ c_{k'-k_0}. \end{aligned} \tag{1.14}$$

Insertion of equation (1.13) into equation (1.14) yields:

$$\begin{aligned} I_E(\boldsymbol{r},t) &= \frac{\hbar}{2\epsilon_0 V} \cdot \sum_{k}\sum_{k'}\ \sqrt{\omega_{\boldsymbol{k}}\ \omega_{\boldsymbol{k}}'}\ \boldsymbol{\epsilon}_u^* \cdot \boldsymbol{\epsilon}_u\ c_{k-k_0}^*\ c_{k'-k_0} \\ &\qquad\qquad \times e^{-\iota(\boldsymbol{k}\cdot\boldsymbol{r}-\omega_{\boldsymbol{k}}t)}\ e^{\iota(\boldsymbol{k}'\cdot\boldsymbol{r}-\omega_{\boldsymbol{k}'}t)} \\ &= \frac{\hbar}{2\epsilon_0 V} \cdot \left| \sum_{k}\ \sqrt{\omega_{\boldsymbol{k}}}\ c_{k-k_0}\ e^{\iota(\boldsymbol{k}\cdot\boldsymbol{r}-\omega_{\boldsymbol{k}}t)} \right|^2. \end{aligned} \tag{1.15}$$

The inner product of the polarisation vectors $\boldsymbol{\epsilon}_u^* \cdot \boldsymbol{\epsilon}_u$ in the first line of equation (1.15) equals unity. The distribution c_{k-k_0} that is peaked at $k = k_0$ can be replaced with a distribution c_k that is peaked at $k = 0$ instead. This is done by the transformation $k = k' + k_0$ such that:

$$c_{k-k_0} = c_{k'}, \qquad \omega_{\boldsymbol{k}} = \omega_{\boldsymbol{k}'} + \omega_{\boldsymbol{k}_0}, \qquad \boldsymbol{k} = \boldsymbol{k}' + \boldsymbol{k}_0. \tag{1.16}$$

In contrast to k of c_{k-k_0} that refers directly to the angular frequency $\omega_{\boldsymbol{k}} = kc$ of the corresponding field mode, k' of $c_{k'}$ defines the deviation of $\omega_{\boldsymbol{k}}$ from $\omega_{\boldsymbol{k}_0}$. With the transformations in equation (1.16), equation (1.15) is modified to:

$$\begin{aligned} I_E(\boldsymbol{r},t) &= \frac{\hbar}{2\epsilon_0 V} \cdot \left| \sum_{k'} \sqrt{\omega_{\boldsymbol{k}'} + \omega_{\boldsymbol{k}_0}}\; c_{k'}\; e^{\iota\left((\boldsymbol{k}'+\boldsymbol{k}_0)\cdot\boldsymbol{r} - (\omega_{\boldsymbol{k}'}+\omega_{\boldsymbol{k}_0})t\right)} \right|^2 \\ &= \frac{\hbar\omega_{\boldsymbol{k}_0}}{2\epsilon_0 V} \cdot \left| \sum_{k'} \sqrt{\frac{\omega_{\boldsymbol{k}'} + \omega_{\boldsymbol{k}_0}}{\omega_{\boldsymbol{k}_0}}}\; c_{k'}\; e^{\iota(\boldsymbol{k}'\cdot\boldsymbol{r} - \omega_{\boldsymbol{k}'}t)} \right|^2 . \end{aligned} \tag{1.17}$$

The amplitude of the classical electric field[46] $E_{\boldsymbol{k}_0} = \sqrt{\hbar\omega_{\boldsymbol{k}_0}/(2\epsilon_0 V)}$ can be identified in equation (1.17). Given that the distribution of frequencies around $\omega_{\boldsymbol{k}_0}$ is narrow so that $\omega_{\boldsymbol{k}} \ll \omega_{\boldsymbol{k}_0}$, the fraction $\sqrt{(\omega_{\boldsymbol{k}'} + \omega_{\boldsymbol{k}_0})/\omega_{\boldsymbol{k}_0}}$ can be approximated by unity. Renaming k' as k, the X-ray intensity is finally:

$$I_E(\boldsymbol{r},t) = E_{\boldsymbol{k}_0}^2 \cdot \left|h(\boldsymbol{r},t)\right|^2, \tag{1.18}$$

where $h(\boldsymbol{r},t)$ describes the electric field envelope of the pulse:

$$h(\boldsymbol{r},t) = \sum_k\; c_k\; e^{\iota(\boldsymbol{k}\cdot\boldsymbol{r} - \omega_{\boldsymbol{k}}t)}. \tag{1.19}$$

The envelope in equation (1.19) confirms that the wave packet $\left|\psi_{u\boldsymbol{k}_0}\right\rangle$ from equation (1.8) is indeed a pulse of electromagnetic radiation. Its field modes with angular frequencies $\omega_{\boldsymbol{k}}$ add up coherently and thereby allow the wave packet to move through space.

1.3 Perturbation Operator

Turning back to the perturbation operator $\hat{O}(t)$, insertion of the states $\left|\psi_{v\boldsymbol{k}_\mathrm{s}}\right\rangle$ and $\left|\psi_{u\boldsymbol{k}_0}\right\rangle$ from equations (1.7) and (1.8) into equation (1.4) yields:

$$\hat{O}(t) = \sum_k \; c_{k-k_0} \; \left\langle \mathrm{vac} \right| \; \hat{a}_{v\boldsymbol{k}_\mathrm{s}} \; \hat{H}_\mathrm{int}(t) \; \hat{a}^\dagger_{u\boldsymbol{k}} \; \left| \mathrm{vac} \right\rangle . \tag{1.20}$$

The second term of the interaction Hamiltonian $\hat{H}_\mathrm{int}(t)$ in equation (1.5), $\hat{\nabla}_{\boldsymbol{r}_\alpha} \; \hat{\boldsymbol{A}}(\boldsymbol{r}_\alpha, t)$, cannot contribute to the matrix element in equation (1.20), since only an equal number of creation and annihilation operators can lead to non-vanishing matrix elements. Moreover, non-resonant X-ray scattering requires a simultaneous creation and annihilation of photons as implied by $\hat{\boldsymbol{A}}^2(\boldsymbol{r}_\alpha, t)$. The contribution $\hat{\nabla}_{\boldsymbol{r}_\alpha} \; \hat{\boldsymbol{A}}(\boldsymbol{r}_\alpha, t)$, in contrast, refers to the absorption (annihilation) or emission (creation) of a photon and can be neglected in the hard X-ray regime of non-resonant scattering. (It is, however, essential in the case of resonant scattering.) Thus, only the $\hat{\boldsymbol{A}}^2(\boldsymbol{r}_\alpha, t)$ term of $\hat{H}_\mathrm{int}(t)$ has to be considered here and equation (1.20) becomes:

$$\hat{O}(t) = \sum_\alpha \sum_k \; c_{k-k_0} \; \frac{q_\alpha^2}{2m_\alpha} \; \left\langle v\boldsymbol{k}_\mathrm{s} \right| \; \hat{\boldsymbol{A}}^2(\boldsymbol{r}_\alpha, t) \; \left| u\boldsymbol{k} \right\rangle . \tag{1.21}$$

Following equation (1.6), the squared operator of the vector potential $\hat{\boldsymbol{A}}^2(\boldsymbol{r}_\alpha, t)$ in equation (1.21) equals the sum of four terms:

$$\begin{aligned} \hat{\boldsymbol{A}}^2(\boldsymbol{r}_\alpha, t) = {} & \hat{\boldsymbol{A}}^{(+)}(\boldsymbol{r}_\alpha, t) \cdot \hat{\boldsymbol{A}}^{(+)}(\boldsymbol{r}_\alpha, t) + \hat{\boldsymbol{A}}^{(-)}(\boldsymbol{r}_\alpha, t) \cdot \hat{\boldsymbol{A}}^{(-)}(\boldsymbol{r}_\alpha, t) \\ & + \hat{\boldsymbol{A}}^{(+)}(\boldsymbol{r}_\alpha, t) \cdot \hat{\boldsymbol{A}}^{(-)}(\boldsymbol{r}_\alpha, t) + \hat{\boldsymbol{A}}^{(-)}(\boldsymbol{r}_\alpha, t) \cdot \hat{\boldsymbol{A}}^{(+)}(\boldsymbol{r}_\alpha, t). \end{aligned} \tag{1.22}$$

The matrix elements of the two terms in the first line of equation (1.22) vanish due to unequal numbers of creation and annihilation operators. The matrix elements of the two remaining terms in the second line are equal, because bosonic states are symmetric under particle exchange, reflected by the fact that both $\hat{a}^\dagger_{u\boldsymbol{k}} \; \hat{a}_{u'\boldsymbol{k}'}$ and $\hat{a}_{u'\boldsymbol{k}'} \; \hat{a}^\dagger_{u\boldsymbol{k}}$ in equation (1.10) have the same sign. Hence, equation (1.21) becomes:

$$\begin{aligned} \hat{O}(t) = 2 \cdot \sum_\alpha \sum_k \; & c_{k-k_0} \; \frac{q_\alpha^2}{2m_\alpha} \\ & \times \left\langle v\boldsymbol{k}_\mathrm{s} \right| \; \hat{\boldsymbol{A}}^{(+)}(\boldsymbol{r}_\alpha, t) \cdot \hat{\boldsymbol{A}}^{(-)}(\boldsymbol{r}_\alpha, t) \; \left| u\boldsymbol{k} \right\rangle , \end{aligned} \tag{1.23}$$

which is:

$$\begin{aligned}\hat{O}(t) = 2 \cdot \sum_{\alpha} \sum_{u'} \sum_{u''} \sum_{k} \sum_{\boldsymbol{k}'} \sum_{\boldsymbol{k}''} \; & c_{k-k_0} \; \frac{q_\alpha^2}{2m_\alpha} \; \sqrt{\frac{\hbar}{2\epsilon_0 V \omega_{\boldsymbol{k}'}}} \\ & \times \sqrt{\frac{\hbar}{2\epsilon_0 V \omega_{\boldsymbol{k}''}}} \; \boldsymbol{\epsilon}_{u'} \cdot \boldsymbol{\epsilon}_{u''}^* \; e^{\iota(\boldsymbol{k}' \cdot \boldsymbol{r}_\alpha - \omega_{\boldsymbol{k}'} t)} \; e^{-\iota(\boldsymbol{k}'' \cdot \boldsymbol{r}_\alpha - \omega_{\boldsymbol{k}''} t)} \\ & \times \left\langle \mathrm{vac} \middle| \; \hat{a}_{v\boldsymbol{k}_\mathrm{s}} \; \hat{a}_{u'\boldsymbol{k}'} \; \hat{a}^\dagger_{u''\boldsymbol{k}''} \; \hat{a}^\dagger_{u\boldsymbol{k}} \; \middle| \mathrm{vac} \right\rangle .\end{aligned} \tag{1.24}$$

Applying Wick's theorem and accordingly equation (1.10) again, the matrix element in the last line of equation (1.24) evaluates to:

$$\begin{aligned}\left\langle \mathrm{vac} \middle| \; \hat{a}_{v\boldsymbol{k}_\mathrm{s}} \; \hat{a}_{u'\boldsymbol{k}'} \; \hat{a}^\dagger_{u''\boldsymbol{k}''} \; \hat{a}^\dagger_{u\boldsymbol{k}} \; \middle| \mathrm{vac} \right\rangle = \; & \delta_{u'u''} \; \delta_{uv} \; \delta_{\boldsymbol{k}'\boldsymbol{k}''} \; \delta_{\boldsymbol{k}\boldsymbol{k}_\mathrm{s}} \\ & + \delta_{u'u} \; \delta_{u''v} \; \delta_{\boldsymbol{k}'\boldsymbol{k}} \; \delta_{\boldsymbol{k}''\boldsymbol{k}_\mathrm{s}} .\end{aligned} \tag{1.25}$$

The first term on the right-hand side of equation (1.25) implies that the photon remains in its initial state $\left|\psi_{u\boldsymbol{k}_0}\right\rangle$ and that it is therefore not scattered at all. Only the second term describes a scattering event and has to be considered. Hence, equation (1.24) simplifies to:

$$\begin{aligned}\hat{O}(t) = \sum_{\alpha} \sum_{k} \; & c_{k-k_0} \; \frac{q_\alpha^2}{2m_\alpha} \; \sqrt{\frac{\hbar}{\epsilon_0 V \omega_{\boldsymbol{k}}}} \; \sqrt{\frac{\hbar}{\epsilon_0 V \omega_{\boldsymbol{k}_\mathrm{s}}}} \; \boldsymbol{\epsilon}_u \cdot \boldsymbol{\epsilon}_v^* \\ & \times e^{\iota(\boldsymbol{k} \cdot \boldsymbol{r}_\alpha - \omega_{\boldsymbol{k}} t)} \; e^{-\iota(\boldsymbol{k}_\mathrm{s} \cdot \boldsymbol{r}_\alpha - \omega_{\boldsymbol{k}_\mathrm{s}} t)} .\end{aligned} \tag{1.26}$$

By abbreviation of the polarisation factor $P = \boldsymbol{\epsilon}_u \cdot \boldsymbol{\epsilon}_v^*$ and reordering of the terms, equation (1.26) becomes:

$$\begin{aligned}\hat{O}(t) = P \; & \sqrt{\frac{\hbar}{\epsilon_0 V}} \; \sqrt{\frac{\hbar}{\epsilon_0 V \omega_{\boldsymbol{k}_\mathrm{s}}}} \cdot \sum_{\alpha} \; \frac{q_\alpha^2}{2m_\alpha} \; e^{-\iota(\boldsymbol{k}_\mathrm{s} \cdot \boldsymbol{r}_\alpha - \omega_{\boldsymbol{k}_\mathrm{s}} t)} \\ & \times \sum_{k} \; \frac{1}{\sqrt{\omega_{\boldsymbol{k}}}} \; c_{k-k_0} \; e^{\iota(\boldsymbol{k} \cdot \boldsymbol{r}_\alpha - \omega_{\boldsymbol{k}} t)} .\end{aligned} \tag{1.27}$$

With the transformations in equation (1.16), equation (1.27) is modified to:

$$\begin{aligned}\hat{O}(t) = P \; & \sqrt{\frac{\hbar}{\epsilon_0 V}} \; \sqrt{\frac{\hbar}{\epsilon_0 V \omega_{\boldsymbol{k}_\mathrm{s}}}} \cdot \sum_{\alpha} \; \frac{q_\alpha^2}{2m_\alpha} \; e^{-\iota(\boldsymbol{k}_\mathrm{s} \cdot \boldsymbol{r}_\alpha - \omega_{\boldsymbol{k}_\mathrm{s}} t)} \\ & \times \sum_{k'} \; \frac{1}{\sqrt{\omega_{\boldsymbol{k}'} + \omega_{\boldsymbol{k}_0}}} \; c_{k'} \; e^{\iota\left((\boldsymbol{k}' + \boldsymbol{k}_0) \cdot \boldsymbol{r}_\alpha - (\omega_{\boldsymbol{k}'} + \omega_{\boldsymbol{k}_0}) t\right)} .\end{aligned} \tag{1.28}$$

Renaming of k' as k and reordering of terms lead to:

$$\begin{aligned}\hat{O}(t) = P \sqrt{\frac{\hbar\omega_{\boldsymbol{k}_0}}{\epsilon_0 V}} \frac{\sqrt{2}}{\omega_{\boldsymbol{k}_0}} \sqrt{\frac{\hbar}{\epsilon_0 V \omega_{\boldsymbol{k}_\mathrm{s}}}} \cdot \sum_\alpha \frac{q_\alpha^2}{2m_\alpha} \, e^{-\iota(\boldsymbol{k}_\mathrm{s}\cdot\boldsymbol{r}_\alpha - \omega_{\boldsymbol{k}_\mathrm{s}} t)} \\ \times e^{\iota(\boldsymbol{k}_0\cdot\boldsymbol{r}_\alpha - \omega_{\boldsymbol{k}_0} t)} \cdot \sum_k \sqrt{\frac{\omega_{\boldsymbol{k}_0}}{\omega_{\boldsymbol{k}} + \omega_{\boldsymbol{k}_0}}} \, c_k \, e^{\iota(\boldsymbol{k}\cdot\boldsymbol{r}_\alpha - \omega_{\boldsymbol{k}} t)}.\end{aligned} \tag{1.29}$$

As in case of the intensity in equation (1.17), the amplitude of the classical electric field $E_{\boldsymbol{k}_0} = \sqrt{\hbar\omega_{\boldsymbol{k}_0}/(2\epsilon_0 V)}$ can be identified in equation (1.29). On condition that the distribution of angular frequencies around $\omega_{\boldsymbol{k}_0}$ is narrow so that $\omega_{\boldsymbol{k}} \ll \omega_{\boldsymbol{k}_0}$, the fraction $\sqrt{\omega_{\boldsymbol{k}_0}/(\omega_{\boldsymbol{k}} + \omega_{\boldsymbol{k}_0})}$ can be approximated by unity as well. Hence, the perturbation $\hat{O}(t)$ is:

$$\begin{aligned}\hat{O}(t) = P \, E_{\boldsymbol{k}_0} \frac{\sqrt{2}}{\omega_{\boldsymbol{k}_0}} \sqrt{\frac{\hbar}{\epsilon_0 V \omega_{\boldsymbol{k}_\mathrm{s}}}} \cdot \sum_\alpha \frac{q_\alpha^2}{2m_\alpha} \, e^{-\iota(\boldsymbol{k}_\mathrm{s}\cdot\boldsymbol{r}_\alpha - \omega_{\boldsymbol{k}_\mathrm{s}} t)} \\ \times e^{\iota(\boldsymbol{k}_0\cdot\boldsymbol{r}_\alpha - \omega_{\boldsymbol{k}_0} t)} \cdot \sum_k c_k \, e^{\iota(\boldsymbol{k}\cdot\boldsymbol{r}_\alpha - \omega_{\boldsymbol{k}} t)}.\end{aligned} \tag{1.30}$$

Equation (1.30) contains the time-dependent classical electric field of the incident X-ray pulse that involves the envelope $h(\boldsymbol{r}, t)$ from equation (1.19) and the carrier frequency $\omega_{\boldsymbol{k}_0}$:

$$E_{\boldsymbol{k}_0}(\boldsymbol{r}, t) = E_{\boldsymbol{k}_0} \, h(\boldsymbol{r}, t) \, e^{-\iota\omega_{\boldsymbol{k}_0} t}. \tag{1.31}$$

With equation (1.31), equation (1.30) becomes:

$$\hat{O}(t) = P \, \frac{\sqrt{2}}{\omega_{\boldsymbol{k}_0}} \sqrt{\frac{\hbar}{\epsilon_0 V \omega_{\boldsymbol{k}_\mathrm{s}}}} \, e^{\iota\omega_{\boldsymbol{k}_\mathrm{s}} t} \cdot \sum_\alpha \frac{q_\alpha^2}{2m_\alpha} \, E_{\boldsymbol{k}_0}(\boldsymbol{r}_\alpha, t) \, e^{\iota(\boldsymbol{k}_0 - \boldsymbol{k}_\mathrm{s})\cdot\boldsymbol{r}_\alpha}. \tag{1.32}$$

Introducing the scattering or momentum transfer vector $\boldsymbol{q} = \boldsymbol{k}_0 - \boldsymbol{k}_\mathrm{s}$, the perturbation $\hat{O}(t)$ is finally:

$$\hat{O}(t) = P \, \frac{\sqrt{2}}{\omega_{\boldsymbol{k}_0}} \sqrt{\frac{\hbar}{\epsilon_0 V \omega_{\boldsymbol{k}_\mathrm{s}}}} \, e^{\iota\omega_{\boldsymbol{k}_\mathrm{s}} t} \cdot \sum_\alpha \frac{q_\alpha^2}{2m_\alpha} \, E_{\boldsymbol{k}_0}(\boldsymbol{r}_\alpha, t) \, e^{\iota\boldsymbol{q}\cdot\boldsymbol{r}_\alpha}. \tag{1.33}$$

1.4 Differential Scattering Signal

After derivation of equation (1.33) for the perturbation operator $\hat{O}(t)$, the time-dependent first-order wave function from equation (1.3) can be inserted into equation (1.1), so that the differential scattering signal becomes:

$$\begin{aligned}
\frac{dS}{d\Omega} &= \frac{1}{\hbar^2} \cdot \int_0^{+\infty} \int_{-\infty}^{+\infty} \int_{-\infty}^{+\infty} \rho(\omega_{\boldsymbol{k}_\mathrm{s}}) \left\langle \Psi(t'') \,\middle|\, \hat{O}^\dagger(t'') \right. \\
&\quad \left. \times \hat{U}^\dagger(t,t'')\, \hat{U}(t,t')\, \hat{O}(t') \,\middle|\, \Psi(t') \right\rangle dt'\, dt''\, d\omega_{\boldsymbol{k}_\mathrm{s}} \\
&= \int_0^{+\infty} \int_{-\infty}^{+\infty} \int_{-\infty}^{+\infty} \rho(\omega_{\boldsymbol{k}_\mathrm{s}})\, \frac{2P^2}{\epsilon_0 V \hbar \omega_{\boldsymbol{k}_0}^2 \omega_{\boldsymbol{k}_\mathrm{s}}} \\
&\quad \times \left\langle \Psi(t'') \,\middle|\, \sum_\alpha \frac{q_\alpha^2}{2m_\alpha}\, E^*_{\boldsymbol{k}_0}(\boldsymbol{r}_\alpha, t'')\, e^{-\iota \boldsymbol{q}\cdot\boldsymbol{r}_\alpha} \right. \\
&\qquad\qquad \times e^{\frac{\iota}{\hbar}\hat{H}_\mathrm{M}(t-t'')}\, e^{-\frac{\iota}{\hbar}\hat{H}_\mathrm{M}(t-t')} \\
&\qquad\qquad \left. \times \sum_\beta \frac{q_\beta^2}{2m_\beta}\, E_{\boldsymbol{k}_0}(\boldsymbol{r}_\beta, t')\, e^{\iota \boldsymbol{q}\cdot\boldsymbol{r}_\beta} \,\middle|\, \Psi(t') \right\rangle \\
&\quad \times e^{-\iota\omega_{\boldsymbol{k}_\mathrm{s}}(t''-t')}\, dt'\, dt''\, d\omega_{\boldsymbol{k}_\mathrm{s}}.
\end{aligned} \tag{1.34}$$

With the definition of the density of angular frequencies $\rho(\omega_{\boldsymbol{k}_\mathrm{s}})$ given in equation (1.2), equation (1.34) simplifies to:

$$\begin{aligned}
\frac{dS}{d\Omega} &= \int_0^{+\infty} \int_{-\infty}^{+\infty} \int_{-\infty}^{+\infty} \frac{\omega_{\boldsymbol{k}_\mathrm{s}} P^2}{4\pi^3 c^3 \epsilon_0 \hbar \omega_{\boldsymbol{k}_0}^2} \\
&\quad \times \left\langle \Psi(t'') \,\middle|\, \sum_\alpha \frac{q_\alpha^2}{2m_\alpha}\, E^*_{\boldsymbol{k}_0}(\boldsymbol{r}_\alpha, t'')\, e^{-\iota \boldsymbol{q}\cdot\boldsymbol{r}_\alpha}\, e^{-\frac{\iota}{\hbar}\hat{H}_\mathrm{M}(t''-t')} \right. \\
&\qquad\qquad \left. \times \sum_\beta \frac{q_\beta^2}{2m_\beta}\, E_{\boldsymbol{k}_0}(\boldsymbol{r}_\beta, t')\, e^{\iota \boldsymbol{q}\cdot\boldsymbol{r}_\beta} \,\middle|\, \Psi(t') \right\rangle \\
&\quad \times e^{-\iota\omega_{\boldsymbol{k}_\mathrm{s}}(t''-t')}\, dt'\, dt''\, d\omega_{\boldsymbol{k}_\mathrm{s}}.
\end{aligned} \tag{1.35}$$

X-ray pulses at modern Free-Electron Laser facilities are typically several femtoseconds long and therefore spread over a range of micrometers. Atoms and molecules, however, extend over just a few Ångströms or nanometers at most. It can thus be assumed that the field envelope $h(\boldsymbol{r}_\alpha, t)$ at a given time t has essentially the same value for all particles of the material system, meaning that the change of $h(\boldsymbol{r}_\alpha, t)$ with coordinates $\{\boldsymbol{r}_\alpha\}$ is negligible. The field envelope can be approximated by a function that depends only on the mean position of the material system $\overline{\boldsymbol{R}}$ and time t then:

$$h(\boldsymbol{r}_\alpha, t) \approx h(\overline{\boldsymbol{R}}, t) = \sum_k \; c_k \; e^{\iota(\boldsymbol{k}\cdot\overline{\boldsymbol{R}} - \omega_{\boldsymbol{k}} t)}. \tag{1.36}$$

The time-dependent classical electric field of the incident X-ray pulse in equation (1.31) changes accordingly:

$$E_{\boldsymbol{k}_0}(\boldsymbol{r}, t) \approx E_{\boldsymbol{k}_0}(\overline{\boldsymbol{R}}, t) = E_{\boldsymbol{k}_0} \; h(\overline{\boldsymbol{R}}, t) \; e^{-\iota\omega_{\boldsymbol{k}_0} t}, \tag{1.37}$$

and can thus be moved out of the matrix element in equation (1.35):

$$\begin{aligned} \frac{dS}{d\Omega} = \int_0^{+\infty} \int_{-\infty}^{+\infty} \int_{-\infty}^{+\infty} & \frac{\omega_{\boldsymbol{k}_\mathrm{s}} P^2}{4\pi^3 c^3 \epsilon_0 \hbar \omega_{\boldsymbol{k}_0}^2} \; e^{-\iota\omega_{\boldsymbol{k}_\mathrm{s}}(t''-t')} \\ & \times \left\langle \Psi(t'') \;\middle|\; \sum_\alpha \; \frac{q_\alpha^2}{2m_\alpha} \; e^{-\iota\boldsymbol{q}\cdot\boldsymbol{r}_\alpha} \; e^{-\frac{\iota}{\hbar}\hat{H}_\mathrm{M}(t''-t')} \right. \\ & \qquad \left. \times \sum_\beta \; \frac{q_\beta^2}{2m_\beta} \; e^{\iota\boldsymbol{q}\cdot\boldsymbol{r}_\beta} \;\middle|\; \Psi(t') \right\rangle \\ & \times E_{\boldsymbol{k}_0}(\overline{\boldsymbol{R}}, t') \; E_{\boldsymbol{k}_0}^*(\overline{\boldsymbol{R}}, t'') \; dt' \; dt'' \; d\omega_{\boldsymbol{k}_\mathrm{s}}. \end{aligned} \tag{1.38}$$

Equation (1.38) reveals that every charged particle of the material system contributes to the differential scattering signal with a term proportional to the ratio of its squared charge to its mass, $q_\alpha^2/(2m_\alpha)$ and $q_\beta^2/(2m_\beta)$. Since nuclei in atoms are at least three orders of magnitudes heavier than electrons, X-ray scattering by nuclei is negligible. This is illustrated as follows. The strength of the nuclear relative to the electronic contribution of atoms can be estimated as:

$$\mu_{eZ}(Z) = \frac{q_Z^2}{2m_Z} \;\Big/\; \frac{Ze^2}{2m_e} \cdot 1000‰. \tag{1.39}$$

q_Z and m_Z are the charge and the mass of a particular nucleus, respectively. $-e$ and m_e are the charge and the mass of an electron. Figure **1.1** shows $\mu_{eZ}(Z)$ for the most abundant isotopes from hydrogen to uranium. The relative strength of the nuclear contribution drops from roughly 0.54‰ for ${}_1^1\mathrm{H}$ to 0.27‰ for ${}_2^4\mathrm{He}$ and to 0.21‰ for ${}_{92}^{238}\mathrm{U}$. This decrease is a consequence of the increasing neutron-proton ratio of elements with growing Z.

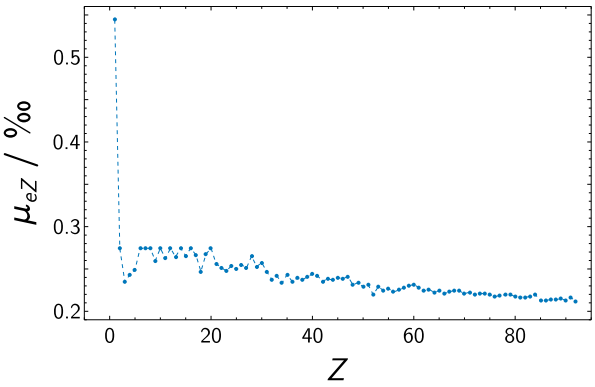

Fig. 1.1: Relative strength of X-ray scattering by nuclei with atomic number Z estimated according to equation (1.39).

The sums over the charged particles with indices α and β in equation (1.38) can therefore be restricted to electrons:

$$\begin{aligned}\frac{dS}{d\Omega} = &\int_0^{+\infty}\int_{-\infty}^{+\infty}\int_{-\infty}^{+\infty} \frac{e^4\omega_{\boldsymbol{k}_\mathrm{s}}P^2}{16\pi^3c^3\epsilon_0 m_e^2\hbar\omega_{\boldsymbol{k}_0}^2}\; e^{-\imath\omega_{\boldsymbol{k}_\mathrm{s}}(t''-t')} \\ &\times \left\langle \Psi(t'') \middle| \sum_m e^{-\imath\boldsymbol{q}\cdot\boldsymbol{r}_m}\; e^{-\frac{\imath}{\hbar}\hat{H}_\mathrm{M}(t''-t')} \sum_n e^{\imath\boldsymbol{q}\cdot\boldsymbol{r}_n} \middle| \Psi(t') \right\rangle \\ &\times E_{\boldsymbol{k}_0}(\overline{\boldsymbol{R}},t')\; E^*_{\boldsymbol{k}_0}(\overline{\boldsymbol{R}},t'')\; dt'\; dt''\; d\omega_{\boldsymbol{k}_\mathrm{s}}.\end{aligned} \tag{1.40}$$

The quantities $\{\boldsymbol{r}_m\}$ and $\{\boldsymbol{r}_n\}$ in equation (1.40) are electronic coordinates. Identifying the Thomson scattering cross-section of the free electron [41,44,45]:

$$\frac{d\sigma_\mathrm{T}}{d\Omega} = \frac{e^4P^2}{16\pi^2\epsilon_0^2m_e^2c^4}, \tag{1.41}$$

and defining the one-electron scattering operator:

$$\hat{L} = \sum_n e^{\imath\boldsymbol{q}\cdot\boldsymbol{r}_n}, \tag{1.42}$$

equation (1.40) can be written as:

$$\begin{aligned}\frac{dS}{d\Omega} = &\frac{1}{2\pi}\frac{d\sigma_\mathrm{T}}{d\Omega}\cdot\int_0^{+\infty}\int_{-\infty}^{+\infty}\int_{-\infty}^{+\infty} \frac{\omega_{\boldsymbol{k}_\mathrm{s}}}{\omega_{\boldsymbol{k}_0}}\; e^{-\imath\omega_{\boldsymbol{k}_\mathrm{s}}(t''-t')} \\ &\times \left\langle \Psi(t'') \middle| \hat{L}^\dagger\; e^{-\frac{\imath}{\hbar}\hat{H}_\mathrm{M}(t''-t')}\; \hat{L} \middle| \Psi(t') \right\rangle \\ &\times \frac{2\epsilon_0 c}{\hbar\omega_{\boldsymbol{k}_0}}\; E_{\boldsymbol{k}_0}(\overline{\boldsymbol{R}},t')\; E^*_{\boldsymbol{k}_0}(\overline{\boldsymbol{R}},t'')\; dt'\; dt''\; d\omega_{\boldsymbol{k}_\mathrm{s}}.\end{aligned} \tag{1.43}$$

Moreover, the product in the last line of equation (1.43) simplifies to:

$$\frac{2\epsilon_0 c}{\hbar\omega_{\boldsymbol{k}_0}}\; E_{\boldsymbol{k}_0}(\overline{\boldsymbol{R}},t')\; E^*_{\boldsymbol{k}_0}(\overline{\boldsymbol{R}},t'') = \frac{c}{V}\; h(\overline{\boldsymbol{R}},t')\; h^*(\overline{\boldsymbol{R}},t'')\; e^{\iota\omega_{\boldsymbol{k}_0}(t''-t')}, \tag{1.44}$$

and equation (1.43) becomes:

$$\begin{aligned}\frac{dS}{d\Omega} = \frac{1}{2\pi}\;\frac{d\sigma_{\mathrm{T}}}{d\Omega}\cdot\int_0^{+\infty}\int_{-\infty}^{+\infty}\int_{-\infty}^{+\infty}\;\frac{\omega_{\boldsymbol{k}_\mathrm{s}}}{\omega_{\boldsymbol{k}_0}}\;e^{\iota(\omega_{\boldsymbol{k}_0}-\omega_{\boldsymbol{k}_\mathrm{s}})(t''-t')}\\ \times\left\langle\Psi(t'')\;\middle|\;\hat{L}^\dagger\;e^{-\frac{\iota}{\hbar}\hat{H}_\mathrm{M}(t''-t')}\;\hat{L}\;\middle|\;\Psi(t')\right\rangle\\ \times\frac{c}{V}\;h(\overline{\boldsymbol{R}},t')\;h^*(\overline{\boldsymbol{R}},t'')\;dt'\;dt''\;d\omega_{\boldsymbol{k}_\mathrm{s}}.\end{aligned} \tag{1.45}$$

A substitution of $t-\delta/2$ and $t+\delta/2$ for the two time variables t' and t'', respectively, permits further simplifications in the following. With the substitution, equation (1.45) transforms into:

$$\begin{aligned}\frac{dS}{d\Omega} = \frac{1}{2\pi}\;\frac{d\sigma_{\mathrm{T}}}{d\Omega}\cdot\int_0^{+\infty}\int_{-\infty}^{+\infty}\int_{-\infty}^{+\infty}\;\frac{\omega_{\boldsymbol{k}_\mathrm{s}}}{\omega_{\boldsymbol{k}_0}}\;e^{\iota(\omega_{\boldsymbol{k}_0}-\omega_{\boldsymbol{k}_\mathrm{s}})\delta}\\ \times\left\langle\Psi\Big(t+\frac{\delta}{2}\Big)\;\middle|\;\hat{L}^\dagger\;e^{-\frac{\iota}{\hbar}\hat{H}_\mathrm{M}\delta}\;\hat{L}\;\middle|\;\Psi\Big(t-\frac{\delta}{2}\Big)\right\rangle\\ \times\frac{c}{V}\;h\Big(\overline{\boldsymbol{R}},t-\frac{\delta}{2}\Big)\;h^*\Big(\overline{\boldsymbol{R}},t+\frac{\delta}{2}\Big)\;dt\;d\delta\;d\omega_{\boldsymbol{k}_\mathrm{s}}.\end{aligned} \tag{1.46}$$

It is now assumed that the field modes $\left|u\boldsymbol{k}\right\rangle$ of the incident X-ray pulse are so close in energy that their discrete distribution c_k can be approximated by a continuous function. Given that the pulse is focussed on the material system at all times and assuming that the absolute square of the field envelope is well described by a Gaussian centred at time τ with standard deviation σ, the envelope can be further approximated to be:

$$h(\overline{\boldsymbol{R}},t)\approx h_\mathrm{p}(t-\tau) = N_h\;e^{-\frac{(t-\tau)^2}{4\sigma^2}}. \tag{1.47}$$

Here, N_h is a factor that scales the envelope. If the absolute square of the field envelope is assumed to be normalised, it will be $N_h = 1/\sqrt{\sqrt{2\pi}\sigma}$.

With equation (1.47), the product of the two envelope functions $h\big(\overline{\boldsymbol{R}},t-\delta/2\big)$ and $h^*\big(\overline{\boldsymbol{R}},t+\delta/2\big)$ in the last line of equation (1.46) separates into two functions that depend on only one of the two time variables t and δ each:

$$\begin{aligned} h\Big(\overline{\boldsymbol{R}}, t-\frac{\delta}{2}\Big)\; h^*\Big(\overline{\boldsymbol{R}}, t+\frac{\delta}{2}\Big) &\approx h_\mathrm{p}\Big(t-\frac{\delta}{2}-\tau\Big)\; h_\mathrm{p}\Big(t+\frac{\delta}{2}-\tau\Big) \\ &= \big|N_h\big|^2\; e^{-\frac{(t-\delta/2-\tau)^2}{4\sigma^2}}\; e^{-\frac{(t+\delta/2-\tau)^2}{4\sigma^2}} \\ &= \big|N_h\big|^2\; e^{-\frac{(t-\tau)^2}{2\sigma^2}}\; e^{-\frac{\delta^2}{8\sigma^2}} \\ &= \big|h_\mathrm{p}(t-\tau)\big|^2\; \sqrt{h_\mathrm{p}(\delta)}. \end{aligned} \tag{1.48}$$

Analogous to the light intensity in equation (1.18), the absolute square of the envelope function $h_\mathrm{p}(t-\tau)$ in equation (1.48) is equal to the photon number intensity[42,44–46] of the incident X-ray pulse:

$$I(t-\tau) = \frac{c}{V}\; \big|h_\mathrm{p}(t-\tau)\big|^2. \tag{1.49}$$

Similarly, the square root of the envelope function $h_\mathrm{p}(\delta)$ is equal to the time-correlation or coherence function[42,44,45] of the pulse:

$$C(\delta) = \sqrt{h_\mathrm{p}(\delta)}. \tag{1.50}$$

Considering equations (1.47) to (1.50), equation (1.46) can be written as:

$$\begin{aligned} \frac{dS}{d\Omega} = \frac{1}{2\pi}\; \frac{d\sigma_\mathrm{T}}{d\Omega} \cdot \int_0^{+\infty}\; \frac{\omega_{\boldsymbol{k}_\mathrm{s}}}{\omega_{\boldsymbol{k}_0}}\; \int_{-\infty}^{+\infty}\; I(t-\tau)\; \int_{-\infty}^{+\infty}\; C(\delta) \\ \times\, e^{\imath(\omega_{\boldsymbol{k}_0}-\omega_{\boldsymbol{k}_\mathrm{s}})\delta}\; \mathcal{L}(\boldsymbol{q}, t, \delta)\; d\delta\; dt\; d\omega_{\boldsymbol{k}_\mathrm{s}}, \end{aligned} \tag{1.51}$$

where $\mathcal{L}(\boldsymbol{q}, t, \delta)$ is the scattering amplitude:

$$\mathcal{L}(\boldsymbol{q}, t, \delta) = \Big\langle \Psi(t) \Big|\; e^{\frac{\imath}{2\hbar}\hat{H}_\mathrm{M}\delta}\; \hat{L}^\dagger\; e^{-\frac{\imath}{\hbar}\hat{H}_\mathrm{M}\delta}\; \hat{L}\; e^{\frac{\imath}{2\hbar}\hat{H}_\mathrm{M}\delta} \;\Big|\; \Psi(t) \Big\rangle. \tag{1.52}$$

The variable t in equations (1.49), (1.51), and (1.52) is the real time in which both the wave function $\big|\Psi(t)\big\rangle$ and the photon number intensity $I(t-\tau)$ evolve. The parameter τ denotes the time at which the X-ray pulse is centred and corresponds to the pump-probe delay in experiments. The integral over t convolutes the instantaneous scattering signal at time t with the photon number intensity $I(t-\tau)$, thereby accounting for the finite duration of the X-ray pulse. The variable δ in equations (1.50), (1.51), and (1.52) refers to the temporal coherence of the pulse. The integral over δ is a Fourier transform that converts the coherence function $C(\delta)$ into its corresponding spectral density[42,45] in the frequency domain. The three time-evolution operators in the matrix element in equation (1.52) yield information about

the energy that is transferred between the X-ray photon and the material system in the scattering process.

The approximations that have been applied above refer to the description of the incident X-ray pulse and its interaction with the material system only. The time-dependent electronic wave function $\big|\Psi(t)\big\rangle$ in equation (1.52) is hitherto completely general. In the following two sections, equation (1.51) is simplified and discussed for non-stationary electronic and nuclear wave packets in atoms and molecules.

2 Scattering by Atoms

If the material system probed by time-resolved X-ray scattering is an atom in a non-stationary state, the time-dependent wave function $\big|\Psi(t)\big\rangle$ can be expanded as an electronic wave packet:

$$\big|\Psi(t)\big\rangle = \sum_{i}^{N} \; c_i(t) \; e^{-\frac{\imath}{\hbar}E_i t} \; \big|\varphi_i\big\rangle. \tag{2.1}$$

The states $\big|\varphi_i\big\rangle$ in equation (2.1) are eigenstates of of the field-free atomic Hamiltonian $\hat{H}$. They obey the corresponding time-independent Schrödinger equation $\hat{H} \; \big|\varphi_i\big\rangle = E_i \; \big|\varphi_i\big\rangle$ with eigenvalues E_i. The multipliers $c_i(t)$ are time-dependent expansion coefficients. If the wave packet is prepared by laser excitation, the coefficients will change during the interaction with the laser pulse. Once the pulse is over and no other external field excites the system, the coefficients become independent of time. Since the wave packet is normalised, the absolute squares of the coefficients add up to unity.

A substitution of equation (2.1) for the states in equation (1.52) permits further simplifications and a more specific, more detailed discussion of time-resolved non-resonant X-ray scattering by atoms. If the expansion of $\big|\Psi(t)\big\rangle$ is applied to equation (1.52) and if the resolution of the identity in the basis of the eigenstates:

$$\boldsymbol{I} = \sum_{k}^{\infty} \; \big|\varphi_k\big\rangle \; \big\langle\varphi_k\big|, \tag{2.2}$$

is inserted behind each of the three time-evolution operators, the matrix element $\mathcal{L}(\boldsymbol{q}, t, \delta)$ becomes:

$$\mathcal{L}(\boldsymbol{q}, t, \delta) = \sum_{i,j}^{N} \sum_{f}^{\infty} \; c_i(t) \; c_j^*(t) \; e^{-\imath\omega_{ij}t} \; e^{-\imath\omega_{fij}\delta} \; L_{fi}(\boldsymbol{q}) \; L_{fj}^*(\boldsymbol{q}), \tag{2.3}$$

where the indices i and j refer to eigenstates occupied by the electronic wave packet in equation (2.1). The index f can denote any eigenstate of the atom. The two angular frequencies in the exponentials are $\omega_{ij} = \big(E_i - E_j\big)/\hbar$ and $\omega_{fij} = \big(E_f - [E_i + E_j]/2\big)/\hbar$. $L_{fi}(\boldsymbol{q})$ and $L^*_{fj}(\boldsymbol{q})$ are matrix elements of the one-electron scattering operator $\hat{L}$:

$$\begin{aligned} L_{fi}(\boldsymbol{q}) &= \Big\langle \varphi_f \,\Big|\, \hat{L} \,\Big|\, \varphi_i \Big\rangle = \sum_n^{N_e} \,\Big\langle \varphi_f \Big|\, e^{\iota \boldsymbol{q}\cdot\boldsymbol{r}_n} \,\Big|\varphi_i\Big\rangle, \\ L^*_{fj}(\boldsymbol{q}) &= \Big\langle \varphi_j \,\Big|\, \hat{L}^\dagger \,\Big|\, \varphi_f \Big\rangle = \sum_n^{N_e} \,\Big\langle \varphi_j \Big|\, e^{-\iota \boldsymbol{q}\cdot\boldsymbol{r}_n} \,\Big|\varphi_f\Big\rangle. \end{aligned} \tag{2.4}$$

The matrix elements in equation (2.4) imply integration over the set of electronic coordinates $\{\boldsymbol{r}_n\}$. N_e denotes the number of electrons of the atom. One-electron scattering matrix elements can be written as Fourier transformed expectation values of the one-electron density operator $\delta(\boldsymbol{r} - \boldsymbol{r}_n)$ [47]:

$$\begin{aligned} \rho_{fi}(\boldsymbol{r}) &= \sum_{n=1}^{N_e} \,\Big\langle \varphi_f \,\Big|\, \delta(\boldsymbol{r} - \boldsymbol{r}_n) \,\Big|\, \varphi_i \Big\rangle, \\ L_{fi}(\boldsymbol{q}) &= \int_{-\infty}^{+\infty} e^{\iota \boldsymbol{q}\cdot\boldsymbol{r}}\; \rho_{fi}(\boldsymbol{r})\; d\boldsymbol{r} = \mathcal{F}_{\boldsymbol{r}}\big[\rho_{fi}(\boldsymbol{r})\big](\boldsymbol{q}), \end{aligned} \tag{2.5}$$

where the sum over n refers to all N_e electrons of the atom. The Fourier transform $\mathcal{F}_{\boldsymbol{r}}\big[\rho_{fi}(\boldsymbol{r})\big](\boldsymbol{q})$ in equation (2.5) occurs from real into reciprocal space, from the domain of the electronic coordinates $\boldsymbol{r}$ into the domain of the scattering vector $\boldsymbol{q} = \boldsymbol{k}_0 - \boldsymbol{k}_\mathrm{s}$. Equations (2.5) can be derived as follows. First, the integrals of the scattering matrix element are written out explicitly:

$$\begin{aligned} L_{fi}(\boldsymbol{q}) = \sum_{n=1}^{N_e} \int_{-\infty}^{+\infty} & e^{\iota \boldsymbol{q}\cdot\boldsymbol{r}_n}\; \varphi_f^*(\boldsymbol{r}_1 \ldots \boldsymbol{r}_{N_e}) \\ & \times \varphi_i(\boldsymbol{r}_1 \ldots \boldsymbol{r}_{N_e})\; d\boldsymbol{r}_1 \ldots d\boldsymbol{r}_{N_e}. \end{aligned} \tag{2.6}$$

Second, the exponential $\exp\big[\iota \boldsymbol{q}\cdot\boldsymbol{r}_n\big]$ is expressed as an integral over a general electronic coordinate $\boldsymbol{r}$ by use of the sifting property of the Dirac delta function $\delta(\boldsymbol{r} - \boldsymbol{r}_n)$:

$$e^{\iota \boldsymbol{q}\cdot\boldsymbol{r}_n} = \int_{-\infty}^{+\infty} e^{\iota \boldsymbol{q}\cdot\boldsymbol{r}}\; \delta(\boldsymbol{r} - \boldsymbol{r}_n)\; d\boldsymbol{r}. \tag{2.7}$$

Insertion of equation (2.7) into equation (2.6) leads to equations (2.5) after interchange of the order of the integrals. It follows that the diagonal one-electron scattering matrix element $L_{ii}(\boldsymbol{q})$ corresponds to the form factor $f_i(\boldsymbol{q})$ of the atom in state i:

$$L_{ii}(\boldsymbol{q}) = \int_{-\infty}^{+\infty} e^{\imath \boldsymbol{q}\cdot\boldsymbol{r}}\ \rho_{ii}(\boldsymbol{r})\ d\boldsymbol{r} = f_i(\boldsymbol{q}). \tag{2.8}$$

The atomic form factor of the ground state $f_0(\boldsymbol{q})$ is used in crystallography and traditional X-ray diffraction [41,48] as well as in the independent atom model [21,27,29,41] that approximates the elastic scattering signal of molecules as a simple sum of atomic form factors.

With equation (2.3), the differential scattering signal in (1.51) becomes:

$$\begin{aligned}\frac{dS}{d\Omega} = \frac{1}{2\pi}\ \frac{d\sigma_{\mathrm{T}}}{d\Omega} \cdot \sum_{i,j}^{N}\sum_{f}^{\infty}\ \int_{-\infty}^{+\infty}\ I(t-\tau)\ c_i(t)\ c_j^*(t)\ e^{-\imath\omega_{ij}t}\ dt \\ \times \int_{0}^{+\infty}\ \frac{\omega_{\boldsymbol{k}_\mathrm{s}}}{\omega_{\boldsymbol{k}_0}} \cdot \int_{-\infty}^{+\infty}\ C(\delta)\ e^{\imath(\omega_{\boldsymbol{k}_0}-\omega_{\boldsymbol{k}_\mathrm{s}}-\omega_{fij})\delta}\ d\delta \\ \times L_{fi}(\boldsymbol{q})\ L_{fj}^*(\boldsymbol{q})\ d\omega_{\boldsymbol{k}_\mathrm{s}}.\end{aligned} \tag{2.9}$$

Identifying the integral over δ in equation (2.9) as a Fourier transform of the coherence function $C(\delta)$ equal to the spectral density [42,45] of the X-ray pulse at the angular frequency $\omega_{\boldsymbol{k}_\mathrm{s}} - \omega_{\boldsymbol{k}_0} + \omega_{fij}$:

$$F\big(\omega_{\boldsymbol{k}_\mathrm{s}} - \omega_{\boldsymbol{k}_0} + \omega_{fij}\big) = \frac{1}{2\pi} \cdot \int_{-\infty}^{+\infty}\ C(\delta)\ e^{\imath(\omega_{\boldsymbol{k}_0}-\omega_{\boldsymbol{k}_\mathrm{s}}-\omega_{fij})\delta}\ d\delta, \tag{2.10}$$

equation (2.9) simplifies to:

$$\begin{aligned}\frac{dS}{d\Omega} = \frac{d\sigma_{\mathrm{T}}}{d\Omega} \cdot \sum_{i,j}^{N}\sum_{f}^{\infty}\ \int_{-\infty}^{+\infty}\ I(t-\tau)\ c_i(t)\ c_j^*(t)\ e^{-\imath\omega_{ij}t}\ dt \\ \times \int_{0}^{+\infty}\ \frac{\omega_{\boldsymbol{k}_\mathrm{s}}}{\omega_{\boldsymbol{k}_0}}\ F\big(\omega_{\boldsymbol{k}_\mathrm{s}} - \omega_{\boldsymbol{k}_0} + \omega_{fij}\big)\ L_{fi}(\boldsymbol{q})\ L_{fj}^*(\boldsymbol{q})\ d\omega_{\boldsymbol{k}_\mathrm{s}}.\end{aligned} \tag{2.11}$$

Following the common Waller-Hartree approximation [49], it is furthermore assumed that the differences in energies of the incident and the scattered photons are small in comparison to the mean photon energy of the X-ray pulse, *i.e.* $\omega_{\boldsymbol{k}_\mathrm{s}} \approx \omega_{\boldsymbol{k}_0}$. The Waller-Hartree approximation does not imply that the differential scattering signal becomes purely elastic. It only means that the $\boldsymbol{q}$-space coordinates that are generally dependent on both $\omega_{\boldsymbol{k}_0}$ and $\omega_{\boldsymbol{k}_\mathrm{s}}$ become independent of the angular frequency of the scattered photons $\omega_{\boldsymbol{k}_\mathrm{s}}$. The scattering matrix elements $L_{fi}(\boldsymbol{q})$ and $L_{fj}^*(\boldsymbol{q})$ can therefore be moved out of the integral over $\omega_{\boldsymbol{k}_\mathrm{s}}$, yielding:

$$\frac{dS}{d\Omega} = \frac{d\sigma_{\mathrm{T}}}{d\Omega} \cdot \sum_{i,j}^{N} \sum_{f}^{\infty} W_{fij}(\Delta\omega)\ L_{fi}(\boldsymbol{q}_0)\ L_{fj}^{*}(\boldsymbol{q}_0) \times \int_{-\infty}^{+\infty} I(t-\tau)\ c_i(t)\ c_j^{*}(t)\ e^{-\imath\omega_{ij}t}\ dt. \tag{2.12}$$

where $\boldsymbol{q}_0$ denotes a scattering vector that does not depend on $\omega_{\boldsymbol{k}_\mathrm{s}}$ and the detection window $W_{fij}(\Delta\omega)$ refers to the remaining integral over $\omega_{\boldsymbol{k}_\mathrm{s}}$:

$$W_{fij}(\Delta\omega) = \int_{\omega_{\boldsymbol{k}_0}-\Delta\omega}^{\omega_{\boldsymbol{k}_0}+\Delta\omega} F\big(\omega_{\boldsymbol{k}_\mathrm{s}} - \omega_{\boldsymbol{k}_0} + \omega_{fij}\big)\ d\omega_{\boldsymbol{k}_\mathrm{s}}. \tag{2.13}$$

The variable $\Delta\omega$ in equation (2.13) defines the range of detected photons with angular frequencies around the mean $\omega_{\boldsymbol{k}_0}$. It has to be significantly smaller than $\omega_{\boldsymbol{k}_0}$ itself to ensure that the assumption $\omega_{\boldsymbol{k}_\mathrm{s}} \approx \omega_{\boldsymbol{k}_0}$ of the Waller-Hartree approximation is justified. The window $W_{fij}(\Delta\omega)$ accounts for the number of incident X-ray photons with angular frequencies that can be shifted by ω_{fij} to frequencies $\omega_{\boldsymbol{k}_\mathrm{s}}$ within the range of $\pm\Delta\omega$ around $\omega_{\boldsymbol{k}_0}$. The shift ω_{fij} corresponds to an inelastic energy transfer between the photon and the atom. Since the value of $W_{fij}(\Delta\omega)$ decreases with an increase in ω_{fij}, the function effectively introduces an upper limit into the sum over f.

Three different contributions to the time-resolved differential X-ray scattering signal can be identified in equation (2.12). First, the scattering is purely elastic if $i = j = f$:

$$\frac{dS_\mathrm{e}}{d\Omega} = \frac{d\sigma_{\mathrm{T}}}{d\Omega}\ W(\Delta\omega) \cdot \sum_{i}^{N} \big|L_{ii}(\boldsymbol{q}_0)\big|^2 \times \int_{-\infty}^{+\infty} I(t-\tau)\ \big|c_i(t)\big|^2\ dt. \tag{2.14}$$

The angular frequency $\omega_{fij} = \big(E_f - [E_i + E_j]/2\big)/\hbar$ that refers to an electronic transition vanishes if the scattering is elastic. The weights $W_{fij}(\Delta\omega)$ are therefore independent of their indices in equation (2.14).

Second, the scattering is purely inelastic if $i = j \neq f$:

$$\frac{dS_\mathrm{i}}{d\Omega} = \frac{d\sigma_{\mathrm{T}}}{d\Omega} \cdot \sum_{i}^{N} \sum_{f\neq i}^{\infty} W_{fi}(\Delta\omega)\ \big|L_{fi}(\boldsymbol{q}_0)\big|^2 \times \int_{-\infty}^{+\infty} I(t-\tau)\ \big|c_i(t)\big|^2\ dt. \tag{2.15}$$

The angular frequency ω_{fij} simplifies to $\omega_{fi} = \big(E_f - E_i\big)/\hbar$ if the scattering is inelastic. The redundant index j of the weights $W_{fij}(\Delta\omega)$ is dropped in equation (2.15). The quantity $\hbar\omega_{fi}$ is the energy that the atom gains from or loses to the X-ray photon.

Third, the scattering refers to electronic coherences if $i \neq j$ for all f:

$$\begin{aligned}\frac{dS_\mathrm{c}}{d\Omega} = \frac{d\sigma_\mathrm{T}}{d\Omega} \cdot \sum_i^N \sum_{j\neq i}^N \sum_f^\infty W_{fij}(\Delta\omega)\; L_{fi}(\boldsymbol{q}_0)\; L^*_{fj}(\boldsymbol{q}_0) \\ \times \int_{-\infty}^{+\infty} I(t-\tau)\; c_i(t)\; c^*_j(t)\; e^{-\iota\omega_{ij}t}\; dt.\end{aligned} \tag{2.16}$$

Since an interchange of two values of i and j in equation (2.16) yields the complex conjugate of the term:

$$L_{fi}(\boldsymbol{q}_0)\; L^*_{fj}(\boldsymbol{q}_0)\; c_i(t)\; c^*_j(t)\; e^{-\iota\omega_{ij}t}, \tag{2.17}$$

the sums in equation (2.16) can be restricted:

$$\begin{aligned}\frac{dS_\mathrm{c}}{d\Omega} = 2\;\frac{d\sigma_\mathrm{T}}{d\Omega} \cdot \sum_i^{N-1} \sum_{j>i}^N \sum_f^\infty W_{fij}(\Delta\omega) \cdot \int_{-\infty}^{+\infty} I(t-\tau) \\ \times \mathrm{Re}\Big[L_{fi}(\boldsymbol{q}_0)\; L^*_{fj}(\boldsymbol{q}_0)\; c_i(t)\; c^*_j(t)\; e^{-\iota\omega_{ij}t}\Big]\; dt.\end{aligned} \tag{2.18}$$

The detection window $W_{fij}(\Delta\omega)$ is not included in the real part in equation (2.18), because the angular frequency $\omega_{fij} = \big(E_f - [E_i + E_j]/2\big)/\hbar$ is invariant under interchange of i and j.

It follows from equations (2.14) and (2.15) that both the purely elastic and the purely inelastic contribution are independent of the pump-probe delay τ when the coefficients $c_i(t)$ become time-independent constants:

$$\frac{dS_\mathrm{e}}{d\Omega} = \frac{d\sigma_\mathrm{T}}{d\Omega}\; N_\mathrm{p}\; W(\Delta\omega) \cdot \sum_i^N \big|c_i\big|^2\; \big|L_{ii}(\boldsymbol{q}_0)\big|^2, \tag{2.19}$$

$$\frac{dS_\mathrm{i}}{d\Omega} = \frac{d\sigma_\mathrm{T}}{d\Omega}\; N_\mathrm{p} \cdot \sum_i^N \sum_{f\neq i}^\infty W_{fi}(\Delta\omega)\; \big|c_i\big|^2\; \big|L_{fi}(\boldsymbol{q}_0)\big|^2. \tag{2.20}$$

The quantity N_p in equations (2.19) and (2.20) is the integrated photon number intensity $N_\mathrm{p} = \int_{-\infty}^{+\infty} I(t-\tau)\; dt$, *i.e.* the number of photons in the

incident pulse. It is assumed to be the same at all pump-probe delays τ. The situation of constant coefficients c_i occurs when the interaction with the pump pulse that prepares the wave packet is over and the populations in the individual eigenstates are no longer altered. Then, the sum of the elastic and inelastic contributions defines the static average of the differential scattering signal, whereas the coherence contribution in equation (2.18) describes its time-dependent modulation at a particular pump-probe delay τ. Without the coherence terms, the scattering signal of atoms would remain stationary under such conditions.

2.1 Large Detection Range

In most experiments the detection range $\hbar\Delta\omega$ is much larger than the transition energies $\hbar\omega_{fij}$ of the atom. Under such conditions the weights $W_{fij}(\Delta\omega)$ become independent of their indices and equation (2.12) can be simplified further:

$$\begin{aligned}\frac{dS}{d\Omega} = \frac{d\sigma_{\mathrm{T}}}{d\Omega}\, W(\Delta\omega) \cdot \sum_{i,j}^{N} \int_{-\infty}^{+\infty} I(t-\tau)\; c_i(t)\; c_j^*(t)\; e^{-\iota\omega_{ij}t}\; dt \\ \times \sum_{f}^{\infty} L_{fi}(\boldsymbol{q}_0)\; L_{fj}^*(\boldsymbol{q}_0).\end{aligned} \tag{2.21}$$

Each term of the sum over f is weighted equally by $W(\Delta\omega)$ now. Thus, the resolution of the identity $\boldsymbol{I} = \sum_f^\infty \left|\varphi_f\right\rangle\!\left\langle\varphi_f\right|$ can be applied to the sum of the scattering matrix elements in the last line of equation (2.21):

$$\begin{aligned}\sum_{f}^{\infty} L_{fi}(\boldsymbol{q}_0)\; L_{fj}^*(\boldsymbol{q}_0) &= \sum_{f}^{\infty} \left\langle\varphi_j\right|\, \hat{L}_0^\dagger \,\left|\varphi_f\right\rangle \left\langle\varphi_f\right|\, \hat{L}_0 \,\left|\varphi_i\right\rangle \\ &= \left\langle\varphi_j\right|\, \hat{L}_0^\dagger\; \hat{L}_0 \,\left|\varphi_i\right\rangle,\end{aligned} \tag{2.22}$$

where $\hat{L}_0$ denotes the scattering operator with the scattering vector $\boldsymbol{q} \approx \boldsymbol{q}_0$ in the Waller-Hartree approximation. The matrix element in the last line of equation (2.22) is a two-electron scattering matrix element:

$$\Lambda_{ji}(\boldsymbol{q}_0) = \left\langle\varphi_j\right|\, \hat{L}_0^\dagger\; \hat{L}_0 \,\left|\varphi_i\right\rangle = \sum_{m,n}^{N_e} \left\langle\varphi_j\right|\, e^{\iota\boldsymbol{q}_0\cdot(\boldsymbol{r}_n - \boldsymbol{r}_m)} \,\left|\varphi_i\right\rangle. \tag{2.23}$$

Due to the orthonormality of the eigenstates $\left\{\left|\varphi_i\right\rangle\right\}$, elements with indices $m = n$ in equation (2.23) reduce to the Kronecker delta δ_{ij}. The matrix element can therefore be written as:

$$\Lambda_{ji}(\boldsymbol{q}_0) = N_e\ \delta_{ij} + \tilde{\Lambda}_{ji}(\boldsymbol{q}_0), \tag{2.24}$$

where $\tilde{\Lambda}_{ji}(\boldsymbol{q}_0)$ is the pure two-electron part with $m \neq n$:

$$\tilde{\Lambda}_{ji}(\boldsymbol{q}_0) = \sum_{m}^{N_e} \sum_{n \neq m}^{N_e} \left\langle \varphi_j \,\middle|\, e^{\iota \boldsymbol{q}_0 \cdot (\boldsymbol{r}_n - \boldsymbol{r}_m)} \,\middle|\, \varphi_i \right\rangle. \tag{2.25}$$

Analogous to equation (2.5), the scattering matrix element in equation (2.25) can be expressed as a doubly Fourier transformed expectation value of the two-electron density operator $\delta(\boldsymbol{r}_1 - \boldsymbol{r}_m)\ \delta(\boldsymbol{r}_2 - \boldsymbol{r}_n)$ [47]:

$$\begin{aligned} \rho_{ji}(\boldsymbol{r}_1, \boldsymbol{r}_2) &= \frac{1}{2} \cdot \sum_{m}^{N_e} \sum_{n \neq m}^{N_e} \left\langle \varphi_j \,\middle|\, \delta(\boldsymbol{r}_1 - \boldsymbol{r}_m)\ \delta(\boldsymbol{r}_2 - \boldsymbol{r}_n) \,\middle|\, \varphi_i \right\rangle, \\ \tilde{\Lambda}_{ji}(\boldsymbol{q}_0) &= 2 \cdot \int_{-\infty}^{+\infty} \int_{-\infty}^{+\infty} e^{\iota \boldsymbol{q}_0 \cdot (\boldsymbol{r}_2 - \boldsymbol{r}_1)}\ \rho_{ji}(\boldsymbol{r}_1, \boldsymbol{r}_2)\ d\boldsymbol{r}_1\ d\boldsymbol{r}_2 \\ &= 2 \cdot \mathcal{F}_{\boldsymbol{r}_2 - \boldsymbol{r}_1}\big[\rho_{ji}(\boldsymbol{r}_1, \boldsymbol{r}_2)\big](\boldsymbol{q}_0). \end{aligned} \tag{2.26}$$

The two electron density operator probes the correlated presence of two different electrons at their respective coordinates $\boldsymbol{r}_1$ and $\boldsymbol{r}_2$. The double Fourier transform $\mathcal{F}_{\boldsymbol{r}_2 - \boldsymbol{r}_1}\big[\rho_{ji}(\boldsymbol{r}_1, \boldsymbol{r}_2)\big](\boldsymbol{q}_0)$ in equation (2.26) occurs from real into reciprocal space twice. Equations (2.26) can be derived as follows. Again, the integrals of the scattering matrix element are written out explicitly first:

$$\begin{aligned} \tilde{\Lambda}_{ji}(\boldsymbol{q}_0) = \sum_{m}^{N_e} \sum_{n \neq m}^{N_e} \int_{-\infty}^{+\infty} & e^{\iota \boldsymbol{q}_0 \cdot (\boldsymbol{r}_n - \boldsymbol{r}_m)}\ \varphi_f^*(\boldsymbol{r}_1 \ldots \boldsymbol{r}_{N_e}) \\ & \times \varphi_i(\boldsymbol{r}_1 \ldots \boldsymbol{r}_{N_e})\ d\boldsymbol{r}_1 \ldots d\boldsymbol{r}_{N_e}. \end{aligned} \tag{2.27}$$

Second, the exponential $\exp\big[\iota \boldsymbol{q}(\boldsymbol{r}_n - \boldsymbol{r}_m)\big]$ is expressed as a product of two integrals over two different electronic coordinates $\boldsymbol{r}_1$ and $\boldsymbol{r}_2$ by use of the sifting property of the Dirac delta function $\delta(\boldsymbol{r} - \boldsymbol{r}_n)$:

$$\begin{aligned} e^{\iota \boldsymbol{q}_0 \cdot (\boldsymbol{r}_n - \boldsymbol{r}_m)} = \int_{-\infty}^{+\infty} \int_{-\infty}^{+\infty} & e^{\iota \boldsymbol{q}_0 \cdot (\boldsymbol{r}_2 - \boldsymbol{r}_1)}\ \delta(\boldsymbol{r}_1 - \boldsymbol{r}_m) \\ & \times \delta(\boldsymbol{r}_2 - \boldsymbol{r}_n)\ d\boldsymbol{r}_1\ d\boldsymbol{r}_2. \end{aligned} \tag{2.28}$$

Insertion of equation (2.28) into equation (2.27) leads to equations (2.26) after interchange of the order of the integrals.

With equations (2.22) and (2.23), equation (2.21) becomes:

$$\frac{dS}{d\Omega} = \frac{d\sigma_{\mathrm{T}}}{d\Omega}\, W(\Delta\omega) \cdot \sum_{i,j}^{N} \Lambda_{ji}(\boldsymbol{q}_0) \cdot \int_{-\infty}^{+\infty} I(t-\tau)\; c_i(t) \times c_j^*(t)\; e^{-\iota\omega_{ij}t}\; dt. \tag{2.29}$$

Similar to equation (2.12), three contributions to the time-resolved differential X-ray scattering signal can be identified in equation (2.29). The first term of the two-electron scattering matrix element $N_{\mathrm{e}}\,\delta_{ij}$ in equation (2.24) leads to the scattering signal of N_{e} free electrons:

$$\frac{dS_1}{d\Omega} = \frac{d\sigma_{\mathrm{T}}}{d\Omega}\, N_{\mathrm{e}}\, N_{\mathrm{p}}\, W(\Delta\omega). \tag{2.30}$$

The one-electron contribution described by equation (2.30) reflects that, from the perspective of the X-ray photons, an electron can move freely within the bound system if all transitions are equally allowed. $dS_1/d\Omega$ is a global, time-independent quantity that can be subtracted from the total signal without loss of $\boldsymbol{q}_0$-dependent information.

The second term $\tilde{\Lambda}_{ji}(\boldsymbol{q}_0)$ in equation (2.24) yields for $i = j$:

$$\frac{dS_2}{d\Omega} = \frac{d\sigma_{\mathrm{T}}}{d\Omega}\, W(\Delta\omega) \cdot \sum_{i}^{N} \tilde{\Lambda}_{ii}(\boldsymbol{q}_0) \cdot \int_{-\infty}^{+\infty} I(t-\tau)\; \left|c_i(t)\right|^2\, dt. \tag{2.31}$$

Equation (2.31) is the two-electron part of the elastic and inelastic scattering of equations (2.14) and (2.15) in the limit of a large detection range $\Delta\omega$. Consequently, $\boldsymbol{q}_0$-dependent information in the scattering signal stems solely from the two-electron contributions when all transitions are detected equally.

Finally, the term $\tilde{\Lambda}_{ji}(\boldsymbol{q}_0)$ in equation (2.24) yields for $i \neq j$:

$$\frac{dS_{\mathrm{c}}}{d\Omega} = \frac{d\sigma_{\mathrm{T}}}{d\Omega}\, W(\Delta\omega) \cdot \sum_{i}^{N}\sum_{j\neq i}^{N} \tilde{\Lambda}_{ji}(\boldsymbol{q}_0) \cdot \int_{-\infty}^{+\infty} I(t-\tau)\; c_i(t) \times c_j^*(t)\; e^{-\iota\omega_{ij}t}\; dt. \tag{2.32}$$

Since the two-electron scattering matrix elements form a Hermitian matrix:

$$\begin{aligned}\tilde{\Lambda}_{ij}(\boldsymbol{q}_0) &= \sum_{m}^{N_e}\sum_{n\neq m}^{N_e} \left\langle \varphi_i \right|\, e^{\iota\boldsymbol{q}_0\cdot(\boldsymbol{r}_n - \boldsymbol{r}_m)}\, \left|\, \varphi_j \right\rangle \\ &= \sum_{m}^{N_e}\sum_{n\neq m}^{N_e} \left\langle \varphi_j \right|\, e^{\iota\boldsymbol{q}_0\cdot(\boldsymbol{r}_n - \boldsymbol{r}_m)}\, \left|\, \varphi_i \right\rangle^* = \tilde{\Lambda}_{ji}^*(\boldsymbol{q}_0),\end{aligned} \tag{2.33}$$

an interchange of two values of i and j in equation (2.32) yields the complex conjugate of the term:

$$\tilde{\Lambda}_{ji}(\boldsymbol{q}_0)\ c_i(t)\ c_j^*(t)\ e^{-\imath\omega_{ij}t}. \tag{2.34}$$

Hence, the sums in equation (2.32) can be restricted:

$$\begin{aligned}\frac{dS_\mathrm{c}}{d\Omega} = 2\ \frac{d\sigma_\mathrm{T}}{d\Omega}\ W(\Delta\omega) \cdot \sum_{i}^{N-1} \sum_{j>i}^{N} \int_{-\infty}^{+\infty} I(t-\tau) \\ \times \mathrm{Re}\Big[\tilde{\Lambda}_{ji}(\boldsymbol{q}_0)\ c_i(t)\ c_j^*(t)\ e^{-\imath\omega_{ij}t}\Big]\ dt.\end{aligned} \tag{2.35}$$

Equation (2.35) is the two-electron part of the coherence contribution from equation (2.18) in the limit of a large $\Delta\omega$.

As the elastic and inelastic scattering in equations (2.14) and (2.15), the single-state contribution in equation (2.31) becomes independent of the pump-probe delay τ in the situation of time-independent coefficients:

$$\frac{dS_2}{d\Omega} = \frac{d\sigma_\mathrm{T}}{d\Omega}\ N_\mathrm{p}\ W(\Delta\omega) \cdot \sum_{i}^{N} \big|c_i\big|^2\ \tilde{\Lambda}_{ii}(\boldsymbol{q}_0). \tag{2.36}$$

Again, solely the coherence terms in equation (2.35) change with pump-probe delay τ under such conditions.

Moreover, the scattering signal of single-electron systems like the hydrogen atom is entirely described by the time-independent one-electron contribution in equation (2.30). The one-electron part of the coherence contribution from equation (2.18) vanishes in the limit of a large detection range $\Delta\omega$. Single-electron systems thus require a sufficiently sharp range of photon energies that are accepted by the detector if X-ray scattering is supposed to yield structural and time-dependent information.

3 Scattering by Molecules

If the material system probed by time-resolved X-ray scattering is a molecule in a non-stationary state, the time-dependent wave function $\big|\Psi(t)\big\rangle$ can be expanded in a direct product basis:

$$\Big|\Psi(t)\Big\rangle = \sum_{k}^{N} \Big|\chi_k(t)\Big\rangle\ \Big|\varphi_k\big(\{\boldsymbol{R}_\alpha\}\big)\Big\rangle. \tag{3.1}$$

The states $\big|\varphi_k\big(\{\boldsymbol{R}_\alpha\}\big)\big\rangle$ in equation (3.1) are eigenstates of of the field-free electronic Hamiltonian $\hat{H}_e$ and depend parametrically on the set of nuclear coordinates $\{\boldsymbol{R}_\alpha\}$. They obey the time-independent Schrödinger equation:

$$\hat{H}_e \ \Big|\varphi_k\big(\{\boldsymbol{R}_\alpha\}\big)\Big\rangle = V_k\big(\{\boldsymbol{R}_\alpha\}\big) \ \Big|\varphi_k\big(\{\boldsymbol{R}_\alpha\}\big)\Big\rangle, \tag{3.2}$$

with eigenvalues $V_k\big(\{\boldsymbol{R}_\alpha\}\big)$. Moreover, the vectors $\big|\chi_k(t)\big\rangle$ in equation (3.1) are nuclear wave packets associated with their respective electronic states with index k. They can be understood as time-dependent superpositions of rovibrational eigenstates of the time-independent nuclear Schrödinger equation in the Born-Oppenheimer approximation:

$$\Big[\hat{T}_\mathrm{N} + V_k\big(\{\boldsymbol{R}_\alpha\}\big)\Big] \ \Big|\chi_{k,\nu_k,J_k}\Big\rangle = E_{k,\nu_k,J_k} \ \Big|\chi_{k,\nu_k,J_k}\Big\rangle, \tag{3.3}$$

where ν_k and J_k are vibrational and rotational quantum numbers, $\hat{T}_\mathrm{N}$ is the kinetic energy operator of the nuclei, E_{k,ν_k,J_k} denotes the total energy of the molecule, and $V_k\big(\{\boldsymbol{R}_\alpha\}\big)$ acts as the potential. With time-dependent coefficients $a_{\nu_k,J_k}(t)$, the nuclear wave packet expands to:

$$\Big|\chi_k(t)\Big\rangle = \sum_{\nu_k,J_k}^{N_{\nu_k},N_{J_k}} a_{\nu_k,J_k}(t) \ \Big|\chi_{k,\nu_k,J_k}\Big\rangle. \tag{3.4}$$

The expansion of the molecular wave function in equation (3.1) is, at least in principle, exact. Non-adiabatic couplings of the electronic states that may invalidate the adiabatic or Born-Oppenheimer approximation can be taken into account in the propagation of the nuclear wave packets $\big|\chi_k(t)\big\rangle$.

A substitution of equation (3.1) for the states in equation (1.52) permits further simplifications and a more specific, more detailed discussion of time-resolved non-resonant X-ray scattering by molecules. If the expansion of $\big|\Psi(t)\big\rangle$ is applied to equation (1.52) and if the resolution of the identity in the direct product basis:

$$\boldsymbol{I} = \sum_{\{k\}}^{\infty} \ \Big|\varphi_k\big(\{\boldsymbol{R}_\alpha\}\big)\Big\rangle \ \Big|\chi_{\{k\}}\Big\rangle \ \Big\langle\chi_{\{k\}}\Big| \ \Big\langle\varphi_k\big(\{\boldsymbol{R}_\alpha\}\big)\Big|, \tag{3.5}$$

where the set of quantum numbers $\{k,\ \nu_k,\ J_k\}$ is abbreviated as $\{k\}$, is inserted behind each of the three time-evolution operators in equation (1.52), the matrix element $\mathcal{L}(\boldsymbol{q},t,\delta)$ becomes:

$$\begin{aligned}\mathcal{L}(\boldsymbol{q},t,\delta) = &\sum_{i,j}^{N}\sum_{\nu_i,J_i}^{\infty}\sum_{\nu_j,J_j}^{\infty}\sum_{\{f\}}^{\infty} e^{-\iota\omega_{\{fij\}}\delta}\; a_{\nu_i,J_i}(t)\; a^{*}_{\nu_j,J_j}(t) \\ &\times \Big\langle \chi_{\{f\}}\Big|\; L_{fi}\big(\boldsymbol{q},\{\boldsymbol{R}_\alpha\}\big)\;\Big|\chi_{\{i\}}\Big\rangle\;\Big\langle \chi_{\{j\}}\Big|\; L^{*}_{fj}\big(\boldsymbol{q},\{\boldsymbol{R}_\alpha\}\big)\;\Big|\chi_{\{f\}}\Big\rangle,\end{aligned} \tag{3.6}$$

where it has been assumed that the action of the time-evolution operators that involve the molecular Hamiltonian $\hat{H}_{\mathrm{M}} = \hat{H}_e + \hat{T}_{\mathrm{N}}$ is adiabatic:

$$e^{-\frac{\iota}{\hbar}\hat{H}_{\mathrm{M}}\delta}\;\Big|\varphi_k\big(\{\boldsymbol{R}_\alpha\}\big)\Big\rangle\;\Big|\chi_{\{k\}}\Big\rangle \approx e^{-\frac{\iota}{\hbar}E_{\{k\}}\delta}\;\Big|\varphi_k\big(\{\boldsymbol{R}_\alpha\}\big)\Big\rangle\;\Big|\chi_{\{k\}}\Big\rangle. \tag{3.7}$$

This approximation only affects the propagation in the δ-domain in which the temporal coherence of the pulse is defined. It refers exclusively to the energy that is exchanged between the molecule and the X-ray photon and does not imply that the molecular wave function $\big|\Psi(t)\big\rangle$ itself evolves non-adiabatically in t.

The angular frequency in the exponential in the first line of equation (3.6) is $\omega_{\{fij\}} = \big(E_{\{f\}} - [E_{\{i\}} + E_{\{j\}}]/2\big)/\hbar$. The two matrix elements in the second line imply integration over the set of nuclear coordinates $\{\boldsymbol{R}_\alpha\}$. $L_{fi}\big(\boldsymbol{q},\{\boldsymbol{R}_\alpha\}\big)$ and $L^{*}_{fj}\big(\boldsymbol{q},\{\boldsymbol{R}_\alpha\}\big)$ are matrix elements of the scattering operator:

$$\begin{aligned} L_{fi}\big(\boldsymbol{q},\{\boldsymbol{R}_\alpha\}\big) &= \Big\langle \varphi_f\big(\{\boldsymbol{R}_\alpha\}\big)\Big|\;\hat{L}\;\Big|\varphi_i\big(\{\boldsymbol{R}_\alpha\}\big)\Big\rangle, \\ L^{*}_{fj}\big(\boldsymbol{q},\{\boldsymbol{R}_\alpha\}\big) &= \Big\langle \varphi_j\big(\{\boldsymbol{R}_\alpha\}\big)\Big|\;\hat{L}^{\dagger}\;\Big|\varphi_f\big(\{\boldsymbol{R}_\alpha\}\big)\Big\rangle. \end{aligned} \tag{3.8}$$

Analogous to the atomic case in equations (2.4), the scattering matrix elements in equations (3.8) imply integration over the set of electronic coordinates $\{\boldsymbol{r}_n\}$. The only difference is the parametric dependence of the elements on $\{\boldsymbol{R}_\alpha\}$. Hence, the discussion around equations (2.5) to (2.7) holds here as well. The scattering matrix elements can be written as Fourier transformed expectation values of the one-electron density operator.

The diagonal one-electron scattering matrix element of the molecule in its electronic ground state $L_{\mathrm{GS}}\big(\boldsymbol{q},\{\boldsymbol{R}_\alpha\}\big)$ is often approximated in the framework of the independent atom model (IAM) [21,27,29,41] as a sum of the atomic form factors from equation (2.8). With the form factor $f_{\alpha,0}(\boldsymbol{q})$ that refers to an atom with index α in its ground state, $L_{\mathrm{GS}}\big(\boldsymbol{q},\{\boldsymbol{R}_\alpha\}\big)$ is approximated as:

$$L_{\mathrm{GS}}\big(\boldsymbol{q},\{\boldsymbol{R}_\alpha\}\big) \approx \sum_{\alpha}\; f_{\alpha,0}(\boldsymbol{q})\; e^{\iota\boldsymbol{q}\cdot\boldsymbol{R}_\alpha} = F\big(\boldsymbol{q},\{\boldsymbol{R}_\alpha\}\big). \tag{3.9}$$

Each atomic form factor $f_{\alpha,0}(\boldsymbol{q})$ in equation (3.9) is multiplied with a factor $\exp\big[\iota\boldsymbol{q}\cdot\boldsymbol{R}_\alpha\big]$ that accounts for the position $\boldsymbol{R}_\alpha$ of the corresponding atom in the molecule. The IAM is a fair approximation for systems that include heavier elements with many core electrons that remain largely unaffected by neighbouring atoms. Considering lighter systems with a smaller ratio of core to valence electrons, however, it can deviate significantly from the correct scattering matrix elements $L_{\mathrm{GS}}\big(\boldsymbol{q},\{\boldsymbol{R}_\alpha\}\big)$, since it is neglecting any reorganisation of the one-electron density due to covalent bonding. Furthermore, the IAM cannot describe the effect of electronic excitation and is thus questionable, if not useless in situations where more than just the elastic scattering signal of heavy systems in their electronic ground state is investigated. If a molecular wave packet evolves in more than just one electronic state, an accurate evaluation of the one-electron scattering matrix elements, particularly of the off-diagonal ones, will most likely be inevitable.

Turning back to equation (3.6), an insertion of the matrix element $\mathcal{L}(\boldsymbol{q},t,\delta)$ into equation (1.51) yields for the differential scattering signal:

$$\begin{aligned}\frac{dS}{d\Omega} = \frac{1}{2\pi}\,\frac{d\sigma_{\mathrm{T}}}{d\Omega}\cdot\sum_{i,j}^{N}\sum_{\nu_i,J_i}^{\infty}\sum_{\nu_j,J_j}^{\infty}\sum_{\{f\}}^{\infty}\int_0^{+\infty}\frac{\omega_{\boldsymbol{k}_\mathrm{s}}}{\omega_{\boldsymbol{k}_0}}\cdot\int_{-\infty}^{+\infty}C(\delta)\\ \times\, e^{\iota(\omega_{\boldsymbol{k}_0}-\omega_{\boldsymbol{k}_\mathrm{s}}-\omega_{\{fij\}})\delta}\,d\delta\,\Big\langle\chi_{\{f\}}\Big|\,L_{fi}\big(\boldsymbol{q},\{\boldsymbol{R}_\alpha\}\big)\,\Big|\chi_{\{i\}}\Big\rangle\\ \times\,\Big\langle\chi_{\{j\}}\Big|\,L^*_{fj}\big(\boldsymbol{q},\{\boldsymbol{R}_\alpha\}\big)\,\Big|\chi_{\{f\}}\Big\rangle\,d\omega_{\boldsymbol{k}_\mathrm{s}}\\ \times\int_{-\infty}^{+\infty}I(t-\tau)\;a_{\nu_i,J_i}(t)\;a^*_{\nu_j,J_j}(t)\;dt.\end{aligned}\tag{3.10}$$

Identifying the integral over δ in equation (3.10) as a Fourier transform of the coherence function $C(\delta)$ equal to the spectral density[42,45] of the X-ray pulse at the angular frequency $\omega_{\boldsymbol{k}_\mathrm{s}}-\omega_{\boldsymbol{k}_0}+\omega_{\{fij\}}$:

$$F\big(\omega_{\boldsymbol{k}_\mathrm{s}}-\omega_{\boldsymbol{k}_0}+\omega_{\{fij\}}\big)=\frac{1}{2\pi}\cdot\int_{-\infty}^{+\infty}C(\delta)\;e^{\iota(\omega_{\boldsymbol{k}_0}-\omega_{\boldsymbol{k}_\mathrm{s}}-\omega_{\{fij\}})\delta}\;d\delta,\tag{3.11}$$

equation (3.10) simplifies to:

$$\begin{aligned}\frac{dS}{d\Omega} = \frac{d\sigma_{\mathrm{T}}}{d\Omega}\cdot\sum_{i,j}^{N}\sum_{\nu_i,J_i}^{\infty}\sum_{\nu_j,J_j}^{\infty}\sum_{\{f\}}^{\infty}\int_0^{+\infty}\frac{\omega_{\boldsymbol{k}_\mathrm{s}}}{\omega_{\boldsymbol{k}_0}}\;F\big(\omega_{\boldsymbol{k}_\mathrm{s}}-\omega_{\boldsymbol{k}_0}+\omega_{\{fij\}}\big)\\ \times\,\Big\langle\chi_{\{f\}}\Big|\,L_{fi}\big(\boldsymbol{q},\{\boldsymbol{R}_\alpha\}\big)\,\Big|\chi_{\{i\}}\Big\rangle\,\Big\langle\chi_{\{j\}}\Big|\,L^*_{fj}\big(\boldsymbol{q},\{\boldsymbol{R}_\alpha\}\big)\,\Big|\chi_{\{f\}}\Big\rangle\,d\omega_{\boldsymbol{k}_\mathrm{s}}\\ \times\int_{-\infty}^{+\infty}I(t-\tau)\;a_{\nu_i,J_i}(t)\;a^*_{\nu_j,J_j}(t)\;dt.\end{aligned}\tag{3.12}$$

Following the common Waller-Hartree approximation[49], it is furthermore assumed that the differences in energies of the incident and the scattered photons are small in comparison to the mean photon energy of the X-ray pulse, *i.e.* $\omega_{\boldsymbol{k}_\mathrm{s}} \approx \omega_{\boldsymbol{k}_0}$. The Waller-Hartree approximation does not imply that the differential scattering signal becomes purely elastic. It only means that the $\boldsymbol{q}$-space coordinates that are generally dependent on both $\omega_{\boldsymbol{k}_0}$ and $\omega_{\boldsymbol{k}_\mathrm{s}}$ become independent of the angular frequency of the scattered photons $\omega_{\boldsymbol{k}_\mathrm{s}}$. The scattering matrix elements $L_{fi}\big(\boldsymbol{q},\{\boldsymbol{R}_\alpha\}\big)$ and $L^*_{fj}\big(\boldsymbol{q},\{\boldsymbol{R}_\alpha\}\big)$ can therefore be moved out of the integral over $\omega_{\boldsymbol{k}_\mathrm{s}}$, yielding:

$$\begin{aligned}\frac{dS}{d\Omega} &= \frac{d\sigma_\mathrm{T}}{d\Omega}\cdot\sum_{i,j}^{N}\sum_{\nu_i,J_i}^{\infty}\sum_{\nu_j,J_j}^{\infty}\sum_{\{f\}}^{\infty} W_{\{fij\}}(\Delta\omega)\\ &\times\Big\langle\chi_{\{f\}}\Big|\, L_{fi}(\boldsymbol{q}_0,\{\boldsymbol{R}_\alpha\})\,\Big|\chi_{\{i\}}\Big\rangle\Big\langle\chi_{\{j\}}\Big|\, L^*_{fj}(\boldsymbol{q}_0,\{\boldsymbol{R}_\alpha\})\,\Big|\chi_{\{f\}}\Big\rangle\\ &\times\int_{-\infty}^{+\infty} I(t-\tau)\; a_{\nu_i,J_i}(t)\; a^*_{\nu_j,J_j}(t)\; dt.\end{aligned} \tag{3.13}$$

where $\boldsymbol{q}_0$ denotes a $\boldsymbol{q}$-vector that does not depend on $\omega_{\boldsymbol{k}_\mathrm{s}}$ and the detection window $W_{\{fij\}}(\Delta\omega)$ refers to the remaining integral over $\omega_{\boldsymbol{k}_\mathrm{s}}$:

$$W_{\{fij\}}(\Delta\omega) = \int_{\omega_{\boldsymbol{k}_0}-\Delta\omega}^{\omega_{\boldsymbol{k}_0}+\Delta\omega} F\big(\omega_{\boldsymbol{k}_\mathrm{s}} - \omega_{\boldsymbol{k}_0} + \omega_{\{fij\}}\big)\; d\omega_{\boldsymbol{k}_\mathrm{s}}. \tag{3.14}$$

As in equation (2.13), the variable $\Delta\omega$ in equation (3.14) defines the range of detected photons with angular frequencies around the mean $\omega_{\boldsymbol{k}_0}$. It has to be significantly smaller than $\omega_{\boldsymbol{k}_0}$ itself to ensure that the assumption $\omega_{\boldsymbol{k}_\mathrm{s}} \approx \omega_{\boldsymbol{k}_0}$ of the Waller-Hartree approximation is justified. The window $W_{\{fij\}}(\Delta\omega)$ accounts for the number of incident X-ray photons with angular frequencies that can be shifted by $\omega_{\{fij\}}$ to frequencies $\omega_{\boldsymbol{k}_\mathrm{s}}$ within the range of $\pm\Delta\omega$ around $\omega_{\boldsymbol{k}_0}$. The shift $\omega_{\{fij\}}$ corresponds to an inelastic energy transfer between the photon and the molecule. Since the value of $W_{\{fij\}}(\Delta\omega)$ decreases with an increase in $\omega_{\{fij\}}$, the function effectively introduces an upper limit into the sum over $\{f\}$.

3.1 Intermediate Detection Range

If $\hbar\Delta\omega$ is larger than the rovibrational transition energies, *i.e.* the differences in $E_{\{k\}}$ for a given electronic potential $V_k\big(\{\boldsymbol{R}_\alpha\}\big)$, transitions to all nuclear eigenstates are detected and the change of $W_{\{fij\}}(\Delta\omega)$ with rovibrational quantum numbers is negligible. The detection window can therefore be written with reference to the electronic energies only:

$$W_{\{fij\}}(\Delta\omega) \approx W_{fij}(\Delta\omega). \tag{3.15}$$

Equation (3.15) implies that the angular frequency $\omega_{\{fij\}}$ in equation (3.14) can be approximated by a frequency ω_{fij} that depends solely on the electronic energies. A reasonable choice is $\omega_{fij} = \big(V_{f,0} - [V_{i,0} + V_{j,0}]/2\big)/\hbar$ where the zero-point vibrational energy corrected electronic eigenvalues have been used. The precise definition of ω_{fij} is somewhat arbitrary, as equation (3.15) requires that differences in the order of the rovibrational energies do not alter $W_{\{fij\}}$ anyway. This also justifies the adiabatic approximation made in equation (3.7): non-adiabatic couplings between the electronic and nuclear motion can be neglected when the propagation in δ is considered, because the effect of the couplings on the transition energies $\hbar\omega_{fij}$ is not resolved.

With equation (3.15), equation (3.13) becomes:

$$\begin{aligned}\frac{dS}{d\Omega} = \frac{d\sigma_\mathrm{T}}{d\Omega} \cdot \sum_{i,j}^{N} \sum_{f}^{\infty} W_{fij}(\Delta\omega) \cdot \sum_{\nu_i,J_i}^{\infty} \sum_{\nu_j,J_j}^{\infty} \sum_{\nu_f,J_f}^{\infty} \int_{-\infty}^{+\infty} I(t-\tau) \\ \times \Big\langle \chi_j(t) \Big| \chi_{\{j\}} \Big\rangle \Big\langle \chi_{\{j\}} \Big| L^*_{fj}\big(\boldsymbol{q}_0, \{\boldsymbol{R}_\alpha\}\big) \Big| \chi_{\{f\}} \Big\rangle \\ \times \Big\langle \chi_{\{f\}} \Big| L_{fi}\big(\boldsymbol{q}_0, \{\boldsymbol{R}_\alpha\}\big) \Big| \chi_{\{i\}} \Big\rangle \Big\langle \chi_{\{i\}} \Big| \chi_i(t) \Big\rangle \, dt.\end{aligned} \tag{3.16}$$

Each term of the sums over the quantum numbers $\{\nu_i,\, J_i,\, \nu_j,\, J_j,\, \nu_f,\, J_f\}$ is weighted equally by $W_{fij}(\Delta\omega)$ now. Thus, the resolution of the identity in the nuclear subspace $\boldsymbol{I}_{\boldsymbol{R}} = \sum_{\nu_k,J_k}^{\infty} |\chi_{\{k\}}\rangle\langle\chi_{\{k\}}|$ can be applied to the matrix elements in equation (3.16), yielding:

$$\begin{aligned}\frac{dS}{d\Omega} = \frac{d\sigma_\mathrm{T}}{d\Omega} \cdot \sum_{i,j}^{N} \sum_{f}^{\infty} W_{fij}(\Delta\omega) \cdot \int_{-\infty}^{+\infty} I(t-\tau) \\ \times \Big\langle \chi_j(t) \Big| L_{fi}\big(\boldsymbol{q}_0, \{\boldsymbol{R}_\alpha\}\big) \, L^*_{fj}\big(\boldsymbol{q}_0, \{\boldsymbol{R}_\alpha\}\big) \Big| \chi_i(t) \Big\rangle \, dt.\end{aligned} \tag{3.17}$$

Again, three different contributions to the time-resolved differential X-ray scattering signal can be identified in equation (3.17). First, the scattering is electronically elastic if $i = j = f$:

$$\begin{aligned}\frac{dS_\mathrm{e}}{d\Omega} = \frac{d\sigma_\mathrm{T}}{d\Omega} \, W(\Delta\omega) \cdot \sum_{i}^{N} \int_{-\infty}^{+\infty} I(t-\tau) \\ \times \Big\langle \chi_i(t) \Big| \, \big|L_{ii}\big(\boldsymbol{q}_0, \{\boldsymbol{R}_\alpha\}\big)\big|^2 \, \Big| \chi_i(t) \Big\rangle \, dt.\end{aligned} \tag{3.18}$$

The angular frequency $\omega_{fij} = \big(V_{f,0} - [V_{i,0} + V_{j,0}]/2\big)/\hbar$ that refers to an electronic transition vanishes if the scattering is elastic. The weights $W_{fij}(\Delta\omega)$ are therefore independent of their indices in equation (3.18).

Second, the scattering is electronically inelastic if $i = j \neq f$:

$$\begin{aligned}\frac{dS_{\mathrm{i}}}{d\Omega} = \frac{d\sigma_{\mathrm{T}}}{d\Omega}\, W_{fi}(\Delta\omega) \cdot \sum_{i}^{N} \sum_{f}^{\infty} \int_{-\infty}^{+\infty} I(t-\tau) \\ \times \left\langle \chi_i(t) \right| \left| L_{fi}\big(\boldsymbol{q}_0, \{\boldsymbol{R}_\alpha\}\big) \right|^2 \left| \chi_i(t) \right\rangle \, dt.\end{aligned} \tag{3.19}$$

The angular frequency ω_{fij} simplifies to $\omega_{fi} = \big(E_f - E_i\big)/\hbar$ if the scattering is inelastic. $\hbar\omega_{fi}$ is approximately the energy that the molecule gains from or loses to the X-ray photon. The redundant index j of the weights $W_{fij}(\Delta\omega)$ is dropped.

Third, the scattering refers to coherent nuclear motion on two different electronic surfaces $V_i\big(\{\boldsymbol{R}_\alpha\}\big)$ and $V_j\big(\{\boldsymbol{R}_\alpha\}\big)$ if $i \neq j$ for all f:

$$\begin{aligned}\frac{dS_{\mathrm{c}}}{d\Omega} = \frac{d\sigma_{\mathrm{T}}}{d\Omega} \cdot \sum_{i}^{N} \sum_{j\neq i}^{N} \sum_{f}^{\infty} W_{fij}(\Delta\omega) \cdot \int_{-\infty}^{+\infty} I(t-\tau) \\ \times \left\langle \chi_j(t) \right| L_{fi}\big(\boldsymbol{q}_0, \{\boldsymbol{R}_\alpha\}\big)\; L^*_{fj}\big(\boldsymbol{q}_0, \{\boldsymbol{R}_\alpha\}\big) \left| \chi_i(t) \right\rangle \, dt.\end{aligned} \tag{3.20}$$

Since an interchange of two values of i and j in equation (3.20) yields the complex conjugate of the term:

$$\left\langle \chi_j(t) \right| L_{fi}\big(\boldsymbol{q}_0, \{\boldsymbol{R}_\alpha\}\big)\; L^*_{fj}\big(\boldsymbol{q}_0, \{\boldsymbol{R}_\alpha\}\big) \left| \chi_i(t) \right\rangle, \tag{3.21}$$

the sums in equation (3.20) can be restricted:

$$\begin{aligned}\frac{dS_{\mathrm{c}}}{d\Omega} = 2\, \frac{d\sigma_{\mathrm{T}}}{d\Omega} \cdot \sum_{i}^{N-1} \sum_{j>i}^{N} \sum_{f}^{\infty} W_{fij}(\Delta\omega) \cdot \int_{-\infty}^{+\infty} I(t-\tau) \\ \times \mathrm{Re}\left[\left\langle \chi_j(t) \right| L_{fi}\big(\boldsymbol{q}_0, \{\boldsymbol{R}_\alpha\}\big)\; L^*_{fj}\big(\boldsymbol{q}_0, \{\boldsymbol{R}_\alpha\}\big) \left| \chi_i(t) \right\rangle \right] dt.\end{aligned} \tag{3.22}$$

The detection window $W_{fij}(\Delta\omega)$ is not included in the real part in equation (3.22), because the angular frequency $\omega_{fij} = \big(V_{f,0} - [V_{i,0} + V_{j,0}]/2\big)/\hbar$ is invariant under interchange of i and j.

In contrast to the atomic case, the elastic and inelastic contributions to the scattering signal in equations (3.18) and (3.19) can be time-dependent even in the situation of unaltered populations in the individual electronic states. The elastic and the inelastic signals change according to the absolute square of the nuclear wave packet $\int_{-\infty}^{+\infty} I(t-\tau) \left| \chi_i\big(\{\boldsymbol{R}_\alpha\}, t\big) \right|^2 dt$ that has

been convoluted with the photon number intensity $I(t-\tau)$. They are thus related to the nuclear motion of the molecule.

The coherence terms in equation (3.22) can contain additional information about processes related to electronic motion that is induced by, for example, laser excitation or non-adiabatic coupling. Unlike the elastic and inelastic contributions, the coherence signal is sensitive to the complex phase of the nuclear wave packets.

3.2 Large Detection Range

In equation (3.15) a detection range $\hbar\Delta\omega$ has been assumed that still permits a discrimination between different electronic states. In most experiments, however, $\hbar\Delta\omega$ is much larger even than the electronic transition energies of the molecule $\hbar\omega_{fij}$. Under such conditions the weights $W_{fij}(\Delta\omega)$ become independent of their remaining electronic indices and equation (2.12) can be simplified further:

$$\begin{aligned}\frac{dS}{d\Omega} = \frac{d\sigma_{\mathrm{T}}}{d\Omega}\, W(\Delta\omega) \cdot \sum_{i,j}^{N} \int_{-\infty}^{+\infty} I(t-\tau) \\ \times \left\langle \chi_j(t) \right| \sum_{f}^{\infty} L_{fi}\big(\boldsymbol{q}_0, \{\boldsymbol{R}_\alpha\}\big)\; L^*_{fj}\big(\boldsymbol{q}_0, \{\boldsymbol{R}_\alpha\}\big) \left| \chi_i(t) \right\rangle dt.\end{aligned} \tag{3.23}$$

Each term of the sum over f is weighted equally by $W(\Delta\omega)$ now. As in equation (2.22), the resolution of the identity in the electronic subspace:

$$\boldsymbol{I_r} = \sum_{f}^{\infty} \left| \varphi_f\big(\{\boldsymbol{R}_\alpha\}\big) \right\rangle \left\langle \varphi_f\big(\{\boldsymbol{R}_\alpha\}\big) \right|, \tag{3.24}$$

can thus be applied to the sum of the scattering matrix elements in the last line of equation (3.23), yielding:

$$\begin{aligned}\frac{dS}{d\Omega} = \frac{d\sigma_{\mathrm{T}}}{d\Omega}\, W(\Delta\omega) \cdot \sum_{i,j}^{N} \int_{-\infty}^{+\infty} I(t-\tau) \\ \times \left\langle \chi_j(t) \right| \Lambda_{ji}\big(\boldsymbol{q}_0, \{\boldsymbol{R}_\alpha\}\big) \left| \chi_i(t) \right\rangle dt.\end{aligned} \tag{3.25}$$

The quantity $\Lambda_{ji}\big(\boldsymbol{q}_0, \{\boldsymbol{R}_\alpha\}\big)$ in equation (3.25) is the two-electron scattering matrix element defined in equation (2.23), even though parametrically dependent on the set of nuclear coordinates $\{\boldsymbol{R}_\alpha\}$:

$$\Lambda_{ji}\big(\boldsymbol{q}_0, \{\boldsymbol{R}_\alpha\}\big) = \sum_{m,n}^{N_e} \Big\langle \varphi_j\big(\{\boldsymbol{R}_\alpha\}\big) \Big| \; e^{\imath \boldsymbol{q}_0 \cdot (\boldsymbol{r}_n - \boldsymbol{r}_m)} \; \Big| \varphi_i\big(\{\boldsymbol{R}_\alpha\}\big) \Big\rangle . \tag{3.26}$$

Due to the orthonormality of the eigenstates $\big\{\big|\varphi_i\big(\{\boldsymbol{R}_\alpha\}\big)\big\rangle\big\}$, elements with indices $m = n$ in equation (3.26) reduce to the Kronecker delta δ_{ij} again. The matrix element can therefore be written as:

$$\Lambda_{ji}\big(\boldsymbol{q}_0, \{\boldsymbol{R}_\alpha\}\big) = N_e \; \delta_{ij} + \tilde{\Lambda}_{ji}\big(\boldsymbol{q}_0, \{\boldsymbol{R}_\alpha\}\big), \tag{3.27}$$

where $\tilde{\Lambda}_{ji}\big(\boldsymbol{q}_0, \{\boldsymbol{R}_\alpha\}\big)$ is the pure two-electron part with $m \neq n$:

$$\tilde{\Lambda}_{ji}\big(\boldsymbol{q}_0, \{\boldsymbol{R}_\alpha\}\big) = \sum_{m}^{N_e} \sum_{n \neq m}^{N_e} \Big\langle \varphi_j\big(\{\boldsymbol{R}_\alpha\}\big) \Big| \; e^{\imath \boldsymbol{q}_0 \cdot (\boldsymbol{r}_n - \boldsymbol{r}_m)} \; \Big| \varphi_i\big(\{\boldsymbol{R}_\alpha\}\big) \Big\rangle . \tag{3.28}$$

The scattering matrix element in equation (3.28) can be expressed as a doubly Fourier transformed expectation value of the two-electron density operator $\delta(\boldsymbol{r}_1 - \boldsymbol{r}_m)\; \delta(\boldsymbol{r}_2 - \boldsymbol{r}_n)$ as discussed in equations (2.26) to (2.28).

Similar to equation (3.17), three contributions to the time-resolved differential X-ray scattering signal can be identified in equation (3.25). The first term of the two-electron scattering matrix element $N_\mathrm{e}\; \delta_{ij}$ in equation (3.27) leads to the scattering signal of N_e free electrons:

$$\frac{dS_1}{d\Omega} = \frac{d\sigma_\mathrm{T}}{d\Omega} \; N_\mathrm{e} \; N_\mathrm{p} \; W(\Delta\omega). \tag{3.29}$$

The one-electron contribution described by equation (3.29) reflects that, from the perspective of the X-ray photons, a single electron can move freely within the bound system if all transitions are equally allowed. $dS_1/d\Omega$ is a global, time-independent quantity that can be subtracted from the total signal without loss of structural information.

The second term $\tilde{\Lambda}_{ji}\big(\boldsymbol{q}_0, \{\boldsymbol{R}_\alpha\}\big)$ in equation (3.27) yields for $i = j$:

$$\begin{aligned} \frac{dS_2}{d\Omega} = \frac{d\sigma_\mathrm{T}}{d\Omega} \; W(\Delta\omega) \cdot \sum_{i}^{N} \; & \int_{-\infty}^{+\infty} I(t-\tau) \\ & \times \Big\langle \chi_i(t) \Big| \; \tilde{\Lambda}_{ii}\big(\boldsymbol{q}_0, \{\boldsymbol{R}_\alpha\}\big) \; \Big| \chi_i(t) \Big\rangle \; dt. \end{aligned} \tag{3.30}$$

Equation (3.30) is the two-electron part of the elastic and inelastic scattering of equations (3.18) and (3.19) in the limit of a large detection range $\Delta\omega$.

Consequently, the structural information in the scattering signal stems from the two-electron contribution when all transitions are detected equally.

Finally, the second term $\tilde{\Lambda}_{ji}\big(\boldsymbol{q}_0, \{\boldsymbol{R}_\alpha\}\big)$ in equation (3.27) yields for $i \neq j$:

$$\begin{aligned}\frac{dS_\mathrm{c}}{d\Omega} = \frac{d\sigma_\mathrm{T}}{d\Omega}\, W(\Delta\omega) \cdot \sum_i^N \sum_{j\neq i}^N \int_{-\infty}^{+\infty} I(t-\tau) \\ \times \Big\langle \chi_j(t) \Big| \, \tilde{\Lambda}_{ji}\big(\boldsymbol{q}_0, \{\boldsymbol{R}_\alpha\}\big) \, \Big| \chi_i(t) \Big\rangle \, dt.\end{aligned} \tag{3.31}$$

Since an interchange of two values of i and j in equation (3.31) yields the complex conjugate of the term:

$$\Big\langle \chi_j(t) \Big| \, \tilde{\Lambda}_{ji}\big(\boldsymbol{q}_0, \{\boldsymbol{R}_\alpha\}\big) \, \Big| \chi_i(t) \Big\rangle, \tag{3.32}$$

with the property $\tilde{\Lambda}_{ij}\big(\boldsymbol{q}_0, \{\boldsymbol{R}_\alpha\}\big) = \tilde{\Lambda}^*_{ji}\big(\boldsymbol{q}_0, \{\boldsymbol{R}_\alpha\}\big)$ from equation (2.33), the sums in equation (3.31) can be restricted:

$$\begin{aligned}\frac{dS_\mathrm{c}}{d\Omega} = 2\, \frac{d\sigma_\mathrm{T}}{d\Omega}\, W(\Delta\omega) \cdot \sum_i^{N-1} \sum_{j>i}^N \int_{-\infty}^{+\infty} I(t-\tau) \\ \times \mathrm{Re}\Big[\Big\langle \chi_j(t) \Big| \, \tilde{\Lambda}_{ji}\big(\boldsymbol{q}_0, \{\boldsymbol{R}_\alpha\}\big) \, \Big| \chi_i(t) \Big\rangle \Big] \, dt.\end{aligned} \tag{3.33}$$

Equation (3.33) is the two-electron part of the coherence contribution from equation (3.22) in the limit of a large detection range $\hbar\Delta\omega$.

Like the elastic and inelastic scattering signals in equations (3.18) and (3.19), the single-state contributions in equations (3.29) and (3.30) change according to $\int_{-\infty}^{+\infty} I(t-\tau) \, \big|\chi_i\big(\{\boldsymbol{R}_\alpha\}, t\big)\big|^2 \, dt$ and reveal information about the nuclear motion of the molecule. The two-electron part of the coherence signal in equation (3.33) may add information about electronic motion. Unlike the single-state contributions in equations (3.29) and (3.30), the coherence signal is sensitive to the complex phase of the nuclear wave packets.

Part II

Evaluation of Scattering Matrix Elements

4 Geometry of X-ray Scattering

The differential scattering signal $dS/d\Omega$ is a function of the three-dimensional scattering or momentum transfer vector $\boldsymbol{q}$ in reciprocal space. The scattering vector is defined as the vector difference $\boldsymbol{q} = \boldsymbol{k}_0 - \boldsymbol{k}_\mathrm{s}$ where $\boldsymbol{k}_0$ and $\boldsymbol{k}_\mathrm{s}$ are the wave vectors of the incident and scattered X-ray radiation, respectively. In order to calculate $dS/d\Omega$ it is advantageous to express the components of $\boldsymbol{q}$ in terms of the components of $\boldsymbol{k}_0$ and $\boldsymbol{k}_\mathrm{s}$. The latter are usually known from the experimental conditions and the detection of a scattered photon. The required relations are derived in the following.

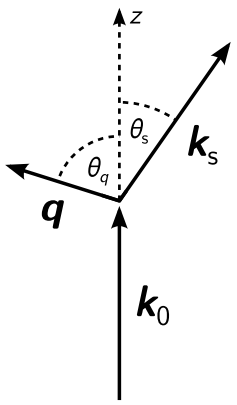

Fig. 4.1: Geometric relation of three vectors $\boldsymbol{k}_0$, $\boldsymbol{k}_\mathrm{s}$, and $\boldsymbol{q}$. $\boldsymbol{k}_0$ and $\boldsymbol{k}_\mathrm{s}$ are the wave vectors of the incident and scattered radiation, respectively. $\boldsymbol{q}$ is the scattering or momentum transfer vector $\boldsymbol{q} = \boldsymbol{k}_0 - \boldsymbol{k}_\mathrm{s}$. The scattering angle θ_s and the polar angle of the scattering vector θ_q are shown as well.

If the coordinate system is defined as in Figure **4.1** such that $\boldsymbol{k}_0$ is aligned with the z-axis in reciprocal space, $\boldsymbol{k}_0$ and $\boldsymbol{k}_\mathrm{s}$ are given as:

$$\boldsymbol{k}_0 = \begin{bmatrix} 0 \\ 0 \\ k_0 \end{bmatrix}, \qquad \boldsymbol{k}_\mathrm{s} = \boldsymbol{k}_0 - \boldsymbol{q} = \begin{bmatrix} -q_x \\ -q_y \\ k_0 - q_z \end{bmatrix} = \begin{bmatrix} -q\sin\theta_q\cos\phi_q \\ -q\sin\theta_q\sin\phi_q \\ k_0 - q\cos\theta_q \end{bmatrix}, \quad (4.1)$$

where k_0 is the norm of $\boldsymbol{k}_0$. Moreover, $\{q_x,\ q_y,\ q_z\}$ and $\{q,\ \theta_q,\ \phi_q\}$ are the Cartesian and spherical components of $\boldsymbol{q}$, respectively. q is the radial distance, θ_q the polar, and ϕ_q the azimuthal angle. The norm of $\boldsymbol{k}_\mathrm{s}$ is thus:

$$\begin{aligned} k_\mathrm{s} &= \sqrt{\left(q\sin\theta_q\cos\phi_q\right)^2 + \left(q\sin\theta_q\sin\phi_q\right)^2 + \left(k_0 - q\cos\theta_q\right)^2} \\ &= \sqrt{k_0^2 - 2\ k_0\ q\cos\theta_q + q^2}. \end{aligned} \quad (4.2)$$

Solving equation (4.2) for the polar angle θ_q yields:

$$\theta_q = \arccos\frac{k_0^2 - k_\mathrm{s}^2 + q^2}{2\ k_0\ q}. \quad (4.3)$$

With $k_\mathrm{s} \approx k_0$ from the Waller-Hartree approximation[49], θ_q simplifies to:

$$\theta_q \approx \arccos\frac{q}{2\ k_0}. \quad (4.4)$$

Following Figure **4.1** and the law of cosines, the norm of $\boldsymbol{q}$ is:

$$q = \sqrt{k_0^2 + k_\mathrm{s}^2 - 2\ k_0 k_\mathrm{s}\cos\theta_s}. \quad (4.5)$$

Making the assumption of $k_\mathrm{s} \approx k_0$ again, equation (4.5) becomes:

$$q \approx \sqrt{2\ k_0^2 - 2\ k_0^2\cos\theta_s} = \sqrt{2\ k_0^2\cdot\left(1-\cos\theta_s\right)} = 2\ k_0\sin\frac{\theta_s}{2}. \quad (4.6)$$

Equation (4.6) relates q simply to the mean photon energy of the incident X-ray pulse $\hbar c k_0$ and the scattering angle θ_s. An insertion of the expression into equation (4.4) yields:

$$\theta_q \approx \arccos\left(\sin\frac{\theta_s}{2}\right) = \frac{1}{2}\cdot\left(\theta_s - \pi\right). \quad (4.7)$$

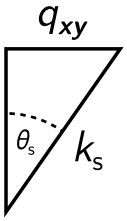

Fig. 4.2: Triangular relationship of the norm of the $\boldsymbol{q}_{xy}$-component and the norm and polar angle of the wave vector of the scattered radiation, k_s and θ_s, respectively.

Equations (4.6) and (4.7) show that both q and θ_q are completely defined by k_0 and θ_s within the Waller-Hartree approximation. These relations hold as long as the change in photon energy due to inelastic scattering is negligible.

Moreover, the azimuthal angle ϕ_q is simply $\phi_q = -\phi_s$ with the azimuthal angle ϕ_s of $\boldsymbol{k}_\mathrm{s}$. This follows from the fact that the corresponding component of $\boldsymbol{k}_0$ is zero in the given coordinate system.

In case $dS/d\Omega$ is measured on a two-dimensional detector in the q_x-q_y-plane, only the projection of full three-dimensional differential scattering signal onto the q_x-q_y-plane has to be considered. It is advantageous then to define all three components of the scattering vector in terms of k_0, q_x, and q_y, meaning that an expression that associates the triple of variables to q_z has to be known. Realising that $\boldsymbol{q}$, its projection $\boldsymbol{q}_{xy}$, and the z-axis in reciprocal space form a right triangle as illustrated in Figure **4.2**, the polar scattering angle θ_s is simply given by the arcsine:

$$\theta_s = \arcsin\frac{q_{xy}}{k_\mathrm{s}} \approx \arcsin\frac{q_{xy}}{k_0}, \tag{4.8}$$

where $q_{xy} = \sqrt{q_x^2 + q_y^2}$ is the norm of $\boldsymbol{q}_{xy}$ and the approximation $k_\mathrm{s} \approx k_0$ is used. An insertion of equation (4.8) into equation (4.6) yields for q:

$$q = 2\ k_0\ \sin\left(\frac{1}{2}\ \arcsin\frac{q_{xy}}{k_0}\right). \tag{4.9}$$

Similarly, an insertion of equation (4.8) into equation (4.7) yields for θ_q:

$$\theta_q = \frac{1}{2}\cdot\left(\arcsin\frac{q_{xy}}{k_0} - \pi\right). \tag{4.10}$$

The azimuthal angle ϕ_q is given as $\phi_q = \arctan\big(q_y/q_x\big)$. The arctangent has to take the quadrant of the point $\big(q_x,\, q_y\big)$ into account.

By insertion of q and θ_q from equations (4.9) and (4.10) into $q_z = q\cos\theta_q$, the q_z-component of $\boldsymbol{q}$ with known values of k_0, q_x, and q_y becomes:

$$q_z = 2\ k_0\ \sin\left(\frac{1}{2}\ \arcsin\frac{q_{xy}}{k_0}\right)\ \cos\left(\frac{1}{2}\cdot\left(\arcsin\frac{q_{xy}}{k_0} - \pi\right)\right). \tag{4.11}$$

With $\cos\big((x-\pi)/2\big) = \sin\big(x/2\big)$ equation (4.11) simplifies to:

$$q_z = 2\ k_0\ \sin^2\left(\frac{1}{2}\ \arcsin\frac{q_{xy}}{k_0}\right), \tag{4.12}$$

and with $2\ \sin^2\big(x/2\big) = 1 - \cos x$ as well as $\cos\big(\arcsin x\big) = \sqrt{1-x^2}$ to:

$$q_z = k_0\cdot\left(1 - \sqrt{1 - \frac{q_{xy}^2}{k_0^2}}\right) = k_0\cdot\left(1 - \sqrt{1 - \frac{q_x^2 + q_y^2}{k_0^2}}\right). \tag{4.13}$$

It is furthermore useful to derive expressions for the minimum and maximum values of the two components q_x and q_y in the detector plane in order to determine the range of values that has to be considered in a calculation. Generally, a stationary detector in the q_x-q_y-plane orthogonal to $\boldsymbol{k}_0$ can only collect photons that are scattered at angles smaller than $\theta_s = 90°$. It follows from the relation $q = 2\ k_0\ \sin\big(\theta_s/2\big)$ given in equation (4.6) that the radial distance q can take values of $q = \sqrt{2}\ k_0$ at most. If scattered photons are detected at angles not above $\theta_s = 60°$, q will be limited to $q = k_0$.

These values can be converted into the minima and maxima of q_x and q_y as follows. Equation (4.9) is solved for q_{xy} first:

$$q_{xy} = k_0\ \sin\left(2\ \arcsin\frac{q}{2\ k_0}\right). \tag{4.14}$$

Insertion of the upper limits $q = \sqrt{2}\,k_0$ and $q = k_0$ into equation (4.14) yields the maxima of q_{xy} now. Hence, all photons scattered at angles of $\theta_s = 90°$ or $\theta_s = 60°$ at most are detected within a circle with radius $q_{xy} = k_0$ or $q_{xy} = \sqrt{3}/2\ k_0$ around the origin of the q_x-q_y-plane, respectively. The single components q_x and q_y are related to q_{xy} and each other by:

$$q_x = \pm\sqrt{q_{xy}^2 - q_y^2}, \qquad \text{or:} \qquad q_y = \pm\sqrt{q_{xy}^2 - q_x^2}. \tag{4.15}$$

5 Properties of Scattering Matrix Elements

The one-electron scattering matrix elements that have been introduced in equations (2.4) and (2.5) have some important and convenient properties that are briefly discussed in the following. To begin with, it is well known that the scattering signal at zero momentum transfer with $\boldsymbol{q} = \mathbf{0} = \big[0, 0, 0\big]$ is proportional to the number of electrons squared. This follows directly from equations (2.5):

$$\begin{aligned} L_{fi}(\mathbf{0}) &= \int_{-\infty}^{+\infty} e^{\iota \mathbf{0}\cdot\boldsymbol{r}}\ \rho_{fi}(\boldsymbol{r})\ d\boldsymbol{r} = \int_{-\infty}^{+\infty} \rho_{fi}(\boldsymbol{r})\ d\boldsymbol{r} \\ &= \int_{-\infty}^{+\infty} \sum_{n=1}^{N_e} \big\langle \varphi_f \,|\, \delta(\boldsymbol{r} - \boldsymbol{r}_n) \,|\, \varphi_i \big\rangle\ d\boldsymbol{r} = \sum_{n=1}^{N_e} \big\langle \varphi_f | \varphi_i \big\rangle = N_e\ \delta_{fi}. \end{aligned} \tag{5.1}$$

Equation (5.1) reveals that at $\boldsymbol{q} = \mathbf{0}$ all off-diagonal scattering matrix elements vanish and that the diagonal elements are equal to the number of electrons N_e. If equation (5.1) is applied to equation (2.12) or (3.17), all contributions to the differential scattering signal $dS/d\Omega$ but the elastic one will vanish, meaning that the scattering is purely elastic at zero momentum transfer. This conclusion may appear trivial in a physical perspective, but it demonstrates that the one-electron scattering matrix elements behave properly at the limit $\boldsymbol{q} = \mathbf{0}$.

On condition that the material system displays inversion symmetry, the one-electron densities or transition densities $\rho_{fi}(\boldsymbol{r})$ in equations (2.5) are either even (*gerade*) or odd (*ungerade*) functions of $\boldsymbol{r}$. If the states $\big|\varphi_f\big\rangle$ and $\big|\varphi_i\big\rangle$ are both *gerade* or *ungerade*, the density $\rho_{fi}(\boldsymbol{r})$ will be even. If only one of the two states is *gerade* and the other is *ungerade*, $\rho_{fi}(\boldsymbol{r})$ will be odd. This has important consequences for the one-electron scattering matrix elements that are Fourier transforms of $\rho_{fi}(\boldsymbol{r})$. For an even density with $\rho_{fi}(-\boldsymbol{r}) = \rho_{fi}(\boldsymbol{r})$, the imaginary part of the scattering matrix element is zero. For an odd density with $\rho_{fi}(-\boldsymbol{r}) = -\rho_{fi}(\boldsymbol{r})$, the real part of the matrix element vanishes. This becomes apparent when Euler's formula $\exp(\iota\boldsymbol{q}\cdot\boldsymbol{r}) = \cos(\boldsymbol{q}\cdot\boldsymbol{r}) + \iota\,\sin(\boldsymbol{q}\cdot\boldsymbol{r})$ is used to express the Fourier transform in equation (2.5) as:

$$\begin{aligned} L_{fi}(\boldsymbol{q}) = \int_{-\infty}^{+\infty} e^{\iota\boldsymbol{q}\cdot\boldsymbol{r}}\ \rho_{fi}(\boldsymbol{r})\ d\boldsymbol{r} &= \int_{-\infty}^{+\infty} \cos(\boldsymbol{q}\cdot\boldsymbol{r})\ \rho_{fi}(\boldsymbol{r})\ d\boldsymbol{r} \\ &\quad + \iota \cdot \int_{-\infty}^{+\infty} \sin(\boldsymbol{q}\cdot\boldsymbol{r})\ \rho_{fi}(\boldsymbol{r})\ d\boldsymbol{r}. \end{aligned} \tag{5.2}$$

Because $\rho_{fi}(\boldsymbol{r})$ is usually real-valued, the integrals on the right-hand side of equation (5.2) are real-valued as well. Considering that the cosine is an even and the sine an odd function of $\boldsymbol{q}\cdot\boldsymbol{r}$, because $\cos(-\boldsymbol{q}\cdot\boldsymbol{r}) = \cos(\boldsymbol{q}\cdot\boldsymbol{r})$

and $\sin(-\boldsymbol{q}\cdot\boldsymbol{r}) = -\sin(\boldsymbol{q}\cdot\boldsymbol{r})$, only one of the two terms in equation (5.2) can differ from zero. The integrands have to be even to allow the integral not to vanish. If the density is even, only the cosine transform will survive and the scattering matrix element will be:

$$L_{fi}(\boldsymbol{q}) = \int_{-\infty}^{+\infty} \cos(\boldsymbol{q}\cdot\boldsymbol{r})\ \rho_{fi}(\boldsymbol{r})\ d\boldsymbol{r}. \tag{5.3}$$

If the density is odd instead, the scattering matrix element will be equal to the sine transform:

$$L_{fi}(\boldsymbol{q}) = \iota \cdot \int_{-\infty}^{+\infty} \sin(\boldsymbol{q}\cdot\boldsymbol{r})\ \rho_{fi}(\boldsymbol{r})\ d\boldsymbol{r}. \tag{5.4}$$

As stated before, the imaginary part of equation (5.3) and the real part of equation (5.4) are zero. Moreover, not only the densities but also the scattering matrix elements in equations (5.3) and (5.4) are even and odd, respectively. This has significant implications for the coherence scattering signal $dS_\mathrm{c}/d\Omega$ in equations (2.18) and (3.22). The products of scattering matrix elements that define the coherence signal are again either real- or imaginary-valued. If the states $\left|\varphi_i\right\rangle$ and $\left|\varphi_j\right\rangle$ are both *gerade* or *ungerade*, the imaginary part of the product will always vanish, since both matrix elements will be real- or imaginary-valued. If only one of the two states is *gerade* and the other is *ungerade*, the real part of the product will be zero, because one matrix element will be real- and the other imaginary-valued. Similarly, the product is even in the first and odd in the second case. These conclusions will be used in both simulations in Part III later on.

Finally, Friedel's law[41,50] that states that a diffraction pattern of a crystal is centrosymmetric irrespective of the symmetry the crystal itself displays is discussed for two-dimensional scattering patterns of atoms or molecules. In X-ray crystallography, Friedel's law follows from the properties of the absolute square of the structure factor that describes the diffraction of a crystal. Here, Friedel's law can be deduced from the properties of the absolute square of one-electron scattering matrix elements of atoms or molecules.

Since the scattering matrix elements are Fourier transforms of real-valued functions, the complex conjugate $L^*_{fi}(\boldsymbol{q})$ is equal to $L_{fi}(-\boldsymbol{q})$:

$$\begin{aligned} L^*_{fi}(\boldsymbol{q}) &= \mathcal{F}^*_{\boldsymbol{r}}\big[\rho_{fi}(\boldsymbol{r})\big](\boldsymbol{q}) = \int_{-\infty}^{+\infty} e^{-\iota\boldsymbol{q}\cdot\boldsymbol{r}}\ \rho_{fi}(\boldsymbol{r})\ d\boldsymbol{r} \\ &= \mathcal{F}_{\boldsymbol{r}}\big[\rho_{fi}(\boldsymbol{r})\big](-\boldsymbol{q}) = L_{fi}(-\boldsymbol{q}). \end{aligned} \tag{5.5}$$

Hence, the absolute square of the scattering matrix element becomes:

$$\left|L_{fi}(\boldsymbol{q})\right|^2 = L^*_{fi}(\boldsymbol{q})\ L_{fi}(\boldsymbol{q}) = L_{fi}(-\boldsymbol{q})\ L_{fi}(\boldsymbol{q}). \tag{5.6}$$

The absolute square in equation (5.6) is clearly invariant under inversion of the coordinates in reciprocal space $\boldsymbol{q} \longrightarrow (-\boldsymbol{q})$:

$$\left|L_{fi}\big(\big[q_x, q_y, q_z\big]\big)\right|^2 = \left|L_{fi}\big(\big[-q_x, -q_y, -q_z\big]\big)\right|^2. \tag{5.7}$$

On a two-dimensional detector, however, an inversion of the coordinates means that only two components of $\boldsymbol{q}$ change their signs. Centrosymmetry of a two-dimensional scattering pattern in the q_x-q_y plane implies:

$$\left|L_{fi}\big(\big[q_x, q_y, q_z\big]\big)\right|^2 = \left|L_{fi}\big(\big[-q_x, -q_y, q_z\big]\big)\right|^2. \tag{5.8}$$

Equation (5.8) will only be true if the following condition is fulfilled:

$$L^*_{fi}\big(\big[q_x, q_y, q_z\big]\big) = L_{fi}\big(\big[-q_x, -q_y, q_z\big]\big). \tag{5.9}$$

Equation (5.9) requires that the Fourier transform of $\rho_{fi}(\boldsymbol{r})$ in z-direction $\mathcal{F}_z\big[\rho_{fi}(\boldsymbol{r})\big](q_z)$ has to be real-valued. Following equation (5.2), that means that $\mathcal{F}_z\big[\rho_{fi}(\boldsymbol{r})\big](q_z)$ has to be defined by the cosine transform alone:

$$\mathcal{F}_z\big[\rho_{fi}(\boldsymbol{r})\big](q_z) = \int_{-\infty}^{+\infty} \cos q_z z\ \rho_{fi}\big(\big[x, y, z\big]\big)\ dz, \tag{5.10}$$

and that $\rho_{fi}(\boldsymbol{r})$ has to be an even function of z:

$$\rho_{fi}\big(\big[x, y, -z\big]\big) = \rho_{fi}\big(\big[x, y, z\big]\big). \tag{5.11}$$

Equations (5.8) and (5.11) show that Friedel's law is valid for two-dimensional scattering patterns of atoms and molecules on two conditions: First, the one-electron densities or one-electron transition densities $\rho_{fi}(\boldsymbol{r})$ have to be invariant under reflection through the detector plane in real space. Second, $dS/d\Omega$ has to be described solely in terms of absolute squares of one-electron scattering matrix elements. The coherence contribution that depends on products of different matrix elements can lead to an invalidation of Friedel's law even in situations where equation (5.11) is fulfilled.

6 Analytic Solutions to Scattering Matrix Elements of the Hydrogen Atom

If the X-ray photons are scattered by a hydrogen-like atom in a non-stationary state, the scattering matrix elements $L_{fi}(\boldsymbol{q}) = \langle \varphi_f | \hat{L} | \varphi_i \rangle$ in equation (2.4) can be solved analytically. The usual separation of the wave function in spherical coordinates, however, leads to a radial integral for which no analytic solution is known. Following the approach of Schnaidt [38], a completely analytic expression without remaining integrals can be obtained by separating in parabolic coordinates instead. Before such a solution is derived, the problem arising from the spherical separation is briefly discussed.

The wave function of the hydrogen atom in spherical coordinate space is [51]:

$$\varphi_{n,l,m}(r, \theta_r, \phi_r) = R_{n,l}(r)\ Y_{l,m}(\theta_r, \phi_r), \tag{6.1}$$

where r is the radial distance and $R_{n,l}(r)$ is the radial part:

$$R_{n,l}(r) = -\sqrt{\frac{(n-l-1)!}{2n(n+l)!}} \left(\frac{2}{n}\right)^{\frac{3}{2}} \left(\frac{2r}{n}\right)^{l} L_{n-l-1}^{2l+1}\left(\frac{2r}{n}\right) e^{-\frac{r}{n}}. \tag{6.2}$$

The function $L_{n-l-1}^{2l+1}(2r/n)$ in equation (6.2) is an associated Laguerre polynomial [52]. Moreover, the variables θ_r and ϕ_r in equation (6.1) are the polar and azimuthal angles and $Y_{l,m}(\theta_r, \phi_r)$ is a spherical harmonic. n, l, and m are the principal, angular momentum, and magnetic quantum numbers.

The scattering operator $\hat{L}$ can be expanded in products of a spherical Bessel function of the first kind $j_l(qr)$ and two spherical Harmonics [53]:

$$\hat{L} = e^{\iota \boldsymbol{q}\cdot\boldsymbol{r}} = 4\pi \cdot \sum_{l}^{\infty} \sum_{m}^{\infty} \iota^l\ j_l(qr)\ Y_{l,m}^*(\theta_q, \phi_q)\ Y_{l,m}(\theta_r, \phi_r), \tag{6.3}$$

where q, θ_q, and ϕ_q are the spherical components of the scattering vector $\boldsymbol{q}$ and $\hat{L}$ refers to a single electron only.

With equations (6.1) and (6.3), the scattering matrix element $L_{fi}(\boldsymbol{q})$ of any two eigenstates of the hydrogen atom is:

$$\begin{aligned} \left\langle \varphi_{n_f,l_f,m_f} \,\middle|\, \hat{L} \,\middle|\, \varphi_{n_i,l_i,m_i} \right\rangle &= 4\pi \cdot \sum_{l}^{\infty} \sum_{m}^{\infty} \iota^l\ Y_{l,m}^*(\theta_q, \phi_q) \\ &\times \int_0^{\infty} r^2\ R_{n_f,l_f}(r)\ R_{n_i,l_i}(r)\ j_l(qr)\ dr \cdot \int_0^{\pi} \sin\theta_r \\ &\times \int_0^{2\pi} Y_{l,m}(\theta_r, \phi_r)\ Y_{l_i,m_i}(\theta_r, \phi_r)\ Y_{l_f,m_f}^*(\theta_r, \phi_r)\ d\phi_r\ d\theta_r. \end{aligned} \tag{6.4}$$

The scattering matrix element in equation (6.4) separates into an integral over r and a double integral over θ_r and ϕ_r. The latter can be solved in terms of Clebsch-Gordan coefficients $\langle l_1, m_1, l_2, m_2 | l_1, l_2, l, m \rangle$ [54]:

$$\begin{aligned} &\left\langle \varphi_{n_f,l_f,m_f} \,\middle|\, \hat{L} \,\middle|\, \varphi_{n_i,l_i,m_i} \right\rangle = 4\pi \cdot \sum_l \; \iota^l \; \sqrt{\frac{(2l+1)(2l_i+1)}{4\pi(2l_f+1)}} \\ &\times \langle l, 0, l_i, 0 | l, l_i, l_f, 0 \rangle \; \langle l, m, l_i, m_i | l, l_i, l_f, m_f \rangle \; Y^*_{l,m}(\theta_q, \phi_q) \\ &\times \int_0^\infty \; r^2 \; R_{n_f,l_f}(r) \; R_{n_i,l_i}(r) \; j_l(qr) \; dr. \end{aligned} \tag{6.5}$$

The Clebsch-Gordan coefficients are non-zero only when $m = m_f - m_i$ and the sum over m reduces to a single term in equation (6.5). Similarly, the angular momentum quantum numbers have to fulfill the triangular condition $|l_f - l_i| \leq l \leq l_f + l_i$. The sum over l is restricted accordingly. The remaining radial integral in equation (6.5) contains the product of the spherical Bessel function and two spherical harmonics:

$$\begin{aligned} &\int_0^\infty \; r^2 \; R_{n_f,l_f}(r) \; R_{n_i,l_i}(r) \; j_l(qr) \; dr = N_r \cdot \int_0^\infty \; r^2 \; \left(\frac{2r}{n_f}\right)^{l_f} \\ &\times \left(\frac{2r}{n_i}\right)^{l_i} \; L^{2l_f+1}_{n_f-l_f-1}\left(\frac{2r}{n_f}\right) \; L^{2l_i+1}_{n_i-l_i-1}\left(\frac{2r}{n_i}\right) \; j_l(qr) \; e^{-\nu r} \; dr, \end{aligned} \tag{6.6}$$

where $\nu = (n_f + n_i)/(n_f n_i)$ and the coefficients N_r are:

$$N_r = 4 \; \sqrt{\frac{(n_f - l_f - 1)!}{n_f (n_f + l_f)!}} \; \sqrt{\frac{(n_i - l_i - 1)!}{n_i (n_i + l_i)!}} \; (n_f n_i)^{-\frac{3}{2}}. \tag{6.7}$$

It has already been mentioned that no analytic solution to the integral in equation (6.6) is known. A direct evaluation of the scattering matrix elements in spherical coordinates would thus necessitate the numerical evaluation of equation (6.6). Considering that there is one integral for every value of l in equation (6.5) and that potentially thousands of matrix elements are required to achieve convergence of equation (2.12), such a task can become "numerically challenging" even for the hydrogen atom [25].

Alternatively, the scattering matrix element can be evaluated in parabolic coordinates without the need for numerical integration. This approach has already been used by Fritz Schnaidt in 1934 to discuss the "discontinuous Compton spectrum of hydrogen" in its 1s ground state. [38] His equations are generalised for scattering matrix elements of any two eigenstates of the hydrogen atom in the following.

The wave function of the hydrogen atom in parabolic coordinate space is [51]:

$$\begin{aligned}\varphi_{n,n_1,n_2}(\xi,\eta,\phi) = N_{n,n_1,n_2}\ (\xi\eta)^{\frac{m}{2}}\ e^{-\frac{\xi+\eta}{2n}} \\ \times L^m_{n_1}\left(\frac{\xi}{n}\right)\ L^m_{n_2}\left(\frac{\eta}{n}\right)\ e^{\pm\iota m\phi}.\end{aligned} \tag{6.8}$$

Equation (6.8) contains two associated Laguerre polynomials that depend on one of the parabolic coordinates ξ and η each. The third coordinate is the azimuthal angle ϕ. n and m are the principal and magnetic quantum numbers of the eigenstate. n_1 and n_2 are parabolic quantum numbers that are related to n and m by $n = n_1 + n_2 + m + 1$. The principal quantum number is a positive integer, m, n_1, and n_2 are non-negative integers. The factor N_{n,n_1,n_2} is a normalisation constant that will be derived later.

The scattering operator $\hat{L}$ and the integral over the electronic coordinates can be written in parabolic coordinates by means of the following relations:

$$\begin{aligned}&x = \sqrt{\xi\eta}\ \cos\phi, \qquad y = \sqrt{\xi\eta}\ \sin\phi, \qquad z = \frac{\xi-\eta}{2}, \\ &r = \frac{\xi+\eta}{2}, \qquad dx\ dy\ dz = \frac{\xi+\eta}{4}\ d\xi\ d\eta\ d\phi,\end{aligned} \tag{6.9}$$

where x, y, and z are the Cartesian components of $\boldsymbol{r}$. The coordinate system is now defined such that the scattering vector $\boldsymbol{q}$ is aligned with the z-axis. This implies that the scattering matrix elements is preliminary reduced to just one dimension in reciprocal space. An extension to all three dimensions is achieved by rotation of the coordinate system later on. Hence, the scattering operator $\hat{L}$ for one electron becomes:

$$\hat{L}_z = e^{\iota q \boldsymbol{e}_z\cdot\boldsymbol{r}} = e^{\iota q z} = e^{\iota q\frac{\xi-\eta}{2}}, \tag{6.10}$$

where $\boldsymbol{e}_z$ is the unit vector in z-direction. With equations (6.8) to (6.10), the one-dimensional scattering matrix element for any two eigenstates of the hydrogen atom in parabolic coordinate space is:

$$\begin{aligned}&\left\langle \varphi_{n_f,n_{f_1},n_{f_2}} \,\middle|\, \hat{L}_z \,\middle|\, \varphi_{n_i,n_{i_1},n_{i_2}} \right\rangle = N_{n_f,n_{f_1},n_{f_2}}\ N_{n_i,n_{i_1},n_{i_2}} \\ &\times \int_0^\infty \int_0^\infty \frac{\xi+\eta}{4}\ e^{-\left(\xi+\eta\right)\left(\frac{1}{2n_f}+\frac{1}{2n_i}\right)}\ (\xi\eta)^{\frac{m_f+m_i}{2}}\ e^{\iota q\frac{\xi-\eta}{2}} \\ &\times L^{m_f}_{n_{f_1}}\left(\frac{\xi}{n_f}\right)\ L^{m_f}_{n_{f_2}}\left(\frac{\eta}{n_f}\right)\ L^{m_i}_{n_{i_1}}\left(\frac{\xi}{n_i}\right)\ L^{m_i}_{n_{i_2}}\left(\frac{\eta}{n_i}\right)\ d\eta\ d\xi \\ &\times \int_0^{2\pi} e^{\pm\iota(m_i-m_f)\phi}\ d\phi.\end{aligned} \tag{6.11}$$

The integral over ϕ in the last line of equation (6.11) is the integral representation of the Kronecker delta multiplied with 2π:

$$\int_0^{2\pi} e^{\pm\iota(m_i - m_f)\phi}\, d\phi = 2\pi\ \delta_{m_i m_f}. \tag{6.12}$$

Equation (6.12) implies the selection rule $\Delta m = 0$. With $m_f = m_i = m$ and $\kappa = \big(1/(2n_f) + 1/(2n_i)\big)$, equation (6.11) becomes:

$$\begin{aligned}\left\langle \varphi_{n_f n_{f_1} n_{f_2}} \,\middle|\, \hat{L}_z \,\middle|\, \varphi_{n_i, n_{i_1}, n_{i_2}} \right\rangle &= \frac{\pi}{2}\ N_{n_f, n_{f_1}, n_{f_2}}\ N_{n_i, n_{i_1}, n_{i_2}} \\ \times \int_0^\infty \int_0^\infty \big(\xi + \eta\big)\ e^{-(\xi+\eta)\kappa}\ \big(\xi\eta\big)^m\ e^{\iota q \frac{\xi-\eta}{2}} \\ \times L^m_{n_{f_1}}\left(\frac{\xi}{n_f}\right) L^m_{n_{f_2}}\left(\frac{\eta}{n_f}\right) L^m_{n_{i_1}}\left(\frac{\xi}{n_i}\right) L^m_{n_{i_2}}\left(\frac{\eta}{n_i}\right) d\eta\ d\xi.\end{aligned} \tag{6.13}$$

The sum $\xi + \eta$ in the second line of equation (6.13) contains both parabolic coordinates and prohibits the separation of the two remaining integrals. This problem can be solved, however, by replacing $\big(\xi+\eta\big)\cdot\exp\big(-\big(\xi+\eta\big)\kappa\big)$ with the negative partial derivative of the exponential function:

$$\big(\xi + \eta\big)\ e^{-(\xi+\eta)\kappa} = -\frac{\partial}{\partial\kappa}\ e^{-(\xi+\eta)\kappa}. \tag{6.14}$$

With equation (6.14) both integrals in equation (6.13) are fully separable:

$$\begin{aligned}\left\langle \varphi_{n_f, n_{f_1}, n_{f_2}} \,\middle|\, \hat{L}_z \,\middle|\, \varphi_{n_i, n_{i_1}, n_{i_2}} \right\rangle &= -\frac{\pi}{2}\ N_{n_f, n_{f_1}, n_{f_2}}\ N_{n_i, n_{i_1}, n_{i_2}} \\ \times \frac{\partial}{\partial\kappa}\Bigg(\int_0^\infty \xi^m\ e^{-\xi\left(\kappa - \frac{\iota q}{2}\right)}\ L^m_{n_{f_1}}\left(\frac{\xi}{n_f}\right) L^m_{n_{i_1}}\left(\frac{\xi}{n_i}\right) d\xi \\ \times \int_0^\infty \eta^m\ e^{-\eta\left(\kappa + \frac{\iota q}{2}\right)}\ L^m_{n_{f_2}}\left(\frac{\eta}{n_f}\right) L^m_{n_{i_2}}\left(\frac{\eta}{n_i}\right) d\eta \Bigg).\end{aligned} \tag{6.15}$$

Both integrands in equation (6.15) are a product of two associated Laguerre polynomials with an exponential function and a power of the variable of integration. A solution for this kind of integral is known from literature [55]:

$$\begin{aligned}
&\int_0^\infty \; x^\alpha \; e^{-x\beta} \; L_q^\alpha\big(\lambda x\big) \; L_p^\alpha\big(\mu x\big) \; dx \\
&= \frac{\Gamma\big(p+q+\alpha+1\big)}{p!\; q!} \; \frac{(\beta-\lambda)^q \cdot (\beta-\mu)^p}{\beta^{(p+q+\alpha+1)}} \\
&\quad \times {}_2F_1\left(-p,\; -q;\; -p-q-\alpha;\; \frac{\beta \;\; (\beta-\lambda-\mu)}{(\beta-\lambda)\,(\beta-\mu)} \right).
\end{aligned} \tag{6.16}$$

Equation (6.16) is valid under the conditions $\mathrm{Re}\big(\alpha\big) > -1$ and $\mathrm{Re}\big(b\big) > 0$. With $\mathrm{Re}\big(\alpha\big) = m \geq 0$ and $\mathrm{Re}\big(\beta\big) = \kappa > 0$, both conditions are fulfilled here. The functions $\Gamma\big(x\big)$ and ${}_2F_1\left(a,b;c;z\right)$ are the Gamma function and the Gaussian hypergeometric function, respectively.

In order to avoid lengthy equations in the following, several constants and functions are defined now:

$$\gamma_1 = \frac{\Gamma\big(m+n_{f_1}+n_{i_1}+1\big)}{n_{f_1}!\; n_{i_1}!}, \tag{6.17}$$

$$\gamma_2 = \frac{\Gamma\big(m+n_{f_2}+n_{i_2}+1\big)}{n_{f_2}!\; n_{i_2}!}, \tag{6.18}$$

$$g_1(\kappa) = \frac{\left(\kappa - \frac{\iota q}{2} - \frac{1}{n_f}\right)^{n_{f_1}} \; \left(\kappa - \frac{\iota q}{2} - \frac{1}{n_i}\right)^{n_{i_1}}}{\left(\kappa - \frac{\iota q}{2}\right)^{m+n_{f_1}+n_{i_1}+1}}, \tag{6.19}$$

$$g_2(\kappa) = \frac{\left(\kappa + \frac{\iota q}{2} - \frac{1}{n_f}\right)^{n_{f_2}} \; \left(\kappa + \frac{\iota q}{2} - \frac{1}{n_i}\right)^{n_{i_2}}}{\left(\kappa + \frac{\iota q}{2}\right)^{m+n_{f_2}+n_{i_2}+1}}, \tag{6.20}$$

$$h_1(\kappa) = {}_2F_1\left(-n_{i_1},\; -n_{f_1};\; -m-n_{i_1}-n_{f_1};\; i_1(\kappa)\right), \tag{6.21}$$

$$i_1(\kappa) = \frac{\left(\kappa - \frac{\iota q}{2}\right) \; \left(\kappa - \frac{\iota q}{2} - \frac{1}{n_f} - \frac{1}{n_i}\right)}{\left(\kappa - \frac{\iota q}{2} - \frac{1}{n_f}\right) \; \left(\kappa - \frac{\iota q}{2} - \frac{1}{n_i}\right)}, \tag{6.22}$$

$$h_2(\kappa) = {}_2F_1\left(-n_{i_2},\; -n_{f_2};\; -m-n_{i_2}-n_{f_2};\; i_2(\kappa)\right), \tag{6.23}$$

$$i_2(\kappa) = \frac{\left(\kappa + \frac{\iota q}{2}\right) \; \left(\kappa + \frac{\iota q}{2} - \frac{1}{n_f} - \frac{1}{n_i}\right)}{\left(\kappa + \frac{\iota q}{2} - \frac{1}{n_f}\right) \; \left(\kappa + \frac{\iota q}{2} - \frac{1}{n_i}\right)}. \tag{6.24}$$

With equations (6.16) and (6.17) to (6.24), equation (6.15) shortens to:

$$\begin{aligned}\left\langle \varphi_{n_f,n_{f_1},n_{f_2}} \,\middle|\, \hat{L}_z \,\middle|\, \varphi_{n_i,n_{i_1},n_{i_2}} \right\rangle &= -\frac{\pi}{2}\; N_{n_f,n_{f_1},n_{f_2}}\; N_{n_i,n_{i_1},n_{i_2}} \\ \times\, \gamma_1\; \gamma_2 \cdot \frac{\partial}{\partial\kappa} &\left(g_1(\kappa)\; g_2(\kappa)\; h_1(\kappa)\; h_2(\kappa) \right).\end{aligned} \tag{6.25}$$

By action of the partial derivative $\partial/\partial\kappa$ upon the product $g_1(\kappa)\, g_2(\kappa)\, h_1(\kappa)\, h_2(\kappa)$, equation (6.25) becomes:

$$\begin{aligned}\left\langle \varphi_{n_f,n_{f_1},n_{f_2}} \,\middle|\, \hat{L}_z \,\middle|\, \varphi_{n_i,n_{i_1},n_{i_2}} \right\rangle &= -\frac{\pi}{2}\; N_{n_f,n_{f_1},n_{f_2}}\; N_{n_i,n_{i_1},n_{i_2}} \\ \times\, \gamma_1\; \gamma_2 \cdot \Big[&\left(g_1'(\kappa)\; g_2(\kappa) + g_1(\kappa)\; g_2'(\kappa) \right) \cdot h_1(\kappa)\; h_2(\kappa) \\ &+ g_1(\kappa)\; g_2(\kappa) \cdot \left(h_1'(\kappa)\; h_2(\kappa) + h_1(\kappa)\; h_2'(\kappa) \right) \Big].\end{aligned} \tag{6.26}$$

Equation (6.26) contains derivatives $f'(\kappa)$ of the six functions defined in equations (6.19) to (6.24). These derivatives are:

$$g_1'(\kappa) = d_{g_1}(\kappa)\; g_1(\kappa), \tag{6.27}$$

$$d_{g_1}(\kappa) = \left(\frac{n_{f_1}}{\kappa - \frac{\iota q}{2} - \frac{1}{n_f}} + \frac{n_{i_1}}{\kappa - \frac{\iota q}{2} - \frac{1}{n_i}} - \frac{m + n_{f_1} + n_{i_1} + 1}{\kappa - \frac{\iota q}{2}} \right), \tag{6.28}$$

$$g_2'(\kappa) = d_{g_2}(\kappa)\; g_2(\kappa), \tag{6.29}$$

$$d_{g_2}(\kappa) = \left(\frac{n_{f_2}}{\kappa + \frac{\iota q}{2} - \frac{1}{n_f}} + \frac{n_{i_2}}{\kappa + \frac{\iota q}{2} - \frac{1}{n_i}} - \frac{m + n_{f_2} + n_{i_2} + 1}{\kappa + \frac{\iota q}{2}} \right), \tag{6.30}$$

$$h_1'(\kappa) = -d_{h_1}\; i_1'(\kappa)\; \tilde{h}_1(\kappa), \tag{6.31}$$

$$d_{h_1} = \frac{n_{i_1}\; n_{f_1}}{m + n_{i_1} + n_{f_1}}, \tag{6.32}$$

$$i_1'(\kappa) = d_{i_1}(\kappa) \cdot \Big(1 - i_1(\kappa)\Big), \tag{6.33}$$

$$d_{i_1}(\kappa) = \left(\frac{1}{\kappa - \frac{\iota q}{2} - \frac{1}{n_f}} + \frac{1}{\kappa - \frac{\iota q}{2} - \frac{1}{n_i}}\right), \tag{6.34}$$

$$\tilde{h}_1(\kappa) = {}_2F_1\Big(1 - n_{i_1},\ 1 - n_{f_1};\ 1 - m - n_{i_1} - n_{f_1};\ i_1(\kappa)\Big), \tag{6.35}$$

$$h_2'(\kappa) = -d_{h_2}\ i_2'(\kappa)\ \tilde{h}_2(\kappa), \tag{6.36}$$

$$d_{h_2} = \frac{n_{i_2}\ n_{f_2}}{m + n_{i_2} + n_{f_2}}, \tag{6.37}$$

$$i_2'(\kappa) = d_{i_2}(\kappa) \cdot \Big(1 - i_2(\kappa)\Big), \tag{6.38}$$

$$d_{i_2}(\kappa) = \left(\frac{1}{\kappa + \frac{\iota q}{2} - \frac{1}{n_f}} + \frac{1}{\kappa + \frac{\iota q}{2} - \frac{1}{n_i}}\right), \tag{6.39}$$

$$\tilde{h}_2(\kappa) = {}_2F_1\Big(1 - n_{i_2},\ 1 - n_{f_2};\ 1 - m - n_{i_2} - n_{f_2};\ i_2(\kappa)\Big). \tag{6.40}$$

With equations (6.27) to (6.40) and by rearrangement of terms, the scattering matrix element in equation (6.26) becomes:

$$\begin{aligned}\left\langle \varphi_{n_f,n_{f_1},n_{f_2}} \,\middle|\, \hat{L}_z \,\middle|\, \varphi_{n_i,n_{i_1},n_{i_2}} \right\rangle &= -\frac{\pi}{2}\ N_{n_f,n_{f_1},n_{f_2}}\ N_{n_i,n_{i_1},n_{i_2}} \\ \times\ \gamma_1\ \gamma_2\ g_1(\kappa)\ g_2(\kappa) \cdot \Big[&\Big(d_{g_1}(\kappa) + d_{g_2}(\kappa)\Big) \cdot h_1(\kappa)\ h_2(\kappa) \\ &- d_{h_1}\ d_{i_1}(\kappa)\ \tilde{h}_1(\kappa)\ h_2(\kappa) \cdot \Big(1 - i_1(\kappa)\Big) \\ &- d_{h_2}\ d_{i_2}(\kappa)\ h_1(\kappa)\ \tilde{h}_2(\kappa) \cdot \Big(1 - i_2(\kappa)\Big)\Big].\end{aligned} \tag{6.41}$$

Equation (6.41) does not contain remaining derivatives or integrals. The expression only involves the functions defined above. The normalisation constant, however, is unknown so far. It is derived in the following.

Since normalisation ensures that the inner product of the wave function with itself equals unity:

$$\left\langle \varphi_{n,n_1,n_2} \middle| \varphi_{n,n_1,n_2} \right\rangle = 1, \tag{6.42}$$

the normalization constant can be obtained as the inverse square root of the matrix element of the unnormalised state $\left|\tilde{\varphi}_{n,n_1,n_2}\right\rangle$:

$$N_{n,n_1,n_2} = \left\langle \tilde{\varphi}_{n,n_1,n_2} \middle| \tilde{\varphi}_{n,n_1,n_2} \right\rangle^{-1/2}. \tag{6.43}$$

The matrix element in equation (6.43) corresponds to equation (6.15) in the limits of $n_f = n_i = n$ and $q = 0$:

$$\begin{aligned} \left\langle \tilde{\varphi}_{n,n_1,n_2} \middle| \tilde{\varphi}_{n,n_1,n_2} \right\rangle = -\frac{\pi}{2} \frac{\partial}{\partial \kappa} \Bigg(& \int_0^\infty \xi^m \, e^{-\xi\kappa} \left[L_{n_1}^m \left(\frac{\xi}{n} \right) \right]^2 d\xi \\ & \times \int_0^\infty \eta^m \, e^{-\eta\kappa} \left[L_{n_2}^m \left(\frac{\eta}{n} \right) \right]^2 d\eta \Bigg). \end{aligned} \tag{6.44}$$

The integrals in equation (6.44) are solved by application of equation (6.16) again. The integral over ξ becomes:

$$\begin{aligned} & \int_0^\infty \xi^m \, e^{-\xi\kappa} \left[L_{n_1}^m \left(\frac{\xi}{n} \right) \right]^2 d\xi = \frac{\Gamma\left(2n_1 + m + 1\right)}{\left(n_1!\right)^2} \, \frac{\left(\kappa - \frac{1}{n}\right)^{2n_1}}{\kappa^{2n_1+m+1}} \\ & \times {}_2F_1 \left(-n_1, \; -n_1; \; -2n_1 - m; \; \frac{\kappa\left(\kappa - \frac{2}{n}\right)}{\left(\kappa - \frac{1}{n}\right)^2} \right). \end{aligned} \tag{6.45}$$

Since $\kappa = 1/n$ in equation (6.45), the denominator of the fourth argument of the hypergeometric function is zero. The resulting singularity requires that the corresponding terms vanish. For this purpose the hypergeometric function is replaced by its corresponding power series, leading to:

$$\begin{aligned} & \int_0^\infty \xi^m \, e^{-\xi\kappa} \left[L_{n_1}^m \left(\frac{\xi}{n} \right) \right]^2 d\xi = \frac{\Gamma\left(2n_1 + m + 1\right)}{\left(n_1!\right)^2} \, \frac{\left(\kappa - \frac{1}{n}\right)^{2n_1}}{\kappa^{2n_1+m+1}} \\ & \times \sum_{i=0}^{\infty} \frac{\left(-n_1\right)_{(i)}^2}{\left(-2n_1 - m\right)_{(i)}} \, \frac{1}{i!} \, \frac{\kappa^i \cdot \left(\kappa - \frac{2}{n}\right)^i}{\left(\kappa - \frac{1}{n}\right)^{2i}}. \end{aligned} \tag{6.46}$$

Here, $(x)_{(i)}$ is the Pochhammer symbol with rising factorial.

Only the term with $i = n_1$ in equation (6.46) has to be considered. In this case the enumerator of the second fraction cancels with the denominator of the fifth fraction. All other terms are either singular ($i > n_1$) or zero ($i < n_1$). Hence, equation (6.46) simplifies to:

$$\begin{aligned}\int_0^\infty \xi^m \, e^{-\xi\kappa} \left[L_{n_1}^m\left(\frac{\xi}{n}\right)\right]^2 d\xi = \frac{\Gamma\big((2n_1+m+1)\big)}{\big(n_1!\big)^3} \, \frac{\big(\kappa-\frac{2}{n}\big)^{n_1}}{\kappa^{n_1+m+1}} \\ \times \frac{\big(-n_1\big)_{(n_1)}^2}{\big(-2n_1-m\big)_{(n_1)}}.\end{aligned} \tag{6.47}$$

Applying equation (6.47) to both integrals in equation (6.44), the matrix element becomes:

$$\begin{aligned}\Big\langle \tilde{\varphi}_{n,n_1,n_2}\Big|\tilde{\varphi}_{n,n_1,n_2}\Big\rangle = -\frac{\pi}{2} \, \frac{\Gamma\big(2n_1+m+1\big)}{\big(n_1!\big)^3} \, \frac{\Gamma\big(2n_2+m+1\big)}{\big(n_2!\big)^3} \\ \times \frac{\big(-n_1\big)_{(n_1)}^2}{\big(-2n_1-m\big)_{(n_1)}} \, \frac{\big(-n_2\big)_{(n_2)}^2}{\big(-2n_2-m\big)_{(n_2)}} \, \frac{\partial}{\partial\kappa} \, \frac{\big(\kappa-\frac{2}{n}\big)^{n_1+n_2}}{\kappa^{n_1+n_2+2m+2}}.\end{aligned} \tag{6.48}$$

An evaluation of the derivative and subsequent substitution of $1/n$ for κ:

$$\begin{aligned}\frac{\partial}{\partial\kappa}\frac{\big(\kappa-\frac{2}{n}\big)^{n_1+n_2}}{\kappa^{n_1+n_2+2m+2}} &= -\left(-1\right)^{n_1+n_2} \, 2n^{2m+3} \cdot \big(n_1+n_2+m+1\big) \\ &= -\left(-1\right)^{n_1+n_2} \, 2n^{2m+4},\end{aligned} \tag{6.49}$$

lead to:

$$\begin{aligned}\Big\langle \tilde{\varphi}_{n,n_1,n_2}\Big|\tilde{\varphi}_{n,n_1,n_2}\Big\rangle = \left(-1\right)^{n_1+n_2} \, n^{2m+4} \, \pi \, \frac{\Gamma\big(2n_1+m+1\big)}{\big(n_1!\big)^3} \\ \times \frac{\Gamma\big(2n_2+m+1\big)}{\big(n_2!\big)^3} \, \frac{\big(-n_1\big)_{(n_1)}^2}{\big(-2n_1-m\big)_{(n_1)}} \, \frac{\big(-n_2\big)_{(n_2)}^2}{\big(-2n_2-m\big)_{(n_2)}}.\end{aligned} \tag{6.50}$$

Equation (6.50) can be simplified further by writing the Gamma functions and the Pochhammer symbols in terms of factorials. Using the relations $\Gamma\big(x+1\big) = x!$ and:

$$\big(-x\big)_{(i)} = \prod_{k=0}^{i-1} \left(k-x\right) = \left(-1\right)^i \cdot \prod_{k=0}^{i-1} \left(x-k\right) = \left(-1\right)^i \, \frac{x!}{(x-i)!}, \tag{6.51}$$

equation (6.50) becomes:

$$\left\langle \tilde{\varphi}_{n,n_1,n_2} \middle| \tilde{\varphi}_{n,n_1,n_2} \right\rangle = n^{2m+4}\ \pi\ \frac{(n_1+m)!}{n_1!}\ \frac{(n_2+m)!}{n_2!}. \tag{6.52}$$

Following equation (6.43), the normalisation constant is simply the inverse square root of equation (6.52):

$$N_{n,n_1,n_2} = \frac{1}{n^{m+2}}\ \sqrt{\frac{1}{\pi}\ \frac{n_1!}{(m+n_1)!}\ \frac{n_2!}{(m+n_2)!}}. \tag{6.53}$$

The constants and functions in equation (6.41) can now be replaced by their definitions given in equations (6.17) to (6.24), (6.27) to (6.40), and (6.53):

$$\begin{aligned}
&\left\langle \varphi_{n_f,n_{f_1},n_{f_2}} \,\middle|\, \hat{L}_z \,\middle|\, \varphi_{n_i,n_{i_1},n_{i_2}} \right\rangle = \frac{4^{m+2}\ n_i^{m+3} n_f^{m+3}}{\sqrt{n_{i_1}!\ n_{i_2}!\ n_{f_1}!\ n_{f_2}!}} \\
&\times \frac{(n_{i_1}+n_{f_1}+m)!}{\sqrt{(n_{i_1}+m)!\ (n_{f_1}+m)!}}\ \frac{(n_{i_2}+n_{f_2}+m)!}{\sqrt{(n_{i_2}+m)!\ (n_{f_2}+m)!}} \\
&\times \frac{\big(n_i - n_f - \iota n_i n_f q\big)^{n_{i_1}} \big(-n_i + n_f - \iota n_i n_f q\big)^{n_{f_1}}}{\big(n_i + n_f - \iota n_i n_f q\big)^{n_{i_1}+n_{f_1}+m}} \\
&\times \frac{\big(n_i - n_f + \iota n_i n_f q\big)^{n_{i_2}} \big(-n_i + n_f + \iota n_i n_f q\big)^{n_{f_2}}}{\big(n_i + n_f + \iota n_i n_f q\big)^{n_{i_2}+n_{f_2}+m}} \\
&\times \frac{1}{(n_i+n_f)^2 + n_i^2 n_f^2 q^2}\ \frac{1}{(n_i-n_f)^2 + n_i^2 n_f^2 q^2} \\
&\times \left(\frac{n_i n_f q - \iota \cdot (n_{i_1} - n_{i_2} + n_{f_1} - n_{f_2})}{(n_i+n_f)^2 + n_i^2 n_f^2 q^2} \cdot \mathfrak{F}_{0,0}(q) \right. \\
&\quad - \frac{2\ \iota}{(n_i-n_f)^2 + n_i^2 n_f^2 q^2}\ \frac{n_{i_1} n_{f_1}}{n_{i_1}+n_{f_1}+m} \cdot \mathfrak{F}_{1,0}(q) \\
&\quad \left. + \frac{2\ \iota}{(n_i-n_f)^2 + n_i^2 n_f^2 q^2}\ \frac{n_{i_2} n_{f_2}}{n_{i_2}+n_{f_2}+m} \cdot \mathfrak{F}_{0,1}(q) \right) \cdot q.
\end{aligned} \tag{6.54}$$

The function $\mathfrak{F}_{\alpha,\beta}(q)$ in equation (6.54) is a product of two Gaussian hypergeometric functions with the same fourth argument:

$$\begin{aligned}\mathfrak{F}_{\alpha,\beta}(q) = {}_2F_1\left(\alpha - n_{i_1},\ \alpha - n_{f_1};\ \alpha - n_{i_1} - n_{f_1} - m;\ z(q)\right) \\ \times {}_2F_1\left(\beta - n_{i_2},\ \beta - n_{f_2};\ \beta - n_{i_2} - n_{f_2} - m;\ z(q)\right),\end{aligned} \tag{6.55}$$

where:

$$z(q) = 1 + \frac{4\ n_i n_f}{\left(n_i - n_f\right)^2 + n_i^2 n_f^2 q^2}. \tag{6.56}$$

The indices α and β of $\mathfrak{F}_{\alpha,\beta}(q)$ are either zero or one. Moreover, the two hypergeometric functions ${}_2F_1\left(a, b; c; z\right)$ in equation (6.55) are polynomials of degree $\lambda = -\max\left(a, b\right)$ in z:

$${}_2F_1\left(a, b; c; z\right) \longrightarrow \sum_{i=0}^{\lambda} \frac{(a)_{(i)}(b)_{(i)}}{(c)_{(i)}}\ \frac{z^i}{i!}, \tag{6.57}$$

since for all non-vanishing terms in equation (6.54) both a and b are non-positive integers.[52] The expression therefore depends solely on elementary functions. Equation (6.54) generalises Schnaidt's formula from 1934[38] for any initial state with quantum numbers $\{n,\ n_{i_1},\ n_{i_2}\}$. It is, however, only one-dimensional in reciprocal space and restricted to wave functions in parabolic coordinate space. In order to be fully applicable, extensions to real-valued atomic orbitals and all three dimensions of the reciprocal space are necessary. These extensions are discussed in the following.

To begin with, equation (6.54) can be used to obtain scattering matrix elements of real-valued atomic orbitals if the orbitals are expanded in the basis of eigenstates in parabolic coordinate space:

$$\text{for } m = 0: \qquad \left|\varphi_{n,l,0}\right\rangle = \sum_{n_1=0}^{n-1} a_{n,l,0,n_1}\ \left|\varphi_{n,n_1,n_2}\right\rangle, \tag{6.58}$$

$$\text{for } m > 0: \qquad \left|\varphi^{\mu}_{n,l,m}\right\rangle = \sum_{n_1=0}^{n-m-1} \sum_{\varrho} a^{\mu,\varrho}_{n,l,m,n_1}\ \left|\psi^{\varrho}_{n,n_1,n_2}\right\rangle. \tag{6.59}$$

The states on the left-hand sides of equations (6.58) and (6.59) are the real-valued atomic orbitals defined by their principal, angular momentum,

and magnetic quantum numbers n, l, and m, respectively. Since atomic orbitals can be written as linear combinations of two eigenstates in spherical coordinate space with positive and negative m, only positive values of m are defined here and for each value of $m > 0$ two degenerate orbitals exist. To distinguish between them, the index μ is introduced. It can be either $-$ or $+$, indicating whether the two eigenstates in spherical coordinate space are subtracted from or added to each other. The $2p_x$ and $2p_y$ orbitals, for example, are distinguished by $\mu = -$ and $\mu = +$, respectively. The states in parabolic coordinate space are degenerate in m as well and equation (6.59) thus contains two vectors that are defined by the same set of parabolic quantum numbers $\{n,\, n_1,\, n_2\}$ but carry a different superscript ϱ. Here, ϱ refers to the sign of the exponent $\pm\imath m\phi$ in equation (6.8), meaning that the two vectors on the right-hand side of equation (6.59) are complex conjugate to each other. The second parabolic coordinate is $n_2 = n - n_1 - m - 1$.

Furthermore, equations (6.58) and (6.59) contain complex-valued expansion coefficients. A coefficient can be determined by projection of an atomic orbital onto the eigenstate in parabolic coordinate space it refers to:

$$a^{\mu,\varrho}_{n,l,m,n_1} = \left\langle \varphi^{\varrho}_{n,n_1,n_2} \;\middle|\; \varphi^{\mu}_{n,l,m} \right\rangle, \tag{6.60}$$

where both μ and ϱ disappear if $m = 0$. The expansion coefficients of all 30 real-valued atomic orbitals with principal quantum numbers $n \in \{1, 2, 3, 4\}$ obtained by means of equations (6.60) are shown in Tables **A.1** and **A.2** of the Appendix. By substitution of the appropriate linear combinations for atomic orbitals, equation (6.54) can be applied to the corresponding scattering matrix elements.

As a consequence of the definition of $\hat{L}_z$, equation (6.54) is still restricted to the q_z-component of the reciprocal space. An extension to all three dimensions including q_x and q_y can be achieved by rotation of the scattering vector around the spatially fixed atom. The constraint that $\boldsymbol{q}$ is aligned with the z-axis imposed in equation (6.10) is thereby lifted. Such an operation is mathematically equivalent to a rotation of the atomic orbitals around the spatially fixed scattering vector and is described as the action of the rotation matrices $\hat{\boldsymbol{R}}_y(\theta)$ and $\hat{\boldsymbol{R}}_z(\phi)$ upon the wave function:

$$\left|\tilde{\varphi}\big(\theta,\phi\big)\right\rangle = \hat{\boldsymbol{R}}_z(\phi)\; \hat{\boldsymbol{R}}_y(\theta)\; \left|\varphi\right\rangle. \tag{6.61}$$

The full three-dimensional scattering matrix element is then given as:

$$\left\langle \varphi_f \;\middle|\; \hat{L} \;\middle|\; \varphi_i \right\rangle = \left\langle \tilde{\varphi}_f\big(\theta,\phi\big) \;\middle|\; \hat{L}_z \;\middle|\; \tilde{\varphi}_i\big(\theta,\phi\big) \right\rangle. \tag{6.62}$$

If the vector $\left|\tilde{\varphi}(\theta,\phi)\right\rangle$ on the right-hand side of equation (6.61) is a rotated real-valued atomic orbital, it can be written as an angle-dependent linear combination of unrotated atomic orbitals that share the same principal and angular quantum numbers n and l but differ in their magnetic quantum number $m_{\boldsymbol{R}}$ and index $\mu_{\boldsymbol{R}}$:

$$\begin{aligned}\left|\tilde{\varphi}^{\mu}_{n,l,m}(\theta,\phi)\right\rangle = b^{\mu}_{n,l,m,0}(\theta,\phi)\ \left|\varphi_{n,l,0}\right\rangle \\ + \sum_{m_{\boldsymbol{R}}=1}^{l}\sum_{\mu_{\boldsymbol{R}}} b^{\mu,\mu_{\boldsymbol{R}}}_{n,l,m,m_{\boldsymbol{R}}}(\theta,\phi)\ \left|\varphi^{\mu}_{n,l,m_{\boldsymbol{R}}}\right\rangle.\end{aligned} \tag{6.63}$$

This is related to the fact that m and μ define the orientation of the orbital's angular momentum. The expansion coefficients in equation (6.63) can be determined with the rotation matrices as implied by equation (6.61). The procedure is illustrated for an orbital with angular and magnetic quantum numbers of $l = 2$ and $m = 0$ written as $\left|nd_{z^2}\right\rangle$ in the following:

$$\left|n\tilde{d}_{z^2}(\theta,\phi)\right\rangle = \hat{\boldsymbol{R}}_z(\phi)\ \hat{\boldsymbol{R}}_y(\theta)\ \left|nd_{z^2}\right\rangle. \tag{6.64}$$

First, the rotation matrix $\hat{\boldsymbol{R}}_y(\theta)$ in equation (6.64) acts upon the orbital and thereby transforms the z-coordinate as $z \longrightarrow \sin\theta\ x + \cos\theta\ z$:

$$\begin{aligned}\hat{\boldsymbol{R}}_y(\theta)\ \left|nd_{z^2}\right\rangle &= \left(\sin\theta\ \left|n\bar{d}_x\right\rangle + \cos\theta\ \left|n\bar{d}_z\right\rangle\right)^2 \\ &= \Big(\sin^2\theta\ \left|n\bar{d}_{x^2}\right\rangle + \sin 2\theta\ \left|n\bar{d}_{xz}\right\rangle \\ &\quad + \cos^2\theta\ \left|n\bar{d}_{z^2}\right\rangle\Big].\end{aligned} \tag{6.65}$$

The bar on top of the orbitals in equation (6.65) implies that the states have to be multiplied with an additional factor so that the normalisation is conserved. An insertion of equation (6.65) into equation (6.64) yields:

$$\begin{aligned}\left|n\tilde{d}_{z^2}(\theta,\phi)\right\rangle = \hat{\boldsymbol{R}}_z(\phi)\ \Big[\sin^2\theta\ \left|n\bar{d}_{x^2}\right\rangle + \sin 2\theta\ \left|n\bar{d}_{xz}\right\rangle \\ + \cos^2\theta\ \left|n\bar{d}_{z^2}\right\rangle\Big].\end{aligned} \tag{6.66}$$

Now, the operator $\hat{\boldsymbol{R}}_z(\phi)$ acts upon the vectors in equation (6.66) and thereby transforms the x-coordinate as $x \longrightarrow \cos\phi\ x + \sin\phi\ y$:

$$\begin{aligned}\hat{\boldsymbol{R}}_z(\phi)\ \left|n\bar{d}_{x^2}\right\rangle &= \Big[\cos^2\phi\ \left|n\bar{d}_{x^2}\right\rangle + \sin 2\phi\ \left|n\bar{d}_{xy}\right\rangle \\ &\quad + \sin^2\phi\ \left|n\bar{d}_{y^2}\right\rangle\Big],\end{aligned} \tag{6.67}$$

$$\hat{\boldsymbol{R}}_z(\phi)\ \left|n\bar{d}_{xz}\right\rangle = \Big[\cos\phi\ \left|n\bar{d}_{xz}\right\rangle + \sin\phi\ \left|n\bar{d}_{yz}\right\rangle\Big], \tag{6.68}$$

$$\hat{\boldsymbol{R}}_z(\phi)\ \left|n\bar{d}_{z^2}\right\rangle = \left|n\bar{d}_{z^2}\right\rangle. \tag{6.69}$$

By insertion of equations (6.67) to (6.69) into equation (6.66), the rotated orbital becomes:

$$\begin{aligned}\left|n\tilde{d}_{z^2}(\theta,\phi)\right\rangle &= \sin^2\theta\cdot\Big[\cos^2\phi\ \left|n\bar{d}_{x^2}\right\rangle + \sin 2\phi\ \left|n\bar{d}_{xy}\right\rangle \\ &\quad + \sin^2\phi\ \left|n\bar{d}_{y^2}\right\rangle\Big] \\ &\quad + \sin 2\theta\cdot\Big[\cos\phi\ \left|n\bar{d}_{xz}\right\rangle + \sin\phi\ \left|n\bar{d}_{yz}\right\rangle\Big] \\ &\quad + \cos^2\theta\ \left|n\bar{d}_{z^2}\right\rangle.\end{aligned} \tag{6.70}$$

The states on the right-hand side of equation (6.70) can be replaced with proper linear combinations of common d orbitals shown in Table **B.1** of the Appendix now. These linear combinations are determined by projection of the states onto the orbitals similar to the approach shown in equation (6.60). Finally, a rearrangement and simplification of terms in equation (6.70) yields the expansion coefficients shown in Table **B.2**. All other rotations of atomic orbitals provided in Tables **B.2** to **B.6** have been derived in the same way.

Combining the rotation and expansion of atomic orbitals as described by equations (6.61), (6.63), (6.58), and (6.59) permits an evaluation of three-dimensional scattering matrix elements in terms of equation (6.54). The total number of non-vanishing matrix elements that may result from these expansions is effectively reduced by the selection rule $\Delta m = 0$ derived in equation (6.12). Eigenstates in parabolic coordinate space with unequal magnetic quantum numbers $m_f \neq m_i$ are not coupled *via* equation (6.54). It also follows from equation (6.12) that matrix elements with $\varrho_f \neq \varrho_i$ vanish:

$$\left\langle\varphi_f^+\right|\ \hat{L}_z\ \left|\varphi_i^-\right\rangle = \left\langle\varphi_f^-\right|\ \hat{L}_z\ \left|\varphi_i^+\right\rangle = 0, \tag{6.71}$$

since the integrand in equation (6.12) would become $\exp\big[\pm\iota(m_i+m_f)\phi\big]$ then. With m_f and m_i being positive integers, the integral has to vanish:

$$\int_0^{2\pi} e^{\pm\iota(m_i+m_f)\phi}\,d\phi = 0. \tag{6.72}$$

It is also worth noting that the sign $\varrho = \varrho_f = \varrho_i$ itself does not affect the matrix elements in equation (6.54):

$$\left\langle \varphi_f^+ \,\middle|\, \hat{L}_z \,\middle|\, \varphi_i^+ \right\rangle = \left\langle \varphi_f^- \,\middle|\, \hat{L}_z \,\middle|\, \varphi_i^- \right\rangle . \tag{6.73}$$

Hence, only one of the two scattering matrix elements in equation (6.73) has to be evaluated and the number of required calculations is reduced by another factor of 2.

If equation (6.54) is directly applied to the differential scattering signal in equation (2.12), only states that are occupied by the electronic wave packet have to be rotated and expanded. The sum over the final states includes all degenerate eigenstates of a given principal quantum number and is therefore rotationally invariant. Whether these states are described as real-valued atomic orbitals or as wave functions in parabolic coordinate space, is both physically and mathematically irrelevant. In any case, each degenerate state occurs exactly once.

Despite all these restrictions, it may appear at first that an evaluation of the scattering matrix elements in parabolic coordinate space is mathematically more involved and more laborious than a simple numerical evaluation of equation (6.5). However, no numerical or iterative procedure is involved and the computational cost is reduced significantly. The scattering matrix elements are completely described by elementary functions and the results are therefore mathematically exact.

Part III

Simulations of Time-Resolved X-Ray Scattering

7 The Hydrogen Atom

In this section a simulation of the differential scattering signal $dS/d\Omega$ of an electronic wave packet of superposed $\left|3d_{z^2}\right\rangle$ and $\left|4f_{z^3}\right\rangle$ orbitals of the hydrogen atom is presented. The numerical results of Dixit, Vendrell, and Santra[25], who have already published scattering patterns of this wave packet, are reproduced within the theoretical framework of sections 1 and 2 and by means of the analytic approach derived in section 6. Thereby, the general equivalence of the formalisms of Dixit *et al.* and of Henriksen and Møller as well as the applicability of the analytic approach are illustrated. All contributions to the scattering signal are evaluated and analysed in detail. The effect of the pulse duration on the scattering signal is revised and an explanation that deviates from the one of Dixit *et al.* is given.

In subsection 7.1 the general expressions from section 2 are further simplified for the wave packet at hand. This facilitates their evaluation and makes the discussion of the scattering signal more transparent. Subsection 7.2 provides further information about the evaluation of the scattering signal. The performance of the analytic approach from section 6 is discussed. The results are presented in subsection 7.3. All scattering intensities are given in electronic units, *i.e.* in units of the Thomson scattering cross-section of the free electron $d\sigma_{\mathrm{T}}/d\Omega$.

7.1 Simplification of Expressions

Following equation (2.1), the electronic wave packet of superposed $\left|3d_{z^2}\right\rangle$ and $\left|4f_{z^3}\right\rangle$ orbitals of the hydrogen atom is:

$$\left|\Psi(t)\right\rangle = \frac{1}{\sqrt{2}} \cdot \left(e^{-\frac{\iota}{\hbar}E_3 t} \left|3d_{z^2}\right\rangle + e^{-\frac{\iota}{\hbar}E_4 t} \left|4f_{z^3}\right\rangle \right). \tag{7.1}$$

Both states in equation (7.1) contribute equally with a weight of $1/\sqrt{2}$. The expansion coefficients of the wave-packet are thus assumed to be time-independent. The eigenenergies of the two atomic orbitals E_3 and E_4 are $E_3 = -1/18$ a.u. ≈ -1.51 eV and $E_4 = -1/32$ a.u. ≈ -0.85 eV.

By insertion of the wave packet from equation (7.1) into equations (2.19), (2.20), and (2.18), the elastic plus inelastic and the coherence contributions to the scattering signal are:

$$\begin{aligned} \frac{dS_\mathrm{e}}{d\Omega} + \frac{dS_\mathrm{i}}{d\Omega} = \frac{1}{2} \frac{d\sigma_\mathrm{T}}{d\Omega} N_\mathrm{p} \cdot \sum_f^\infty \Big(& W_{f,3}(\Delta\omega) \left|L_{f,3}(\boldsymbol{q}_0)\right|^2 \\ & + W_{f,4}(\Delta\omega) \left|L_{f,4}(\boldsymbol{q}_0)\right|^2 \Big), \end{aligned} \tag{7.2}$$

$$\begin{aligned} \frac{dS_\mathrm{c}}{d\Omega} = & \frac{d\sigma_\mathrm{T}}{d\Omega} \cdot \sum_f^\infty W_{f,3,4}(\Delta\omega) \\ & \times \int_{-\infty}^{+\infty} I(t-\tau) \, \mathrm{Re}\Big[L_{f,3}(\boldsymbol{q}_0) \, L^*_{f,4}(\boldsymbol{q}_0) \, e^{\iota\omega t} \Big] \, dt. \end{aligned} \tag{7.3}$$

The numbers 3 and 4 in the subscripts of the scattering matrix elements and weights in equations (7.2) and (7.3) refer to the two orbitals of the wave packet. The angular frequency $\omega = \big(E_4 - E_3\big)/\hbar$ in the coherence contribution is $\omega = 7/288$ a.u. ≈ 1.00 fs, meaning that the signal oscillates with a period of $T = 576\pi/7$ a.u. ≈ 6.25 fs.

Considering that the $\left|3d_{z^2}\right\rangle$ orbital is *gerade*, whereas the $\left|4f_{z^3}\right\rangle$ orbital is *ungerade*, and following the discussion around equations (5.2) to (5.4), the real-part of the product $L_{f,3}(\boldsymbol{q}_0) \, L^*_{f,4}(\boldsymbol{q}_0)$ in equation (7.3) is zero. Hence, only a multiplication with the imaginary-part of the exponential $\exp\big(\iota\omega t\big) = \cos\omega t + \iota \sin\omega t$ leads to real-valued and non-vanishing terms:

$$\begin{aligned} \frac{dS_\mathrm{c}}{d\Omega} = & \frac{d\sigma_\mathrm{T}}{d\Omega} \cdot \int_{-\infty}^{+\infty} I(t-\tau) \, \sin\omega t \, dt \\ & \times \iota \cdot \sum_f^\infty W_{f,3,4}(\Delta\omega) \, L_{f,3}(\boldsymbol{q}_0) \, L^*_{f,4}(\boldsymbol{q}_0). \end{aligned} \tag{7.4}$$

Furthermore, the incident X-ray pulse is assumed to be transform limited. In accordance with equations (1.48) and (1.49), the photon number intensity $I(t)$ is described by a normalised Gaussian:

$$I(t-\tau) = \frac{1}{\sqrt{2\pi}\sigma}\ e^{-\frac{(t-\tau)^2}{2\sigma^2}}, \tag{7.5}$$

where τ and σ are the pump-probe delay and the standard deviation of the photon number distribution of the pulse. The latter is related to the pulse duration d_p (FWHM) by $\sigma = d_\mathrm{p}/\big(2\sqrt{2\ln 2}\big)$. With equation (7.5), the integrated photon number intensity $N_\mathrm{p} = \int_{-\infty}^{+\infty} I(t-\tau)\ dt$ in equation (7.2) is unity and the integral over time in equation (7.4) is analytically solved:

$$\int_{-\infty}^{+\infty} I(t-\tau)\ \sin\omega t\ dt = e^{-\frac{1}{2}\sigma^2\omega^2}\ \sin\omega\tau. \tag{7.6}$$

Following equations (1.48) and (1.50), the coherence function $C(\delta)$ of the incident X-ray pulse is:

$$C(\delta) = e^{-\frac{\delta^2}{8\sigma^2}}. \tag{7.7}$$

With equations (7.7) and (2.10), the spectral density of the pulse becomes:

$$F\big(\omega_{\boldsymbol{k}_\mathrm{s}} - \omega_{\boldsymbol{k}_0} + \omega_{fij}\big) = \sqrt{\frac{2}{\pi}}\ \sigma\ e^{-2\sigma^2\left(\omega_{\boldsymbol{k}_\mathrm{s}} - \omega_{\boldsymbol{k}_0} + \omega_{fij}\right)^2}. \tag{7.8}$$

Analogous to the distribution of incident field modes c_k in equation (1.16), the spectral density in equation (7.8) describes the deviation of angular frequencies $\omega_{\boldsymbol{k}_\mathrm{s}}$ from $\omega_{\boldsymbol{k}_0}$ around ω_{fij}. It refers to the number of incident photons whose energies are shifted to $\hbar\omega_{\boldsymbol{k}_\mathrm{s}}$ as a consequence of an energy transfer $\hbar\omega_{fij}$. With the spectral density in equation (7.8), the detection window $W_{fij}(\Delta\omega)$ from equation (2.13) is:

$$\begin{aligned} W_{fij}(\Delta\omega) = \frac{1}{2}\cdot\Bigg[&\mathrm{erf}\Big(\sqrt{2}\sigma\big(\omega_{fij} + \Delta\omega\big)\Big) \\ &- \mathrm{erf}\Big(\sqrt{2}\sigma\big(\omega_{fij} - \Delta\omega\big)\Big)\Bigg]. \end{aligned} \tag{7.9}$$

The window function $W_{fij}(\Delta\omega)$ in equation (7.9) accounts for the number of scattered photons with angular frequencies $\omega_{\boldsymbol{k}_\mathrm{s}}$ within the detection range of $\pm\Delta\omega$ around $\omega_{\boldsymbol{k}_0}$ and takes values between 0 and 1.

By insertion of $N_\mathrm{p} = 1$ and equation (7.6), equations (7.2) and (7.4) become:

$$\frac{dS_\mathrm{e}}{d\Omega} + \frac{dS_\mathrm{i}}{d\Omega} = \frac{d\sigma_\mathrm{T}}{d\Omega}\ \mathcal{A}(\Delta\omega, \boldsymbol{q}_0), \tag{7.10}$$

$$\frac{dS_\mathrm{c}}{d\Omega} = \frac{d\sigma_\mathrm{T}}{d\Omega}\ e^{-\frac{1}{2}\sigma^2\omega^2}\ \sin\omega\tau\ \mathcal{M}(\Delta\omega, \boldsymbol{q}_0), \tag{7.11}$$

where the sums of scattering matrix elements are abbreviated as:

$$\begin{aligned}\mathcal{A}(\Delta\omega, \boldsymbol{q}_0) = \frac{1}{2}\cdot\sum_f^\infty\ \Big(&W_{f,3}(\Delta\omega)\ \left|L_{f,3}(\boldsymbol{q}_0)\right|^2 \\ &+ W_{f,4}(\Delta\omega)\ \left|L_{f,4}(\boldsymbol{q}_0)\right|^2\Big),\end{aligned} \tag{7.12}$$

$$\mathcal{M}(\Delta\omega, \boldsymbol{q}_0) = \iota\cdot\sum_f^\infty\ W_{f,3,4}(\Delta\omega)\ L_{f,3}(\boldsymbol{q}_0)\ L^*_{f,4}(\boldsymbol{q}_0). \tag{7.13}$$

As discussed in section 2, the elastic and inelastic contributions to the differential scattering signal in equation (7.10) do not change with time. They define the static average of the signal. Solely the coherence part in equation (7.11) depends on the pump-probe delay τ and describes the time-dependent modulation of the signal. According to equation (7.11), the scattering signal displays a simple sinusoidal oscillation with a period of $T \approx 6.25$ fs.

The exponential in equation (7.11) accounts for the finite duration of the incident pulse. It takes values between 0 and 1 and decreases rapidly with an increase in the ratio of the pulse duration and the period d_p/T. For a pulse duration of $d_\mathrm{p} = 1.00$ fs, for example, 91% of the time-dependent modulation can be resolved. In the theoretical framework of Dixit *et al.* it was essentially implied that the exponential is unity, since the authors have assumed that the "pulse duration should be sufficiently short to freeze the dynamics of the electronic wave packet".[25] In the framework at hand, however, the integral over time is solved analytically and there is no apparent reason to make such an assumption. In fact, a strict discussion of the effect of the pulse duration requires that not only the weights $W_{fij}(\Delta\omega)$ but also the exponential in equation (7.11) can change with d_p.

7.2 Computational Methods

Following Dixit *et al.*, a mean photon energy of $\hbar\omega_{\boldsymbol{k}_0} = 4$ keV, a detection range of $\hbar\Delta\omega = \pm 0.25$ eV around $\hbar\omega_{\boldsymbol{k}_0}$, and a pulse duration of $d_\mathrm{p} = 1.00$ fs was chosen. The sums over final states in equations (7.12) and (7.13) were truncated at principal quantum numbers of $n_f = 50$. This means that 42 925 states were included. The scattering matrix elements were evaluated with the analytical approach discussed in section 6. First, the coordinate system was defined as in section 4. The incident X-ray pulse was assumed to propagate in z-direction and the electronic wave packet was oriented orthogonally along the x-axis. Hence, the $\left|3d_{z^2}\right\rangle$ and $\left|4f_{z^3}\right\rangle$ orbitals were transformed to $\left|3d_{x^2}\right\rangle$ and $\left|4f_{x^3}\right\rangle$ orbitals as shown in Table **B.1** of the Appendix. Second, the orbitals were rotated with the coefficients provided in Tables **B.2** to **B.6** and the scattering operator was reduced to $\hat{L}_z$ as in equation (6.10). Third, the rotated vectors were expanded in the basis of eigenstates in parabolic coordinate space according to Tables **A.1** and **A.2**. Fourth, the resulting matrix elements of $\hat{L}_z$ were evaluated by application of equation 6.54. Further details of the procedure are given in reference 56. (Note that the wave packet was oriented along the y-axis there.)

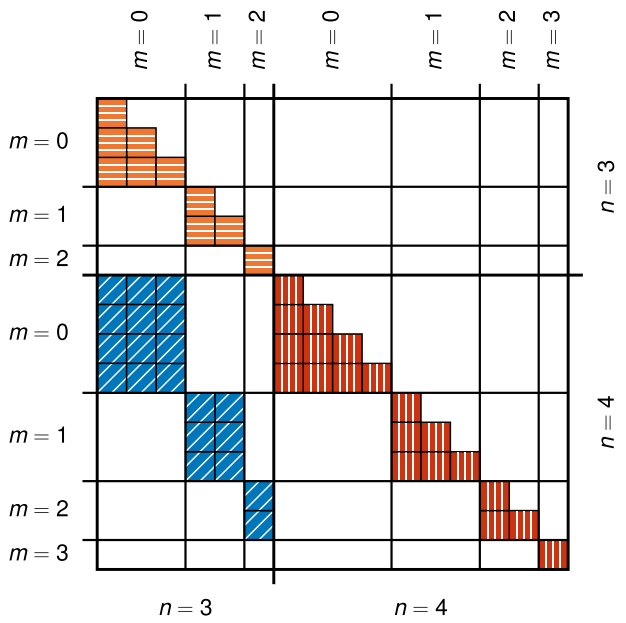

Fig. 7.1: Matrix structure of scattering matrix elements of the operator $\hat{L}_z$ and eigenstates with principal quantum numbers $n \in \{3, 4\}$ in parabolic coordinate space. The coloured squares represent matrix elements that have to be evaluated by application of equation (6.54). The blank parts are either redundant or vanish. The matrix is partitioned into blocks of elements that share the same principal and magnetic quantum numbers m and n.

In order to assess the computational performance and requirements of this approach, the total number of scattering matrix elements that needed to be evaluated by means of equation (6.54) was calculated. For a given pair of principal and magnetic quantum numbers n and m, there are $n-m$ different eigenstates in parabolic coordinate space that lead to distinguishable matrix elements of $\hat{L}_z$. This follows from the relation $n = n_1 + n_2 + m + 1$. The parabolic quantum number n_1 is restricted to values between 0 and $n - m - 1$. Moreover, the degenerate states with $m > 0$ do not add matrix elements that differ from those of their complex conjugate counterparts, as discussed around equations (6.71) and (6.72). Due to the selection rule $\Delta m = 0$ implied by equation (6.12), only states with the same magnetic quantum number are coupled. Finally, the matrix elements are invariant under interchange of their initial and final states, since a change in sign of the complex-valued exponents in equation (6.8) does not alter equation (6.12). The resulting matrix of distinguishable scattering matrix elements for states with $n \in \{3, 4\}$ is illustrated in Figure **7.1**. The coloured squares represent matrix elements that differ from each other, whereas the blank parts are either redundant or vanish. Out of 256 matrix elements only 50 had to be evaluated. The total number of scattering matrix elements involved in the calculation is obtained by adding the number of matrix elements arising from the remaining final states with $n_f \notin \{3, 4\}$ to the 50 matrix elements from Figure **7.1**. This number is given as:

$$\sum_{n_i} \sum_{n_f \notin \{n_i\}}^{n_{f,\max}} \sum_{m=0}^{m_{\max}} \big(n_i - m\big) \cdot \big(n_f - m\big), \tag{7.14}$$

where the upper limit of the sum over m is $m_{\max} = \min(n_i, n_f) - 1$. With the choice of $n_{f,\max} = 50$, a total of 19 672 distinguishable scattering matrix elements had to be evaluated with equation (6.54).

This number was compared to the amount of radial integrals the equivalent calculation in terms of equation (6.5) would have implied. In contrast to the 16 states that lead to the 50 matrix element in Figure **7.1**, a direct calculation in spherical coordinate space would involve only two initial states, namely the atomic orbitals $\left|3d_{z^2}\right\rangle$ and $\left|4f_{z^3}\right\rangle$. The sum over the angular momentum quantum number l in equation (6.5) and the absence of selection rules like $\Delta m = 0$, however, give rise to a significant number of radial integrals, even though the basis of the wave packet appears to be smaller by a factor of 8. For a given quartet of angular momentum and magnetic quantum numbers l_f, l_i, m_f, and m_i, there are $l_f + l_i - \max\big(|l_f - l_i|, |m_f - m_i|\big) + 1$ different radial integrals. This follows from the two relations $\left|l_f - l_i\right| \leq l \leq l_f + l_i$ and $m = m_f - m_i$ that the Clebsch-Cordon coefficients in equation (6.5) have to satisfy. The smallest value l can take is either $\left|l_f - l_i\right|$ or $\left|m_f - m_i\right|$, since $|m|$ cannot be larger than l. The largest value of l is simply given by

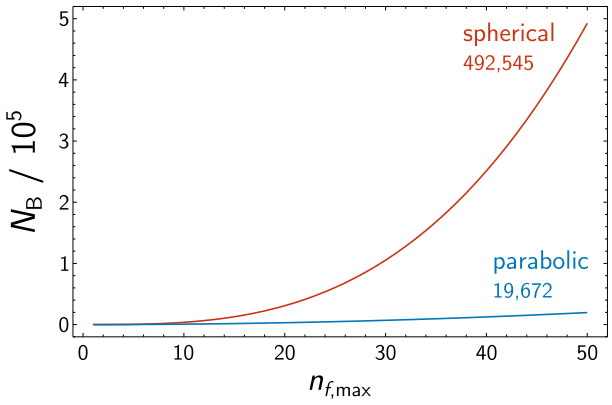

Fig. 7.2: Number of radial integrals in spherical coordinate space and of one-dimensional scattering matrix elements in parabolic coordinate space that a calculation of equations (7.12) and (7.13) in terms of equations (6.5) and (6.54), respectively, would require. The variable $n_{f,\max}$ denotes the principal quantum number at which the sum over final states is truncated.

$l_f + l_i$. The total number of radial integrals is calculated accordingly by summation over the quantum numbers of the final states:

$$\sum_{n_f}^{n_{f,\max}} \sum_{l_f=0}^{n_f-1} \sum_{m_f=-l_f}^{l_f} \Big(l_f + l_i - \max\big(|l_f - l_i|, |m_f - m_i|\big) + 1 \Big), \qquad (7.15)$$

for every pair of l_i and m_i. With $n_{f,\max} = 50$ the $|3d_{z^2}\rangle$ and $|4f_{z^3}\rangle$ orbitals give rise to 207 075 and 285 475 radial integrals each. However, the fact that atomic orbitals are real-valued implies that the scattering matrix elements are invariant under interchange of their initial and final states again. The matrix element that involve both the $|3d_{z^2}\rangle$ and $|4f_{z^3}\rangle$ orbitals and that require the evaluation of 5 radial integrals are therefore counted twice. Thus, a calculation in terms of equation (6.5) would imply a total of 492 545 radial integrals. Considering that each of these integrals would be evaluated numerically, whereas the 19 672 scattering matrix elements in parabolic coordinate space were integrated analytically, the application of equation (6.54) allowed a significant reduction of the computational costs.

Figure **7.2** reveals that the number of one-dimensional scattering matrix elements in parabolic coordinate space increased much slower with $n_{f,\max}$ than the number of radial integrals in spherical coordinate space.

7.3 Results

The total (t) differential scattering patterns $dS/d\Omega$ and their coherence (c) contributions are shown in Figure **7.3**. Five representative pump-probe delays τ that cover a full period $T \approx 6.25$ fs of the oscillating electronic wave packet have been chosen. As equations (7.10) and (7.11) have implied, the total scattering signal displays a sinusoidal modulation with τ that stems solely from the changes in the coherence contribution. The total scattering patterns in Figure **7.3** match the ones published by Dixit *et al.*[25] and hence confirm their main results as well as the applicability of the analytical approach derived in section 6.

At $\tau = 0.00$ fs, $\tau = 3.13$ fs, and $\tau = 6.25$ fs, *i.e.* at zero, one half, and one times T, the factor $\sin \omega\tau$ in equation (7.11) is zero and the coherence signal vanishes. The total signal is thus completely described by the elastic plus inelastic contributions at these pump-probe delays. In compliance with Friedel's law[41,50], the three scattering patterns display a dihedral rosette

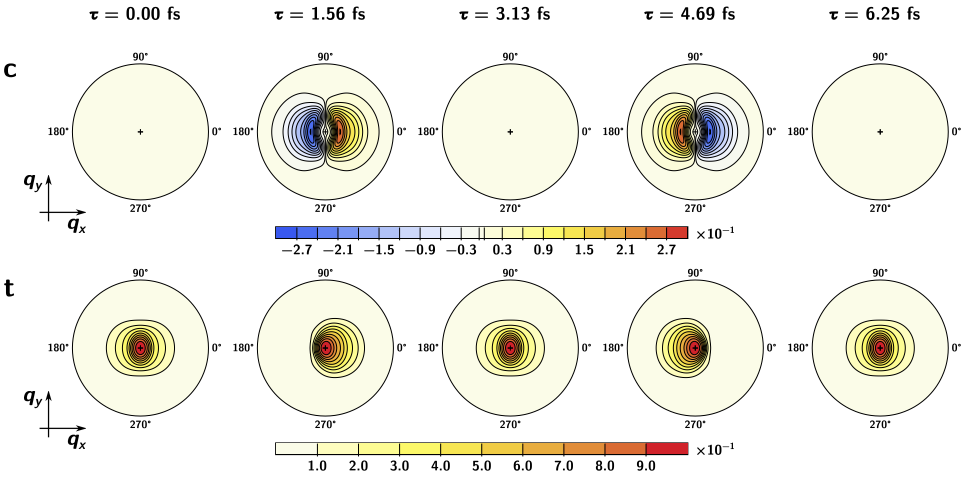

Fig. 7.3: Contour plots of the coherence (**c**) and total (**t**) time-resolved X-ray scattering patterns $dS/d\Omega$ in the q_x-q_y plane at five pump-probe delays τ. The scattering intensity is given in electronic units. The radiation is scattered by a non-stationary electronic wave packet of superposed and equally weighted $\left|3d_{z^2}\right\rangle$ and $\left|4f_{z^3}\right\rangle$ orbitals of the hydrogen atom oriented along the x-axis. The incident probe pulse propagates in z-direction and has a mean photon energy of $\hbar\omega_0 = 4.0$ keV and a time duration (FWHM) of $d_\mathrm{p} = 1.00$ fs. All scattered photons within the range of $\hbar\Delta\omega = \pm 0.25$ eV around $\hbar\omega_0$ are detected. With photons scattered up to 60°, the q_x and q_y coordinates take values between ± 2.03 Å^{-1}. The angular coordinate is the azimuthal angle of the $\boldsymbol{q}$-vector, ϕ_q. The five pump-probe delays τ cover a full period of the oscillation of the electronic wave packet.

group symmetry D_2 that contains a twofold rotation as well as two reflections, one through the q_x- and another one through the q_y-axis. According to equations (5.8) and (5.11), the validity of Friedel's law implies that the one-electron densities and transition densities of the electronic wave packet do not change when reflected through the detector plane in real-space. The two atomic orbitals $\left|3d_{z^2}\right\rangle$ and $\left|4f_{z^3}\right\rangle$ that define the wave packet are indeed invariant under such an operation. That alone is sufficient to conclude that the elastic and inelastic scattering patterns have to be centrosymmetric. Individual final states involved in the sum in equation (7.12) may transform differently, but the inclusion of all degenerate states of a given principal quantum number results in spherical symmetry. Moreover, the scattering patterns have a single maximum of 1 at zero momentum transfer in the origin of the detector. This is required by equation (5.1) and relates to the number of electrons squared.

At $\tau = 1.56$ fs and $\tau = 4.69$ fs, *i.e.* at one fourth and three fourth of the period, the factor $\sin \omega\tau$ in equation (7.11) is equal to unity and minus unity, respectively, and the coherence signal is strongest. In contrast to the elastic and inelastic contributions, the coherence signal is not related to a sum of absolute squares of one-electron scattering matrix elements and does not have to obey Friedel's law. The fact that the two atomic orbitals $\left|3d_{z^2}\right\rangle$ and $\left|4f_{z^3}\right\rangle$ are *gerade* and *ungerade* implies that the coherence signal has to be odd with respect to the q_x-axis. This follows from the discussion around equations (5.2) to (5.4) and becomes apparent in Figure **7.3** where the coherence contribution changes sign when the q_x-coordinate is inverted. The coherence scattering patterns transform according to the less symmetric D_1 rosette group that contains only a onefold rotation and a single reflection through the q_x-axis. They display two extrema with opposite sign, one in the negative and one in the positive range of q_x on the q_y-axis. The extrema take values of roughly ± 0.27 at $q_x = \pm 0.45$ Å^{-1}. The non-vanishing coherence contribution to the total scattering signal breaks the D_2 symmetry of the static average and invalidates Friedel's law. Furthermore, the coherence contribution causes the total scattering signal to oscillate back and forth along the q_x-axes. At $\tau = 1.56$ fs, most of the scattering amplitude appears in the right semicircle of the detector. At $\tau = 4.69$ fs, the majority of X-ray photons is scattered to the left.

The total scattering patterns in Figure **7.3** reflect the oscillating motion of the electron in x-direction, even though they do not directly reveal the corresponding changes in the one-electron density. It has been mentioned before that the time-dependent modulation of the scattering signal originates exclusively from the coherence and not from the elastic contribution. Neither equation (7.10) nor equation (7.11) involve the time-dependent one-electron density $\rho(\boldsymbol{r}, t)$. Instead, the coherence signal in equation (7.11) correlates the scattering amplitudes of different electronic states occupied in the wave

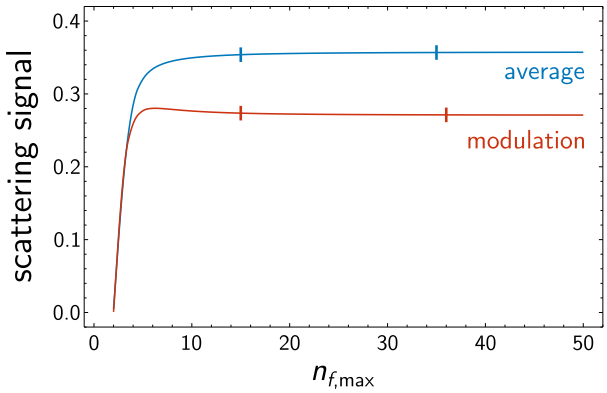

Fig. 7.4: Convergence of the static average and of the amplitude of the time-dependent modulation of the differential scattering signal $dS/d\Omega$. The variable $n_{f,\max}$ denotes the principal quantum number at which the sum over final states is truncated. The scattering intensity is given in electronic units. The incident probe pulse has a mean photon energy of $\hbar\omega_0 = 4.0$ keV and a time duration (FWHM) of $d_\mathrm{p} = 1.00$ fs. All scattered photons within the range of $\hbar\Delta\omega = \pm 0.25$ eV around $\hbar\omega_0$ are detected. The signals have been evaluated at $q \approx 0.45$ Å^{-1}, $\theta_q \approx 84°$, and $\phi_q = 90°$. The vertical lines mark the points at which the signals are converged to less than 1% or 0.1% deviation from their values at $n_{f,\max} = 50$. They are $n_{f,\max} = 15$ and $n_{f,\max} = 35$ (average) as well as $n_{f,\max} = 15$ and $n_{f,\max} = 36$ (modulation).

packet. It is sensitive to the complex-valued, time-dependent phases of the states and therefore changes with the pump-probe delay τ. The coherence signal is a consequence of the quantum nature of both the material system and the X-ray photons and cannot be understood in classical terms. There is no other observable such as the one-electron density $\rho(\boldsymbol{r}, t)$ the coherence scattering signal can be assigned to.

Figure **7.4** illustrates how the truncation of the sum over the final states in equations (7.12) and (7.13) affects the differential scattering signal. Shown are the values of the elastic plus inelastic and of the coherence contributions obtained for different upper limits of the principal quantum number $n_{f,\max}$. The signals have been calculated at the point of the detector where the coherence pattern at $\tau = 1.56$ fs in Figure **7.3** has its maximum. Both contributions are converging with increasing values of $n_{f,\max}$. Final states with principal quantum numbers larger than $n_{f,\max} \approx 20$ lead to insignificant changes of the scattering signals. This is, however, not necessarily true at all coordinates in reciprocal space. The inclusion of every eigenstate up to $n_{f,\max} = 50$ ensures that the differential scattering signal is converged everywhere on the detector.

Dixit *et al.* have also investigated the influence of the pulse duration d_p on the differential scattering signal $dS/d\Omega$.[25] The authors have reported "an optimum contrast as a function of time for a pulse length close to 1 fs" and explained their result with the claim that the scattering signal would become independent of the pump-probe delay for $d_\mathrm{p} \longrightarrow 0$. Crucially, they came to the conclusion that the pulse has to be long enough that the electron has enough "time to change its position". This does not become immediately clear by inspection of equations (7.10) and (7.11), however. There, the pulse duration appears in the exponential term $\exp\big(-\sigma^2\omega^2/2\big)$ and in the window function $W_{fij}(\Delta\omega)$ *via* σ only. The former has been neglected by the authors altogether and the latter does not refer to the "characteristic time scale of the wave packet" but to the photon energies accepted by the detector. Their explanation also seems to contradict their assumption that the "pulse duration should be sufficiently short to freeze the dynamics of the electronic wave packet", which implies that the electron would never have enough time to change its position during the pulse. If their explanation of the optimum contrast would be true, their simulations should not show any time-dependence at all. The influence of the pulse duration on the differential scattering signal $dS/d\Omega$ is therefore discussed once more in the following.

Figure **7.5 A** shows the total differential scattering signal at pump-probe delays from $\tau = 0.00$ fs to $\tau = 6.25$ fs for the three different pulse durations $d_\mathrm{p} = 4$ fs, $d_\mathrm{p} = 1$ fs, and $d_\mathrm{p} = 100$ as. As in Figure **7.4**, the signals have been calculated at the point of the detector where the coherence pattern at $\tau = 1.56$ fs has its maximum. The same detection range $\hbar\Delta\omega$ has been applied to all three pulses. Figure **7.5 A** reveals that the static average of the signal decreases from 0.56 at $d_\mathrm{p} = 4$ fs to 0.36 at $d_\mathrm{p} = 1$ fs and further to $5.8 \cdot 10^{-2}$ at $d_\mathrm{p} = 100$ as. This decrease is a simple consequence of the restriction on the range of photon energies that are accepted by the detector. A shorter pulse duration d_p leads to a broader spectral density in equation (7.8). Hence, the number of photons that fall into the detection range $\hbar\omega_{\boldsymbol{k}_0} \pm \hbar\Delta\omega$ and consequently the weights $W_{fij}(\Delta\omega)$ in equation (7.9) decrease. The amplitude of the time-dependent modulation of the signal, however, does not show the same behaviour as the static average. It is largest clearly at $d_\mathrm{p} = 1$ fs. This becomes even more apparent in Figure **7.5 B** where only the modulation is shown. The amplitude increases from $8.8 \cdot 10^{-2}$ at $d_\mathrm{p} = 4$ fs to 0.25 at $d_\mathrm{p} = 1$ fs and then decreases to $3.4 \cdot 10^{-2}$ at $d_\mathrm{p} = 100$ as. This implies that there is indeed an optimum around $d_\mathrm{p} = 1$ fs as Dixit *et al.* have reported.

Figure **7.6 A** displays the average and the amplitude of the modulation as continuous functions of the pulse duration d_p. The average decreases monotonically with d_p and approaches zero for $d_\mathrm{p} \longrightarrow 0$. The amplitude of the modulation has an optimum of 0.29 at $d_\mathrm{p} = 1.63$ **fs** and approaches zero

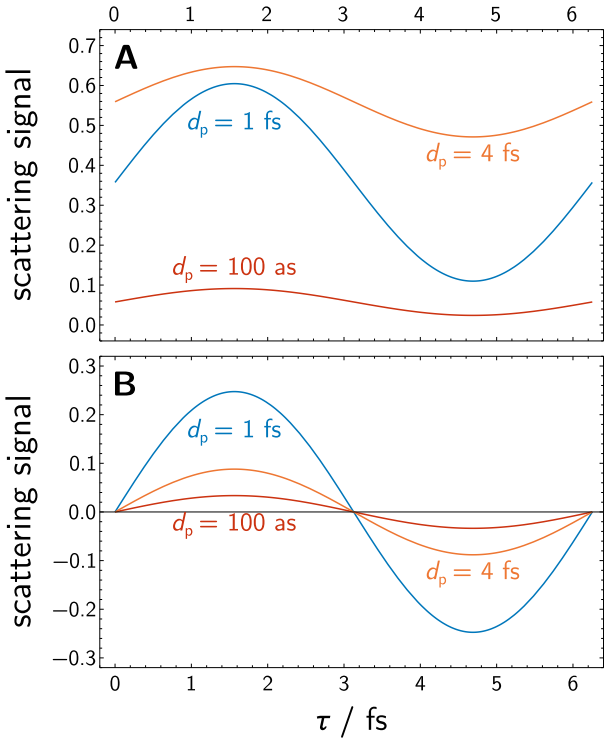

Fig. 7.5: (**A**) Total differential scattering signal $dS/d\Omega$ at different pump-probe delays τ. (**B**) Time-dependent modulation of the differential scattering signal $dS/d\Omega$ at different pump-probe delays τ. The modulation is given by the coherence contribution. (**A** and **B**) Signals for probe pulse durations of $d_\mathrm{p} = 4$ fs, $d_\mathrm{p} = 1$ fs, and $d_\mathrm{p} = 100$ as are shown. The scattering intensity is given in electronic units. The signals have been evaluated at $q \approx 0.45$ Å^{-1}, $\theta_q \approx 84°$, and $\phi_q = 90°$ with a detection range of $\hbar\Delta\omega = \pm 0.25$ eV around the mean photon energy $\hbar\omega_{\boldsymbol{k}_0} = 4$ keV.

for $d_\mathrm{p} \longrightarrow 0$ as well. Figure **7.6 A** also shows the ratio of the two signals in *per cent*, termed the relative amplitude of the modulation. It is a measure of the relative strength of the time-dependent signal. The relative amplitude has a maximum of 71.2% at $d_\mathrm{p} = 1.31$ **fs** and approaches a constant of 58.2% with $d_\mathrm{p} \longrightarrow 0$. Hence, the claim of Dixit *et al.* that the signal would become independent of the pump-probe delay for $d_\mathrm{p} \longrightarrow 0$ cannot be corroborated. Even though the signal will eventually become too weak to be detected, it does not lose its time-dependence.

Moreover, the elastic and inelastic contributions to the static average are shown in Figure **7.6 B**. The elastic signal decreases monotonically with the pump-probe delay, whereas the inelastic signal has an optimum of 0.20 at $d_\mathrm{p} = 0.99$ **fs**. Clearly, the appearance of the optimum in the inelastic signal cannot be explained with the characteristic time scale of the wave packet,

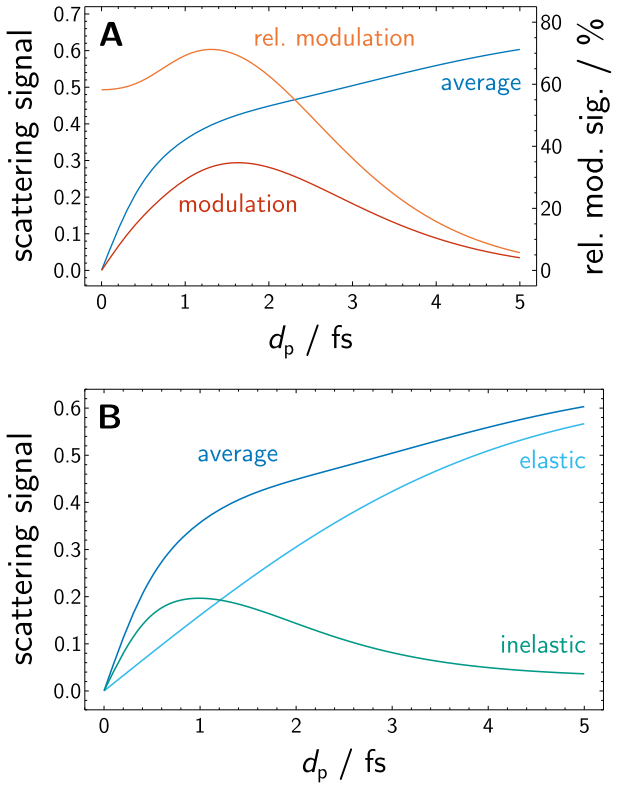

Fig. 7.6: (**A**) Static average, amplitude of the modulation, and relative amplitude of the modulation of the differential scattering signal $dS/d\Omega$ at different probe pulse durations d_p. (**B**) Elastic and inelastic contributions to the static average of the differential scattering signal $dS/d\Omega$ at different probe pulse durations d_p. (**A** and **B**) The scattering intensity is given in electronic units. The signals have been evaluated at $q \approx 0.45$ Å^{-1}, $\theta_q \approx 84°$, and $\phi_q = 90°$ with a detection range of $\hbar\Delta\omega = \pm 0.25$ eV around the mean photon energy $\hbar\omega_{\boldsymbol{k}_0} = 4$ keV.

since equation (7.10) is independent of time. It can only be ascribed to the weights $W_{fij}(\Delta\omega)$ from equation (7.9) and therefore has to be a consequence of the restriction on the range of photon energies that are accepted by the detector as well. At the optimum, the largest fraction of photons falls into the detection range $\hbar\omega_{\boldsymbol{k}_0} \pm \hbar\Delta\omega$ after they have gained or lost an energy of $\hbar\omega_{fij}$. At shorter pulse durations, the spectral density is broader and fewer photons are shifted into the detection range. Similarly, the spectral density is narrower at longer pulse durations and more photons are scattered to energies outside of $\hbar\omega_{\boldsymbol{k}_0} \pm \hbar\Delta\omega$.

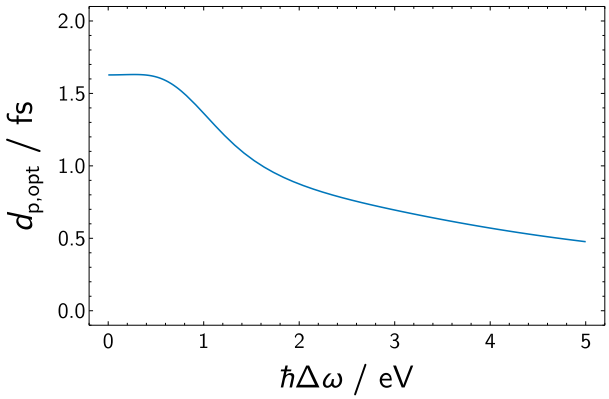

Fig. 7.7: Pulse duration $d_{\mathrm{p,opt}}$ at which the amplitude of the time-dependent modulation has its optimum for different detection ranges $\pm\hbar\Delta\omega$ around the mean photon energy $\hbar\omega_{\boldsymbol{k}_0} = 4$ keV.

The same applies to the optimum of the amplitude of the time-dependent modulation. Consequently, the pulse duration at which the optimum occurs has to be dependent on $\hbar\Delta\omega$, as shown in Figure **7.7**. The optimum appears at shorter pulse durations when a larger detection range is chosen. For $\hbar\Delta\omega = 5$ eV, the amplitude of the modulation has its optimum at a pulse duration that is an order of magnitude shorter than the period of the wave packet. This demonstrates that the "optimum contrast" Dixit *et al.* have reported is not related to the "characteristic time scale of the wave packet". It is entirely due to the restriction on the range of photon energies that are accepted by the detector. It is therefore not necessary that the electron has enough "time to change its position" during the pulse to observe a time-dependent signal.

8 The Hydrogen Molecule

In this section a simulation of the differential scattering signal $dS/d\Omega$ of the hydrogen molecule subsequent to UV excitation is presented. The molecule is excited from it $X^1\Sigma_g^+$ ground state to its $B^1\Sigma_u^+$ excited state. All contributions to the scattering signal are evaluated and analysed in detail. Two-dimensional scattering patterns are displayed and the separability of the coherence contribution from the elastic and inelastic signal is discussed.

Subsection 8.1 provides information about the computational methods that were used in the simulations. The results are presented in subsection 8.2. All scattering intensities are given in electronic units, *i.e.* in units of the Thomson scattering cross-section of the free electron $d\sigma_{\mathrm{T}}/d\Omega$.

8.1 Computational Methods

Electronic Structure Calculation

The first nine electronic singlet states of the H_2 molecule—$X^1\Sigma_g^+$, $B^1\Sigma_u^+$, $EF^1\Sigma_g^+$, $C^1\Pi_u$, $GK^1\Sigma_g^+$, $B'^1\Sigma_u^+$, and $I^1\Pi_g$—were calculated with state-average CASSCF(2,30)[57,58]/d-aug-cc-pVQZ[59,60] implemented in the MOLPRO quantum chemistry package[61,62]. D_{2h} point-group symmetry was applied, allowing for the separation of the close-to-degenerate Σ and Π states as well as for the separation of the degenerate Π states into different irreducible representations. The active space was constructed by inclusion of the 30 lowest molecular orbitals that transformed as the relevant irreducible representations: 7 orbitals in A_g and B_{1u} and 4 orbitals in B_{2g}, B_{3g}, B_{2u}, and B_{3u} each. The energies of the states were computed for H–H bond lengths R between $R = 0.500$ Å and $R = 6.500$ Å in steps of $\Delta R = 0.025$ Å. The molecular orbital coefficients and CI vectors were optimised to convergence thresholds of 10^{-6}. The orbital coefficients and all CI vectors with values larger than $5 \cdot 10^{-5}$ were stored for later use.

Quantum Dynamics Simulation

The time-evolution of a quantum mechanical nuclear wave packet prepared by laser excitation from the electronic ground state to the first excited state, $X^1\Sigma_g^+ \rightarrow B^1\Sigma_u^+$, was simulated with the split-operator method[63,64] implemented in the WavePacket programme[65] in MATLAB. The calculation was performed on a spatial grid ranging from $R = 0.500$ Å to $R = 6.500$ Å with a spacing of $\Delta R = 0.005$ Å. The initial wave packet was the vibrational ground state of $X^1\Sigma_g^+$ calculated with the Fourier DVR method[66] in the same programme. With the laser pulse centred at $t = 0.00$ fs, the wave packet was propagated from $t = -100.00$ fs to $t = 350.00$ fs in steps of $\Delta t = 0.01$ fs.

The laser pulse was described by a Gaussian shaped envelope with a pulse duration (FWHM) of 25.00 fs. It had a mean photon energy of 14.3 eV and its electric field amplitude was optimised to 53.8 MV/cm, corresponding to a peak intensity of 7.69 TW/cm^2, to yield a population of 10.0% in the $B^1\Sigma_u^+$ state at the end of the excitation process. The transitions $X^1\Sigma_g^+ \rightarrow C^1\Pi_u$ and $X^1\Sigma_g^+ \rightarrow B'^1\Sigma_u^+$ were not included for the sake of simplicity. A wave packet similar to the one simulated here has already been probed by strong-field dissociative ionisation.[67]

The accurate potential energy curves[68,69] and transition dipole moments[70] of Wolniewicz were used. The data was interpolated by the WavePacket programme to match the spatial grid. Even though the $B^1\Sigma_u^+$ state is energetically close to other excited states, the next state of the same symmetry, $B'^1\Sigma_u^+$, is well separated by more than 2 eV in the vicinity of their minima

and the non-adiabatic coupling[71] of $B^1\Sigma_u^+$ and $B'^1\Sigma_u^+$ is not strong enough to make their diabatised potentials cross. The dynamics in the $B^1\Sigma_u^+$ state were therefore described adiabatically.

Calculation of One-Electron Scattering Matrix Elements

17 different one-electron scattering matrix elements $L_{fi}(\boldsymbol{q}_0, R)$ were calculated from the wave function data that was stored in the CASSCF calculations for the two initial states $X^1\Sigma_g^+$ and $B^1\Sigma_u^+$. With 241 points on the spatial grid defined in section 8.1, 4097 scattering matrix elements were computed in total. Each of these matrix elements was evaluated on a two-dimensional grid with 1210 points distributed over the origin and 19 equally spaced concentric circles in the q_x-q_y-plane of the reciprocal space. The bond of the hydrogen molecule was aligned with the x-axis in real space. The incident X-ray pulse was propagating in z-direction and had a mean photon energy of $\hbar\omega_0 = 8.5$ keV. The matrix elements were corrected to conserve their phase over the full range of internuclear distances. The calculations were performed with a code based on analytical Fourier transforms of Gaussian-type orbitals as detailed in references 24 and 72.

Simulation of Time-Resolved X-Ray Scattering

The elastic, inelastic, and coherence contributions to the total differential scattering signal given in equations (3.18), (3.19), (3.22), and (3.17) were calculated from the electronic energies, the nuclear wave packet, and the one-electron scattering matrix elements. Following the calculation of the latter, a perfect orientation of the molecule along the x-axis in gas phase was assumed. No rotational eigenstates were considered. The integrals over t and R were evaluated numerically by use of the trapezoidal rule. The scattering matrix elements were interpolated to steps of $\Delta R = 0.005$ Å to ensure converged integration and to match the spatial grid of the quantum dynamics simulation. The same temporal grid as for the quantum dynamics simulation was used. The X-ray scattering signal was simulated for pump-probe delays τ between $\tau = -30.00$ fs and $\tau = 280.00$ fs. Difference scattering signals $\Delta dS/d\Omega$ were obtained by subtraction of the stationary ground state signal at $\tau = -100.00$ fs from signals at later times (pump-on minus pump-off).

The incident X-ray pulse was assumed to be transform limited. Its photon number intensity $I(t - \tau)$ was described by a normalised Gaussian as in equation (7.5) and the detection window $W_{fij}(\Delta\omega)$ from equation (7.9) was applied.

Two different pulse durations were chosen, $d_\mathrm{p} = 10.00$ fs and $d_\mathrm{p} = 100$ as. Values of $\hbar\Delta\omega = 16.0$ eV and $\hbar\Delta\omega = 50.0$ eV ensured that the approximation made in equation (3.15) was justified. For such detection windows, not

only the vibrational but also all electronic transitions were weighted equally and the simulation was performed in the limit of equation (3.25) rather than of equation (3.17). The closely lying excited states of the hydrogen molecule did not allow a strict distinction of the orders of magnitude of the vibrational and electronic energies. Consequently, a fully converged calculation in terms of one-electron scattering matrix elements was impossible, as it would have required a vast and impractical amount of states. The strengths of the inelastic and the coherence contributions relative to the elastic signal were therefore underestimated. Qualitatively, however, the unconverged simulation provided correct and meaningful results: the symmetries of the patterns as well as the trends in their changes became manifest.

8.2 Results

Potential Energy Curves

The potential energy curves obtained from the CASSCF calculations are shown in Figure **8.8**. They are in reasonable agreement with the accurate data of Wolniewicz[68,69,73–75]. The potentials of the $X^1\Sigma_g^+$ and the $B^1\Sigma_u^+$ states deviate by 66 meV and 69 meV at most and by 15 meV and 37 meV on average. The two states with highest energy and gerade symmetry, $GK^1\Sigma_g^+$ and $I^1\Pi_g$, display the largest deviations of 176 meV at most and of 40 meV on average, respectively. Additional single-point MRCI[76–78] calculations led only to insignificant improvements of the energies, confirming that the chosen active space yields results close to the full-CI limit of the d-aug-cc-pVQZ basis set. A better description, particularly of the most energetic states, would require an explicit Rydberg basis[79]. Such a basis would also permit a reliable calculation of even higher excited electronic states. For the purpose of this work, however, the accuracy of the state-average CASSCF(2,30)/d-aug-cc-pVQZ approach is sufficient.

Nuclear Wave Packet

The nuclear density of the $B^1\Sigma_u^+$ state, $\rho_B(R,t) = |\chi_B(R,t)|^2$, is shown in Figure **8.9**. The wave packet gains amplitude by excitation from the $X^1\Sigma_g^+$ ground state at around $t = 0.00$ fs and 0.76 Å and moves down the potential energy curve towards larger internuclear distance R. At $t = 30.59$ fs the mean bond length $\langle R \rangle$ reaches a maximum of $\langle R \rangle = 5.18$ Å, the first outer turning point, and the wave packet oscillates back towards a smaller internuclear distance. Similarly, at $t = 62.05$ fs the wave packet arrives at a minimum of $\langle R \rangle = 2.33$ Å, the first inner turning point. With a period of roughly $T_B \approx 62$ fs, the wave packet continues to oscillate between its outer and inner turning points at times 92.69 fs, 124.51 fs, 154.74 fs, 186.29 fs, 216.55 fs, 248.00 fs, and 278.03 fs with mean bond lengths 5.13 Å, 2.49 Å, 5.05 Å, 2.68 Å, 4.93 Å, 2.88 Å, and 4.80 Å, respectively. The decrease

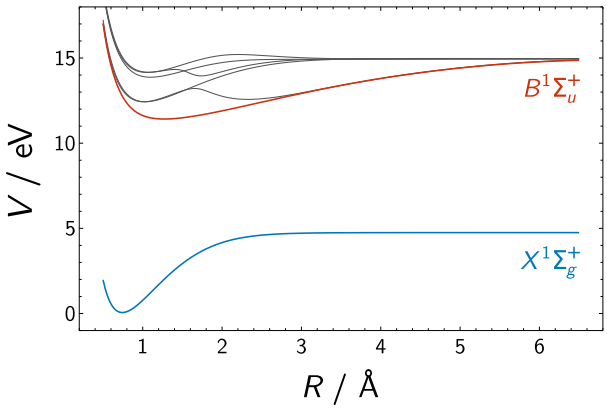

Fig. 8.8: Potential energy curves $V_k(R)$ of the first nine electronic singlet states of the H_2 molecule at different internuclear distances R. The potentials of the ground state $X^1\Sigma_g^+$ and of the first excited state $B^1\Sigma_u^+$ are labelled. The curves of $EF^1\Sigma_g^+$, $C^1\Pi_u$, $GK^1\Sigma_g^+$, $B'^1\Sigma_u^+$, and $I^1\Pi_g$ are following with increasing energy. The potentials of $EF^1\Sigma_g^+$ and $GK^1\Sigma_g^+$ have a double-well, $C^1\Pi_u$ and $I^1\Pi_g$ are degenerate. The potentials were calculated with state-average CASSCF(2,30)/d-aug-cc-pVQZ.

of $\langle R \rangle$ at the outer turning points and its increase at the inner turning points reveals that the amplitude of the oscillation is slightly damped due to dispersion of the wave packet. The nodal structure that appears in the density after its first half-period in R reflects the high energy of the wave packet. The 14.3 eV of the pump pulse are sufficient to excite up to the 28^{th} vibrational eigenstate of $B^1\Sigma_u^+$. The nuclear wave packet of $X^1\Sigma_g^+$ was only depleted by 10% and remained essentially stationary.

The evolution of the nuclear density $\rho_B(R,t)$ determines the changes in the elastic and inelastic scattering signal described by equations (3.18) and (3.19). The coherence in equation (3.22), however, refers to the product of the wave packets of the $X^1\Sigma_g^+$ and $B^1\Sigma_u^+$ states instead. Since $X^1\Sigma_g^+$ is *gerade* and $B^1\Sigma_u^+$ is *ungerade*, the product of the two one-electron scattering matrix elements $L_{fX}(\boldsymbol{q}_0, R)\ L^*_{fB}(\boldsymbol{q}_0, R)$ is purely imaginary-valued for all final states with index f. This follows from the discussion around equations (5.2) to (5.4). Hence, only the imaginary part of $\chi_X(R,t)\ \chi^*_B(R,t)$ can contribute to the scattering signal via equation (3.22). The imaginary part exhibits a rapid oscillation on the time scale of the electronic motion with a period of $T_e \approx 289$ as, corresponding to the carrier frequency of the pump pulse. On top of this oscillation, the imaginary part contains an envelope that represents the overlap of the two wave packets $\chi_X(R,t)$ and $\chi^*_B(R,t)$. The envelope shown in Figure **8.10** is non-zero only in the narrow range of internuclear distances around 0.76 Å where both wave packets overlap. Correspondingly, the envelope has maxima at times around 0 fs,

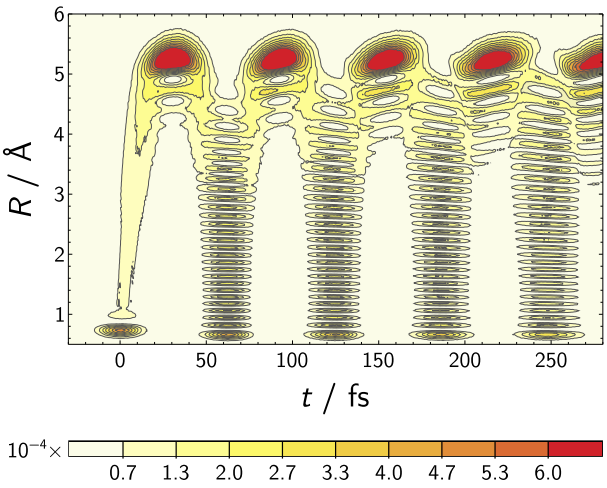

Fig. 8.9: Contour plot of the simulated nuclear density $\rho_B(R,t) = |\chi_B(R,t)|^2$ of the first excited state $B^1\Sigma_u^+$ at different internuclear distances R and times t. The nuclear wave packet $\chi_B(R,t)$ was prepared by laser excitation from the vibrational ground state of $X^1\Sigma_g^+$. The laser pulse was centred at $t = 0.00$ fs, had a duration of 25.00 fs, a mean photon energy of 14.3 eV, and a peak intensity of 7.69 TW/cm^2. The final population in $B^1\Sigma_u^+$ is 10.0%.

63 fs, 126 fs, 184 fs, and 245 fs. At $t = 0$ fs, when $\chi_B^*(R,t)$ mostly resembles the Franck-Condon wave packet, the envelope has its global maximum. The local maxima at later times are somewhat smaller, as $\chi_B^*(R,t)$ disperses. When the wave packet is close to the outer turning points at around 34 fs, 91 fs, 152 fs, 215 fs, and 276 fs, the envelope becomes almost zero, revealing that $\chi_B^*(R,t)$ moves out of coherence with $\chi_X(R,t)$. The nodal structure of $\chi_B^*(R,t)$ in R is also visible in Figure **8.10**.

Time-Resolved X-Ray Scattering

The elastic (e) and inelastic (i) contributions to the total (t) difference scattering patterns $\Delta dS/d\Omega$ (pump-on minus pump-off) for a X-ray probe pulse with a duration of $d_\mathrm{p} = 10.00$ fs are shown in Figure **8.11**. Five representative pump-probe delays τ covering two full periods of the nuclear oscillation were chosen. At each of these five pump-probe delays the wave packet $\chi_B(R,t)$ is close to one of its inner or outer turning points and the rapidly oscillating $\mathrm{Im}\big(\chi_X(R,t)\ \chi_B^*(R,t)\big)$ has a maximum.

The elastic difference scattering patterns in the first row of Figure **8.11** are negative at all coordinates in the q_x-q_y plane at all pump-probe delays τ. This reflects that the one-electron density of the $B^1\Sigma_u^+$ state is more diffuse than the density of the $X^1\Sigma_g^+$ ground state. Furthermore, it illustrates that

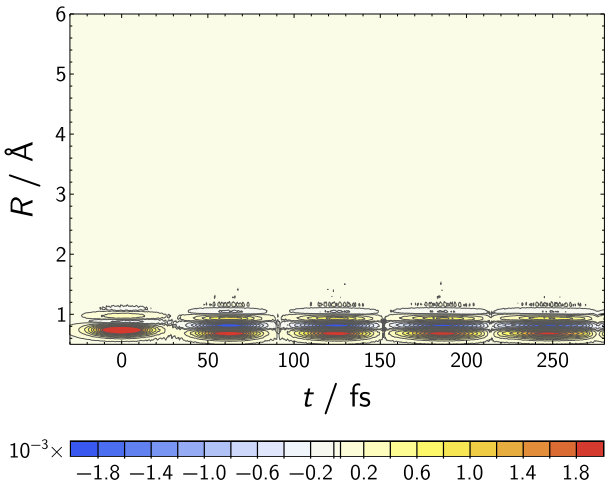

Fig. 8.10: Contour plot of the simulated envelope of $\mathrm{Im}\big(\chi_X(R,t)\ \chi_B^*(R,t)\big)$ at different internuclear distances R and times t. The quantity is associated with the coherence contribution to the scattering signal $dS_\mathrm{c}/d\Omega$. The nuclear wave packets were prepared as described in the caption of Figure **8.9**.

the independent atom model cannot provide a good approximation to the elastic scattering signal of few-electron molecules such as H_2, since it does not account for the observed change in the one-electron density due to excitation. In compliance with Friedel's law[41,50], the elastic patterns display a dihedral rosette group symmetry D_2 that contains a twofold rotation as well as two reflections, one through the q_x- and another one through the q_y-axis. Each pattern has two symmetric minima on the horizontal q_x-axis. At $\tau = 61.92$ fs and $\tau = 124.55$ fs when the nuclear wave packet $\chi_B(R,t)$ is close to its inner turning points, the minima take a value of roughly -0.26 at $q_x \approx \pm 0.91$ Å^{-1}. At $\tau = 30.59$ fs, $\tau = 92.64$ fs, and $\tau = 154.70$ fs when $\chi_B(R,t)$ is close to its outer turning points, the minima decrease to -0.34 and move closer to the origin to $q_x \approx \pm 0.68$ Å^{-1}. These changes reveal that one-electron density is shifted from the centre of the molecule towards its periphery, thereby adjusting to the increase of the internuclear distance.

The inelastic difference scattering signal in the second row of Figure **8.11** is mainly positive, particularly in the vicinity of the q_x-q_y coordinates where the elastic patterns have their minima. As the elastic patterns, the inelastic ones display a D_2 rosette group symmetry. They have two symmetric maxima on the q_x-axis. At $\tau = 61.92$ fs and $\tau = 124.55$ fs, these maxima take a value of roughly $4.7 \cdot 10^{-2}$ at $q_x \approx \pm 0.74$ Å^{-1}. At $\tau = 30.59$ fs, $\tau = 92.64$ fs, and $\tau = 154.70$ fs, the maxima drop to approximately $3.3 \cdot 10^{-2}$ and move closer to the origin to $q_x \approx \pm 0.56$ Å^{-1}. As before, these changes are related to the increase of the internuclear distance. The magnitudes of the off-diagonal one-electron scattering matrix elements are usually largest at

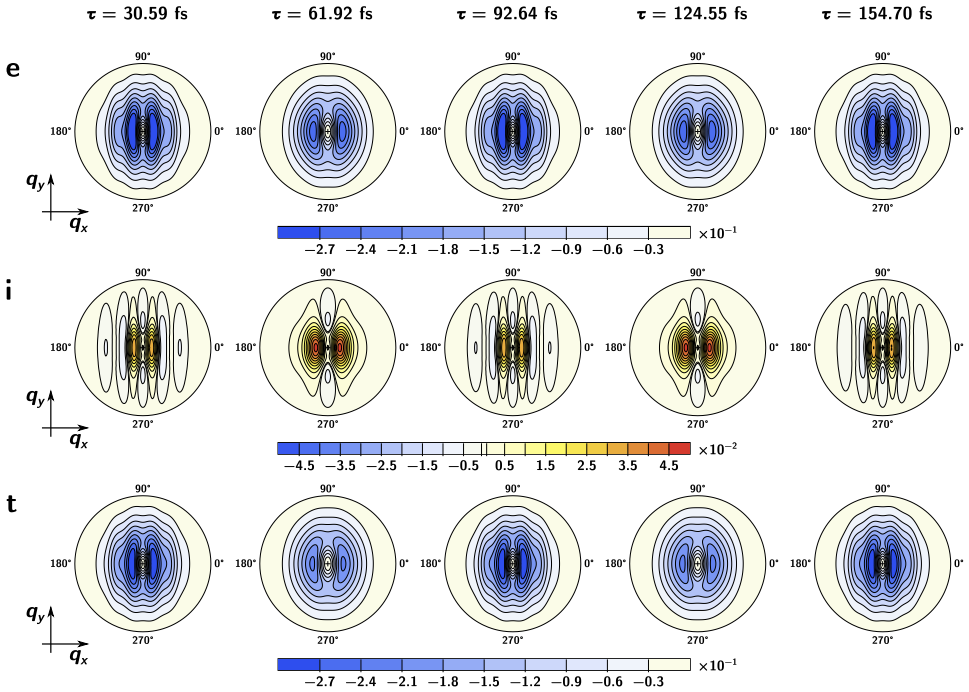

Fig. 8.11: Contour plots of the elastic (**e**), inelastic (**i**), and total (**t**) time-resolved difference X-ray scattering patterns $\Delta dS/d\Omega$ (pump-on minus pump-off) in the q_x-q_y plane at five pump-probe delays τ. The scattering intensity is given in electronic units. The radiation is scattered by the H_2 molecule subsequent to the laser induced transition $X^1\Sigma_g^+ \rightarrow B^1\Sigma_u^+$ at around $\tau = 0$ fs. The incident probe pulse propagates along the z-axis and has a mean photon energy of $\hbar\omega_0 = 8.5$ keV and a time duration (FWHM) of $d_\mathrm{p} = 10.00$ fs. All scattered photons within the range of $\pm\hbar\Delta\omega = 16.0$ eV around $\hbar\omega_0$ are detected. With photons scattered up to 90°, the q_x and q_y coordinates take values between ± 4.31 Å^{-1}. The angular coordinate is the azimuthal angle of the $\boldsymbol{q}$-vector, ϕ_q. The five pump-probe delays τ cover two full periods of the oscillation of the nuclear wave packet $\chi_B(R,t)$ with $T_B \approx 62$ fs. At $\tau = 30.59$ fs, $\tau = 92.64$ fs, and $\tau = 154.70$ fs, the wave packet is close to its outer turning points. At $\tau = 61.92$ fs and $\tau = 124.55$ fs, it is close to its inner turning points.

mean H–H bond lengths close to the minima of their corresponding electronic potential energy curves. When the molecule expands beyond these bond lengths, the magnitude of the matrix elements tends to drop. Hence, both the positive and negative values of the inelastic difference scattering signal decrease when the excited state wave packet is moving in direction of its outer turning points.

Furthermore, the fact that the inelastic difference patterns are mainly positive implies that the incident X-ray photons are more likely to cause an electronic transition from the $B^1\Sigma_u^+$ than from the $X^1\Sigma_g^+$ state. Especially transitions to states with *gerade* inversion symmetry, most notably $B^1\Sigma_u^+ \rightarrow EF^1\Sigma_g^+$, tend to be associated with a stronger inelastic scattering signal than the corresponding transition from the ground state. Transitions to states with *ungerade* inversion symmetry such as $B^1\Sigma_u^+ \rightarrow C^1\Pi_u$, in contrast, tend to be linked to a weaker signal. These trends can be understood by further inspection of the properties of the one-electron scattering matrix elements as follows. Making use of the Maclaurin series expansion of the one-electron scattering operator $\hat{\boldsymbol{L}} = \sum_n \exp(\iota \boldsymbol{q} \cdot \boldsymbol{r}_n)$:

$$\hat{\boldsymbol{L}} = \sum_n \left[1 + \iota \boldsymbol{q} \cdot \boldsymbol{r}_n - \frac{1}{2!} \cdot (\boldsymbol{q} \cdot \boldsymbol{r}_n)^2 - \frac{\iota}{3!} \cdot (\boldsymbol{q} \cdot \boldsymbol{r}_n)^3 + \dots\right], \tag{8.1}$$

even (*gerade*) and odd (*ungerade*) terms of $\hat{\boldsymbol{L}}$ can be identified:

$$\begin{aligned} \hat{\boldsymbol{L}}_{\boldsymbol{g}} &= \sum_n \left[1 - \frac{1}{2} \cdot (\boldsymbol{q} \cdot \boldsymbol{r}_n)^2 + \frac{1}{24} \cdot (\boldsymbol{q} \cdot \boldsymbol{r}_n)^4 + \dots\right], \\ \hat{\boldsymbol{L}}_{\boldsymbol{u}} &= \sum_n \left[\iota \boldsymbol{q} \cdot \boldsymbol{r}_n - \frac{\iota}{6} \cdot (\boldsymbol{q} \cdot \boldsymbol{r}_n)^3 + \frac{\iota}{120} \cdot (\boldsymbol{q} \cdot \boldsymbol{r}_n)^5 + \dots\right]. \end{aligned} \tag{8.2}$$

Two cases can be distinguished now. First, a one-electron scattering matrix element can imply a $g \rightarrow g$ or a $u \rightarrow u$ transition. Only $\hat{\boldsymbol{L}}_{\boldsymbol{g}}$ in equation (8.2) yields non-vanishing results then, since the product of both state vectors and the operator has to be *gerade* in order for the integral not to vanish. Moreover, the first term of $\hat{\boldsymbol{L}}_{\boldsymbol{g}}$ cannot contribute due to the orthonormality of the bra and the ket. Second, a matrix element can imply a $g \rightarrow u$ or $u \rightarrow g$ transition. Only $\hat{\boldsymbol{L}}_{\boldsymbol{u}}$ is relevant in this case. Hence, the first terms that are contributing to the matrix elements are $-\sum_n (\boldsymbol{q} \cdot \boldsymbol{r}_n)^2/2$ and $\sum_n \iota \boldsymbol{q} \cdot \boldsymbol{r}_n$ in case one and two, respectively. If the electronic states have amplitude mostly at small values of $\boldsymbol{r}_n$, one can therefore expect that $\hat{\boldsymbol{L}}_{\boldsymbol{u}}$ leads to larger scattering matrix elements than $\hat{\boldsymbol{L}}_{\boldsymbol{g}}$. Consequently, the inelastic signal should be large when $g \rightarrow u$ or $u \rightarrow g$ and small when $g \rightarrow g$ or $u \rightarrow u$.

Moreover, the relative magnitude of scattering matrix elements roughly follows the inverse difference of the eigenenergies of their corresponding electronic states. Since the potential energy curves of $B^1\Sigma_u^+$ and $EF^1\Sigma_g^+$ are close, the scattering matrix element that couples both states is relatively large. The resulting inelastic scattering signal related to $B^1\Sigma_u^+ \rightarrow EF^1\Sigma_g^+$ exceeds the loss of signal due to weaker $u \rightarrow u$ transitions like $B^1\Sigma_u^+ \rightarrow C^1\Pi_u$ at almost all points in the q_x-q_y plane. Only in a narrow range along the q_y axis, the difference signal is generally negative.

The total difference scattering patterns are shown in the third row of Figure **8.11**. It appears that the elastic signal is the dominant contribution. This is, however, partially a result of the incomplete convergence of the inelastic patterns. As mentioned before, the magnitude of the inelastic signal relative to the elastic one is smaller than it would be in a fully converged calculation. Nonetheless, it becomes apparent from Figure **8.11** that the inelastic difference signal adds to the time-dependent changes of the elastic one: the difference between the patterns at $\tau = 30.59$ fs and $\tau = 61.92$ fs, for instance, is larger for the total than for the purely elastic scattering. Even though the inelastic difference signal is mainly positive and thus predominantly weakens the negative elastic one, it amplifies the time-dependent changes by weakening the elastic signal most when it is already weakest.

The total difference scattering patterns in Figure **8.11** do not display any additional signatures of the coherence terms described by equation (3.22). With a duration of $d_\mathrm{p} = 10.00$ fs, the X-ray pulse cannot resolve the rapid, 289 as long oscillation of the imaginary part of $\chi_X(R,t)\ \chi_B^*(R,t)$ and the coherence terms have to vanish. In order to probe them, a much faster X-ray pulse is required.

Figure **8.12** shows the coherence contribution (c) to the total (t) difference scattering signal $\Delta dS/d\Omega$ for a X-ray probe pulse with a duration of just $d_\mathrm{p} = 100$ as at the same five pump-probe delays τ as before. Each pattern was calculated at a maximum of the rapid electronic oscillation. In contrast to the previously discussed elastic and inelastic scattering, the coherence patterns do not display a centrosymmetric symmetry. Since the coherence signals change sign when reflected through the vertical q_y-axis, the patterns transform according to the less symmetric D_1 rosette group. Consequently, the coherence contribution is completely anisotropic and can only be resolved as long as the molecule is at least partially aligned. In case of an ensemble of molecules with random orientation in the x-y plane, the positive and negative parts of the signal would cancel each other.

The coherence patterns in Figure **8.12** have a minimum in the negative and a maximum in the positive range of q_x-values on the q_x-axis. At $\tau = 61.92$ fs and $\tau = 124.55$ fs, the extrema take values of roughly $\pm 1.0 \cdot 10^{-2}$ at $q_x \approx \pm 1.45$ Å^{-1}, respectively. At $\tau = 30.59$ fs, $\tau = 92.64$ fs, and $\tau = 154.70$ fs, they drop to less than $\pm 0.1 \cdot 10^{-2}$. This relates directly to the envelope of $\mathrm{Im}\big(\chi_X(R,t)\ \chi_B^*(R,t)\big)$ shown in Figure **8.10**: the coherence signal is strongest when $\chi_B(R,t)$ is close to its inner turning point and almost vanishes when the wave packets is close to its outer turning point. This becomes even clearer by inspection of the integrated absolute value of the difference coherence signal:

$$\Upsilon = \frac{1}{2\pi q_\mathrm{m}} \cdot \int_0^{q_\mathrm{m}} \int_0^{2\pi} \left| \Delta \frac{dS_\mathrm{c}}{d\Omega} \right| \, d\phi_q \, dq, \tag{8.3}$$

where q_m is the upper limit of the radial coordinate q and ϕ_q is the azimuthal angle in $\boldsymbol{q}$-space. The values of Υ for pump probe delays between $\tau = -30.00$ fs and $\tau = 280.00$ fs are shown in Figure **8.13**. Again, all data points were obtained at maxima of the rapid electronic oscillation. The quantity Υ has local maxima of roughly $8.4 \cdot 10^{-3}$, $2.6 \cdot 10^{-3}$, $2.5 \cdot 10^{-3}$, $2.3 \cdot 10^{-3}$, and $2.2 \cdot 10^{-3}$ at pump-probe delays τ around 0 fs, 63 fs, 127 fs, 187 fs, and 245 fs, respectively. At times 34 fs, 91 fs, 152 fs, 214 fs, and 276 fs, Υ becomes almost zero. The integrated coherence scattering signal Υ

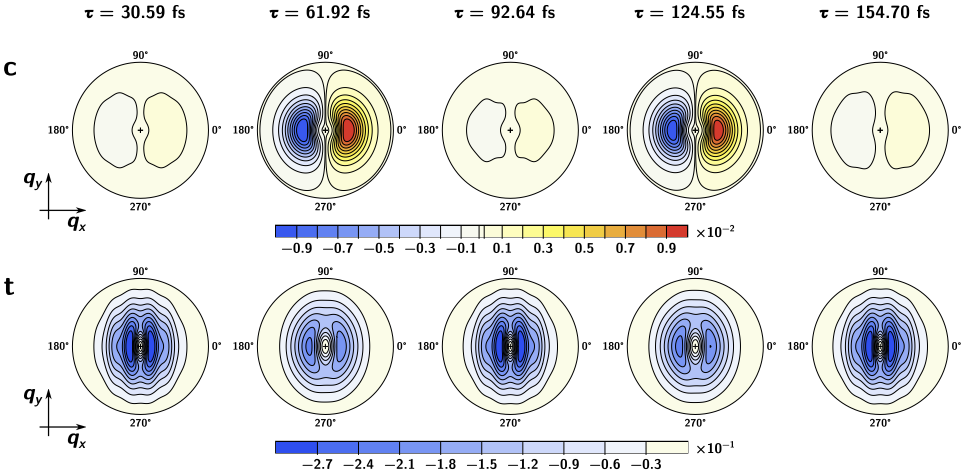

Fig. 8.12: Contour plots of the coherence (**c**) and total (**t**) time-resolved difference X-ray scattering patterns $\Delta dS/d\Omega$ (pump-on minus pump-off) in the q_x-q_y plane at five pump-probe delays τ. The scattering intensity is given in electronic units. The radiation is scattered by the H_2 molecule subsequent to the laser induced transition $X^1\Sigma_g^+ \rightarrow B^1\Sigma_u^+$ at around $\tau = 0$ fs. The incident probe pulse propagates along the z-axis and has a mean photon energy of $\hbar\omega_0 = 8.5$ keV and a time duration (FWHM) of $d_\mathrm{p} = 100$ as. All scattered photons within the range of $\pm\hbar\Delta\omega = 50.0$ eV around $\hbar\omega_0$ are detected. With photons scattered up to 90°, the q_x and q_y coordinates take values between ± 4.31 Å^{-1}. The angular coordinate is the azimuthal angle of the $\boldsymbol{q}$-vector, ϕ_q. The five pump-probe delays τ cover two full periods of the oscillation of the nuclear wave packet $\chi_B(R,t)$ with $T_B \approx 62$ fs. At $\tau = 30.59$ fs, $\tau = 92.64$ fs, and $\tau = 154.70$ fs, the wave packet is close to its outer turning points. At $\tau = 61.92$ fs and $\tau = 124.55$ fs, it is close to its inner turning points. The rapid oscillation of $\mathrm{Im}\left[\chi_X(R,t)\ \chi_B^*(R,t)\right]$ has a maximum at all pump-probe delays.

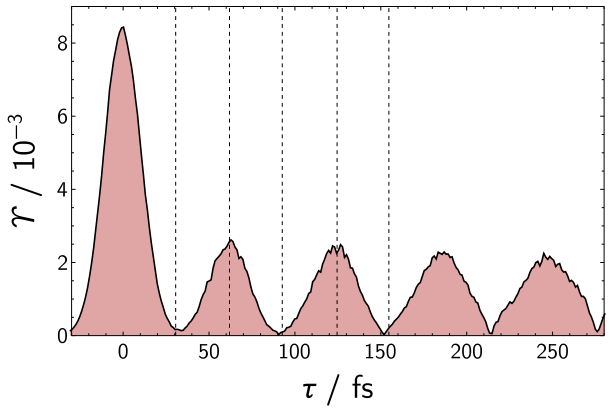

Fig. 8.13: Envelope of the integrated absolute value of the coherence contribution to the total difference scattering signal Υ as defined in equation (8.3) at different pump-probe delays τ. The vertical dashed lines show the pump-probe delays from Figure **8.12**.

thus reveals the dynamics of the envelope of $\mathrm{Im}\big(\chi_X(R,t)\ \chi_B^*(R,t)\big)$ shown in Figure **8.10** and can be understood as a measure of the degree of electronic coherence in the system. Moreover, the decrease of the maxima of Υ, most notably from $\tau = 0$ fs to $\tau = 63$ fs, provides quantitative information about the dispersion of $\chi_B(R,t)$.

In comparison to the elastic difference scattering signal the coherence contribution shown in Figure **8.12** is relatively weak. As in case of the inelastic scattering, the weakness of the signal is partially an artefact of the incomplete convergence of the calculation. It is, however, also a consequence of the convolution of the signal with the photon number intensity of the X-ray pulse: for a pulse-duration of $d_\mathrm{p} = 100$ as and a sinusoidal oscillation with a period of $T_\mathrm{e} \approx 289$ as, at most 65% of the instantaneous signal can be resolved. But even though the coherence contribution in Figure **8.12** is small, its signature is clearly visible in the total difference scattering patterns. At $\tau = 61.92$ fs and $\tau = 124.55$ fs the symmetry of the patterns is markedly broken to D_1, whereas the deviation from D_2 at $\tau = 30.59$ fs, $\tau = 92.64$ fs, and $\tau = 154.70$ fs is negligible.

In addition to the effect of the nuclear motion visible in figures **8.12** and **8.13**, the rapid oscillation of $\mathrm{Im}\big(\chi_X(R,t)\ \chi_B^*(R,t)\big)$ causes the coherence signal to vanish and to change sign on a much faster time scale. A full period of such an oscillation is shown in Figure **8.14**. The coherence signal at $\tau = 61.92$ fs becomes zero at $\tau = 61.85$ fs, $\tau = 61.99$ fs, and $\tau = 62.14$ fs and changes sign at $\tau = 62.06$ fs. The coherence patterns in Figure **8.14** are remarkably similar to those obtained for the electronic wave packet in the hydrogen atom in Figure **7.3**.

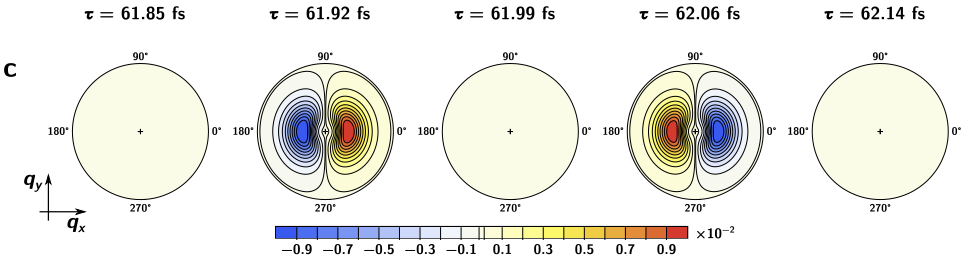

Fig. 8.14: Contour plots of the coherence (**c**) time-resolved difference X-ray scattering patterns $\Delta dS/d\Omega$ (pump-on minus pump-off) in the q_x-q_y plane at five pump-probe delays τ. The scattering intensity is given in electronic units. The radiation is scattered by the H_2 molecule subsequent to the laser induced transition $X^1\Sigma_g^+ \rightarrow B^1\Sigma_u^+$ at around $\tau = 0$ fs. The incident probe pulse propagates along the z-axis and has a mean photon energy of $\hbar\omega_0 = 8.5$ keV and a time duration (FWHM) of $d_\mathrm{p} = 100$ as. All scattered photons within the range of $\pm\hbar\Delta\omega = 50.0$ eV around $\hbar\omega_0$ are detected. With photons scattered up to 90°, the q_x and q_y coordinates take values between ± 4.31 Å^{-1}. The angular coordinate is the azimuthal angle of the $\boldsymbol{q}$-vector, ϕ_q. The five pump-probe delays τ cover a full period of the rapid sinusoidal oscillation in the coherence signal with $T_\mathrm{e} \approx 289$ as. At $\tau = 61.92$ fs and $\tau = 62.06$ fs, the oscillation has a maximum and a minimum, respectively. At $\tau = 61.85$ fs, $\tau = 61.99$ fs, and $\tau = 62.14$ fs, the signal is zero.

The fact that the coherence signal displays a different symmetry compared to the elastic and inelastic contributions can be exploited to isolate it from the total signal that would be measured in an experiment as follows. On condition that a difference scattering pattern is symmetric with respect to a reflection through the q_x-axis, it can be expanded in a series of Legendre polynomials $P_n\big(\cos\phi_q\big)$:

$$\Delta\frac{dS}{d\Omega} = \sum_{n=0}^{\infty} S_n(q)\; P_n\big(\cos\phi_q\big), \tag{8.4}$$

where the radial functions $S_n(q)$ are obtained by projection of the difference scattering signal $\Delta dS/d\Omega$ onto the corresponding Legendre polynomials of order n:

$$S_n(q) = \frac{2n+1}{2} \cdot \int_0^\pi \sin\phi_q\; P_n\big(\cos\phi_q\big)\; \Delta\frac{dS}{d\Omega}\; d\phi_q. \tag{8.5}$$

This expansion has already been used in experimental studies where time-resolved X-ray scattering subsequent to one-photon excitation of an ensemble of randomly oriented molecules was investigated.[80,81] In these studies

equation (8.5) allowed a separation of the isotropic and anisotropic signals $S_0(q)$ and $S_2(q)$, respectively.[22,23,82] If equations (8.4) and (8.5) are applied to the total differential scattering patterns in Figure **8.12**, the elastic and inelastic contributions project onto polynomials with even order, whereas the coherence contribution projects onto odd order only:

$$\begin{aligned} \Delta\frac{dS_\mathrm{e}}{d\Omega} + \Delta\frac{dS_\mathrm{i}}{d\Omega} &= \sum_{n=0}^{\infty} S_{2n}(q)\ P_{2n}\big(\cos\phi_q\big), \\ \Delta\frac{dS_\mathrm{c}}{d\Omega} &= \sum_{n=0}^{\infty} S_{2n+1}(q)\ P_{2n+1}\big(\cos\phi_q\big). \end{aligned} \tag{8.6}$$

Radial functions $S_n(q)$ of the total difference scattering patterns at $\tau = 61.92$ fs are shown in Figure **8.15** for even and odd orders of n, respectively. An insertion of the six functions $S_0(q)$, $S_2(q)$, $S_4(q)$, $S_6(q)$, $S_8(q)$, and $S_{10}(q)$ from Figure **8.15 A** into the first line of equation (8.6) reproduces the sum of the elastic and inelastic difference signals within numerical accuracy. Similarly, the three functions $S_1(q)$, $S_3(q)$, and $S_5(q)$ from figure **8.15 B** and the second line of equation (8.6) permit the construction of the pure coherence signal displayed in Figure **8.12**. The magnitude of the radial functions in Figure **8.15** decreases quickly with increasing order n.

Alternatively, one could make use of the different timescales of the electronic and nuclear motion to extract the pure coherence signal. At pump-probe delays $\tau = 61.85$ fs and $\tau = 61.99$ fs, the total scattering signal is the sum of its elastic and inelastic contributions. Since these contributions oscillate with the period of the nuclear density, $T_B \approx 62$ fs, they remain almost stationary on the attosecond time scale of the rapid electronic oscillation. Hence, one can approximate the sum of the elastic and inelastic contributions at $\tau = 61.92$ fs by the mean of the signals at $\tau = 61.85$ fs and $\tau = 61.99$ fs. A subtraction of this sum from the total difference scattering at $\tau = 61.92$ fs yields the isolated coherence signal.

These two approaches to extract the coherence contribution from the total scattering signal are, however, not always applicable. If the electronic coherence is caused by a population transfer *via* non-adiabatic coupling, both states will display the same inversion symmetry. It follows from the discussion around equations (5.2) to (5.4) that the coherence signal will be even in this case. It will thus project upon Legendre polynomial with even order, meaning that it is inseparable from the elastic and inelastic contributions. If no inversion symmetry is present, it will be possible that the coherence signal has both odd and even terms. Only the odd part can be isolated then. Moreover, the elastic and inelastic signals will not follow Friedel's law if equation (5.11) is not fulfiled. They will at least partially project upon

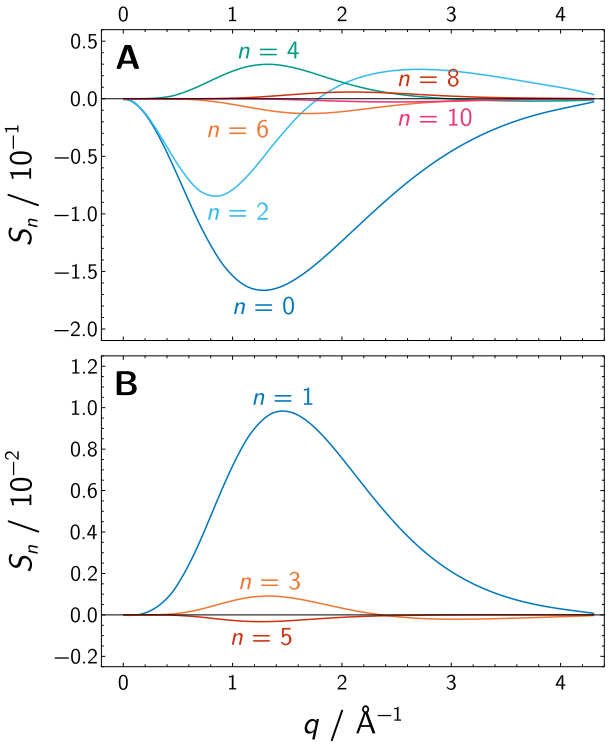

Fig. 8.15: Projection $S_n(q)$ of the total difference scattering signal (pump-on minus pump-off) at $\tau = 61.92$ fs onto Legendre polynomials $P_n\big(\cos\phi_q\big)$ as defined in equation (8.5). The scattering intensity is given in electronic units. (**A**) Even orders $n \in \{0, 2, 4, 6, 8, 10\}$. (**B**) Odd orders $n \in \{1, 3, 5\}$.

Legendre polynomials with odd order under such conditions, potentially preventing an extraction by means of equation (8.6).

The applicability of the second approach that makes use of the different timescales of the electronic and nuclear motion is limited as well. If the two states are non-adiabatically coupled and a population transfer is induced, the electronic and the nuclear motion will occur on the same timescale. The coherence signal cannot be identified by its rapid oscillation then.

The complete separability of the coherence contribution from the elastic and inelastic signals in Figure **8.12** is a consequence of the high symmetry of the hydrogen molecule, its relative orientation to the incident X-ray pulse, and of the fact that the electronic coherence was caused by UV excitation. In many other cases it may turn out that different contributions to the scattering singal are inseparable from each other. Signatures of electronic coherences could be untraceably hidden within a strong elastic and inelastic background. Future simulations of time-resolved X-ray scattering by less symmetric systems should further elucidate the matter.

Summary and Outlook

A theoretical framework for time-resolved non-resonant X-ray scattering by atoms and molecules based on quantum electrodynamics and first-order perturbation theory was developed. An expression for the differential scattering signal of a general material system was derived and further simplified for non-stationary states in atoms and molecules. The resulting expressions were discussed in the limits of different ranges of photon energies accepted by the detector. For a detection range smaller than the electronic transition energies of the material system, the scattering signal was described in terms of one-electron scattering matrix elements, *i.e.* Fourier transformed expectation values of the one-electron density operator. Three contributions to the differential scattering signal were identified: elastic and inelastic scattering as well as scattering related to electronic coherences of the material system. For a detection range much larger than the electronic transition energies, the scattering signal was described in terms of two-electron scattering matrix elements, *i.e.* Fourier transformed expectation values of the two-electron density operator. Three contributions to the differential scattering signal were identified: scattering by single electrons and scattering by two different electrons related either to a single electronic state or to an electronic coherence. The first two of these contributions were shown to be the one- and two-electron parts of the elastic plus inelastic scattering signal in the limit of large detection ranges. This correspondence revealed that the common assumption of the differential scattering signal being mainly elastic is not justified under these conditions. The breakdown of the elastic picture became even more apparent in the context of scattering related to electronic coherences that was shown to be fundamentally different from the elastic and inelastic signals.

Technical issues that facilitate the evaluation of one-electron scattering matrix elements and thus the simulation of differential scattering signals were discussed. Geometric relations of the coordinates in reciprocal space were provided. Three important properties of the one-electron scattering matrix elements were scrutinised. Most notably, Friedel's law for two-dimensional scattering patterns of atoms and molecules in the gas phase was discussed. It was shown that the elastic and inelastic patterns obey Friedel's law as

long as the corresponding one-electron densities or one-electron transition densities are symmetric under reflection through the detector plane in real space. Moreover, an analytic solution to one-electron scattering matrix elements of the hydrogen atom was derived. This generalised an expression published by Schnaidt in 1934 [38] and allowed a computationally efficient and mathematically exact evaluation of the X-ray scattering signal of the hydrogen atom in any non-stationary state.

The theoretical framework was applied in two simulations.

The differential scattering signal of an electronic wave packet of superposed $|3d_{z^2}\rangle$ and $|4f_{z^3}\rangle$ orbitals of the hydrogen atom was simulated. The numerical results of Dixit, Vendrell, and Santra [25] were reproduced by application of the analytic solution to the scattering matrix elements of the hydrogen atom. Thereby, the general equivalence of the formalisms of Dixit *et al.* and of Henriksen and Møller as well as the applicability of the analytic approach was illustrated. All contributions to the scattering signal were evaluated and analysed. It was shown that the time-dependence of the scattering signal was caused by the contributions related to the electronic coherence, whereas the elastic and inelastic signals were independent of time. The effect of the pulse duration on the scattering signal was revised. It was demonstrated that the existence of an optimum pulse duration at which the scattering signal displayed the strongest time-dependence was entirely due to a restriction on the range of photon energies that were accepted by the detector.

The differential scattering signal of the hydrogen molecule subsequent to UV excitation from its $X^1\Sigma_g^+$ ground state to its $B^1\Sigma_u^+$ excited state was simulated. To the best of the author's knowledge, this was the first full simulation of two-dimensional time-resolved X-ray scattering patterns of a molecule. All contributions to the scattering signal were evaluated and analysed. The separability of the coherence contribution from the elastic and inelastic signal was discussed. It was shown that the coherence contribution was separable by projection of the total scattering signal onto Legendre polynomials or, alternatively, by means of the different timescales of the electronic and the nuclear motions. The coherence patterns looked remarkably similar to those simulated for the hydrogen atom.

The theory derived in this doctoral thesis and the codes developed to evaluate the scattering signal of the hydrogen molecule permit further simulations of time-resolved non-resonant X-ray scattering by molecules. An application to less symmetric and more complex molecules would provide further information about the nature of the different contributions to the scattering signal. The question to which degree the coherence contribution is separable from the total scattering signal should be discussed further, in particular for systems without inversion symmetry. A natural continuation of the work presented here could involve simulations of the differential scat-

tering signal for a heteronuclear diamtomic molecule that undergoes non-adiabatic dynamics or a bond dissociation. An extension to larger system with more than one nuclear degree of freedom, triatomic molecules to begin with, should also be pursued.

In addition, the development of a programme that directly computes two-electron scattering matrix elements from wave function data obtained with *ab initio* electronic structure calculations would benefit future research. A simulation of time-resolved X-ray scattering in terms of two-electron scattering matrix elements would eliminate the need to calculate a large amount of electronic states. Experiments with no restriction on the X-ray photon energies accepted by the detector would be better described by such an approach, since a truncation of the sum over the final states in simulations based on one-electron scattering matrix elements will always lead to results that are not completely converged. This problem will not occur if two-electron scattering matrix elements are used instead.

Finally, issues such as inelastic scattering that implies transitions into the continuum or imperfect alignment of the molecule should be considered in order to reproduce time-resolved non-resonant X-ray scattering experiments of atoms or molecules in gas phase.

Appendix

A Expansion of Atomic Orbitals

Tab. A.1: Real-valued atomic orbitals with principal quantum numbers $n \in \{1, 2, 3\}$ expressed as linear combinations of complex-valued eigenstates in parabolic coordinate space. The latter states are written as $\big|n, n_1, n_2\big\rangle$ where n_1 and n_2 are the parabolic quantum numbers.

Orbital	**Linear Combination**
$\big\|1s\big\rangle$	$\big\|1,0,0\big\rangle$
$\big\|2s\big\rangle$	$\frac{1}{\sqrt{2}} \cdot \Big(\big\|2,1,0\big\rangle + \big\|2,0,1\big\rangle\Big)$
$\big\|2p_x\big\rangle$	$\frac{1}{\sqrt{2}} \cdot \Big(\big\|2,0,0\big\rangle^* + \big\|2,0,0\big\rangle\Big)$
$\big\|2p_y\big\rangle$	$\frac{\iota}{\sqrt{2}} \cdot \Big(\big\|2,0,0\big\rangle^* - \big\|2,0,0\big\rangle\Big)$
$\big\|2p_z\big\rangle$	$\frac{1}{\sqrt{2}} \cdot \Big(\big\|2,1,0\big\rangle - \big\|2,0,1\big\rangle\Big)$
$\big\|3s\big\rangle$	$\frac{1}{\sqrt{3}} \cdot \Big(\big\|3,2,0\big\rangle + \big\|3,1,1\big\rangle + \big\|3,0,2\big\rangle\Big)$
$\big\|3p_x\big\rangle$	$\frac{1}{\sqrt{4}} \cdot \Big(\big\|3,1,0\big\rangle^* + \big\|3,1,0\big\rangle + \big\|3,0,1\big\rangle^* + \big\|3,0,1\big\rangle\Big)$
$\big\|3p_y\big\rangle$	$\frac{\iota}{\sqrt{4}} \cdot \Big(\big\|3,1,0\big\rangle^* - \big\|3,1,0\big\rangle + \big\|3,0,1\big\rangle^* - \big\|3,0,1\big\rangle\Big)$
$\big\|3p_z\big\rangle$	$\frac{1}{\sqrt{2}} \cdot \Big(\big\|3,2,0\big\rangle - \big\|3,0,2\big\rangle\Big)$
$\big\|3d_{x^2-y^2}\big\rangle$	$\frac{1}{\sqrt{2}} \cdot \Big(\big\|3,0,0\big\rangle^* + \big\|3,0,0\big\rangle\Big)$
$\big\|3d_{xy}\big\rangle$	$\frac{\iota}{\sqrt{2}} \cdot \Big(\big\|3,0,0\big\rangle^* - \big\|3,0,0\big\rangle\Big)$
$\big\|3d_{xz}\big\rangle$	$\frac{1}{\sqrt{4}} \cdot \Big(\big\|3,1,0\big\rangle^* + \big\|3,1,0\big\rangle - \big\|3,0,1\big\rangle^* - \big\|3,0,1\big\rangle\Big)$
$\big\|3d_{yz}\big\rangle$	$\frac{\iota}{\sqrt{4}} \cdot \Big(\big\|3,1,0\big\rangle^* - \big\|3,1,0\big\rangle - \big\|3,0,1\big\rangle^* + \big\|3,0,1\big\rangle\Big)$
$\big\|3d_{z^2}\big\rangle$	$\frac{1}{\sqrt{6}} \cdot \Big(\big\|3,2,0\big\rangle - 2 \cdot \big\|3,1,1\big\rangle + \big\|3,0,2\big\rangle\Big)$

Tab. A.2: Real-valued atomic orbitals with principal quantum number $n = 4$ expressed as linear combinations of complex-valued eigenstates in parabolic coordinate space. The latter states are written as $\big|n, n_1, n_2\big\rangle$ where n_1 and n_2 are the parabolic quantum numbers.

Orbital	**Linear Combination**
$\big\|4s\big\rangle$	$\frac{1}{\sqrt{4}} \cdot \Big(\big\|4,3,0\big\rangle + \big\|4,0,3\big\rangle + \big\|4,2,1\big\rangle + \big\|4,1,2\big\rangle\Big)$
$\big\|4p_x\big\rangle$	$\frac{1}{\sqrt{5}} \cdot \Big(\frac{\sqrt{3}}{2} \cdot \Big(\big\|4,2,0\big\rangle^* + \big\|4,2,0\big\rangle + \big\|4,0,2\big\rangle^* + \big\|4,0,2\big\rangle\Big) + \big\|4,1,1\big\rangle^* + \big\|4,1,1\big\rangle\Big)$
$\big\|4p_y\big\rangle$	$\frac{\iota}{\sqrt{5}} \cdot \Big(\frac{\sqrt{3}}{2} \cdot \Big(\big\|4,2,0\big\rangle^* - \big\|4,2,0\big\rangle + \big\|4,0,2\big\rangle^* - \big\|4,0,2\big\rangle\Big) + \big\|4,1,1\big\rangle^* - \big\|4,1,1\big\rangle\Big)$
$\big\|4p_z\big\rangle$	$\frac{1}{2\sqrt{5}} \cdot \Big(3 \cdot \Big(\big\|4,3,0\big\rangle - \big\|4,0,3\big\rangle\Big) + \big\|4,2,1\big\rangle - \big\|4,1,2\big\rangle\Big)$
$\big\|4d_{x^2-y^2}\big\rangle$	$\frac{1}{\sqrt{4}} \cdot \Big(\big\|4,1,0\big\rangle^* + \big\|4,1,0\big\rangle + \big\|4,0,1\big\rangle^* + \big\|4,0,1\big\rangle\Big)$
$\big\|4d_{xy}\big\rangle$	$\frac{\iota}{\sqrt{4}} \cdot \Big(\big\|4,1,0\big\rangle^* - \big\|4,1,0\big\rangle + \big\|4,0,1\big\rangle^* - \big\|4,0,1\big\rangle\Big)$
$\big\|4d_{xz}\big\rangle$	$\frac{1}{\sqrt{4}} \cdot \Big(\big\|4,2,0\big\rangle^* + \big\|4,2,0\big\rangle - \big\|4,0,2\big\rangle^* - \big\|4,0,2\big\rangle\Big)$
$\big\|4d_{yz}\big\rangle$	$\frac{\iota}{\sqrt{4}} \cdot \Big(\big\|4,2,0\big\rangle^* - \big\|4,2,0\big\rangle - \big\|4,0,2\big\rangle^* + \big\|4,0,2\big\rangle\Big)$
$\big\|4d_{z^2}\big\rangle$	$\frac{1}{\sqrt{4}} \cdot \Big(\big\|4,3,0\big\rangle + \big\|4,0,3\big\rangle - \big\|4,2,1\big\rangle - \big\|4,1,2\big\rangle\Big)$
$\big\|4f_{x(x^2-3y^2)}\big\rangle$	$\frac{1}{\sqrt{2}} \cdot \Big(\big\|4,0,0\big\rangle^* + \big\|4,0,0\big\rangle\Big)$
$\big\|4f_{y(3x^2-y^2)}\big\rangle$	$\frac{\iota}{\sqrt{2}} \cdot \Big(\big\|4,0,0\big\rangle^* - \big\|4,0,0\big\rangle\Big)$
$\big\|4f_{z(x^2-y^2)}\big\rangle$	$\frac{1}{\sqrt{4}} \cdot \Big(\big\|4,1,0\big\rangle^* + \big\|4,1,0\big\rangle - \big\|4,0,1\big\rangle^* - \big\|4,0,1\big\rangle\Big)$
$\big\|4f_{xyz}\big\rangle$	$\frac{\iota}{\sqrt{4}} \cdot \Big(\big\|4,1,0\big\rangle^* - \big\|4,1,0\big\rangle - \big\|4,0,1\big\rangle^* + \big\|4,0,1\big\rangle\Big)$
$\big\|4f_{xz^2}\big\rangle$	$\frac{1}{\sqrt{10}} \cdot \Big(\big\|4,2,0\big\rangle^* + \big\|4,2,0\big\rangle + \big\|4,0,2\big\rangle^* + \big\|4,0,2\big\rangle - \sqrt{3} \cdot \Big(\big\|4,1,1\big\rangle^* + \big\|4,1,1\big\rangle\Big)\Big)$
$\big\|4f_{yz^2}\big\rangle$	$\frac{\iota}{\sqrt{10}} \cdot \Big(\big\|4,2,0\big\rangle^* - \big\|4,2,0\big\rangle + \big\|4,0,2\big\rangle^* - \big\|4,0,2\big\rangle - \sqrt{3} \cdot \Big(\big\|4,1,1\big\rangle^* - \big\|4,1,1\big\rangle\Big)\Big)$
$\big\|4f_{z^3}\big\rangle$	$\frac{1}{2\sqrt{5}} \cdot \Big(\big\|4,3,0\big\rangle - \big\|4,0,3\big\rangle - 3 \cdot \Big(\big\|4,2,1\big\rangle - \big\|4,1,2\big\rangle\Big)\Big)$

B Rotation of Atomic Orbitals

Tab. B.1: Products of components expressed as linear combinations of real-valued atomic orbitals for arbitrary principal quantum numbers n and angular momentum quantum numbers of $l = 2$ (d) and $l = 3$ (f). The factors have been chosen to conserve the normalisation of the orbitals $\left|nd_{z^2}\right\rangle$ and $\left|nf_{z^3}\right\rangle$ under rotation. If other orbitals are rotated, the factors have to be modified accordingly.

Component	**Linear Combination**
$\left\|n\bar{d}_{x^2}\right\rangle$	$\frac{\sqrt{3}}{2}\left\|nd_{x^2-y^2}\right\rangle - \frac{1}{2}\left\|nd_{z^2}\right\rangle$
$\left\|n\bar{d}_{y^2}\right\rangle$	$-\frac{\sqrt{3}}{2}\left\|nd_{x^2-y^2}\right\rangle - \frac{1}{2}\left\|nd_{z^2}\right\rangle$
$\left\|n\bar{d}_{z^2}\right\rangle$	$\left\|nd_{z^2}\right\rangle$
$\left\|n\bar{d}_{xy}\right\rangle$	$\frac{\sqrt{3}}{2}\left\|nd_{xy}\right\rangle$
$\left\|n\bar{d}_{xz}\right\rangle$	$\frac{\sqrt{3}}{2}\left\|nd_{xz}\right\rangle$
$\left\|n\bar{d}_{yz}\right\rangle$	$\frac{\sqrt{3}}{2}\left\|nd_{yz}\right\rangle$
$\left\|n\bar{f}_{x^3}\right\rangle$	$\sqrt{\frac{5}{8}}\left\|nf_{x(x^2-3y^2)}\right\rangle - \sqrt{\frac{3}{8}}\left\|nf_{xz^2}\right\rangle$
$\left\|n\bar{f}_{y^3}\right\rangle$	$-\sqrt{\frac{5}{8}}\left\|nf_{y(3x^2-y^2)}\right\rangle - \sqrt{\frac{3}{8}}\left\|nf_{yz^2}\right\rangle$
$\left\|n\bar{f}_{z^3}\right\rangle$	$\left\|nf_{z^3}\right\rangle$
$\left\|n\bar{f}_{x^2y}\right\rangle$	$\sqrt{\frac{5}{8}}\left\|nf_{y(3x^2-y^2)}\right\rangle - \frac{1}{\sqrt{24}}\left\|nf_{yz^2}\right\rangle$
$\left\|n\bar{f}_{x^2z}\right\rangle$	$\sqrt{\frac{5}{12}}\left\|nf_{z(x^2-y^2)}\right\rangle - \frac{1}{2}\left\|nf_{z^3}\right\rangle$
$\left\|n\bar{f}_{xy^2}\right\rangle$	$-\sqrt{\frac{5}{8}}\left\|nf_{x(x^2-3y^2)}\right\rangle - \frac{1}{\sqrt{24}}\left\|nf_{xz^2}\right\rangle$
$\left\|n\bar{f}_{xz^2}\right\rangle$	$\sqrt{\frac{2}{3}}\left\|nf_{xz^2}\right\rangle$
$\left\|n\bar{f}_{y^2z}\right\rangle$	$-\sqrt{\frac{5}{12}}\left\|nf_{z(x^2-y^2)}\right\rangle - \frac{1}{2}\left\|nf_{z^3}\right\rangle$
$\left\|n\bar{f}_{yz^2}\right\rangle$	$\sqrt{\frac{2}{3}}\left\|nf_{yz^2}\right\rangle$
$\left\|n\bar{f}_{xyz}\right\rangle$	$\sqrt{\frac{5}{12}}\left\|nf_{xyz}\right\rangle$

Tab. B.2: Rotation of atomic $\left|nd\right\rangle$ orbitals with arbitrary principal quantum number n by polar and azimuthal angles of θ and ϕ, respectively. The rotations are expressed as angle-dependent linear combinations of atomic orbitals that share the same principal and angular momentum quantum numbers n and $l = 2$. The coefficients have been derived by operation of the rotation matrices $\hat{\boldsymbol{R}}_y(\theta)$ and $\hat{\boldsymbol{R}}_z(\phi)$ upon the corresponding orbital.

	Orbitals	**Coefficients**
$\left\|\tilde{nd}_{z^2}(\theta,\phi)\right\rangle$	$\left\|nd_{x^2-y^2}\right\rangle$	$\frac{\sqrt{3}}{2}\sin^2\theta\cos 2\phi$
	$\left\|nd_{xy}\right\rangle$	$\sqrt{3}\sin^2\theta\sin\phi\cos\phi$
	$\left\|nd_{xz}\right\rangle$	$\sqrt{3}\sin\theta\cos\theta\cos\phi$
	$\left\|nd_{yz}\right\rangle$	$\sqrt{3}\sin\theta\cos\theta\sin\phi$
	$\left\|nd_{z^2}\right\rangle$	$\frac{1}{4}\cdot\left(3\cos 2\theta+1\right)$
$\left\|\tilde{nd}_{xz}(\theta,\phi)\right\rangle$	$\left\|nd_{x^2-y^2}\right\rangle$	$\cos\theta\sin\theta\cos 2\phi$
	$\left\|nd_{xy}\right\rangle$	$2\cos\theta\sin\theta\sin\phi\cos\phi$
	$\left\|nd_{xz}\right\rangle$	$\cos 2\theta\cos\phi$
	$\left\|nd_{yz}\right\rangle$	$\cos 2\theta\sin\phi$
	$\left\|nd_{z^2}\right\rangle$	$-\sqrt{3}\sin\theta\cos\theta$
$\left\|\tilde{nd}_{yz}(\theta,\phi)\right\rangle$	$\left\|nd_{x^2-y^2}\right\rangle$	$-2\sin\theta\sin\phi\cos\phi$
	$\left\|nd_{xy}\right\rangle$	$\sin\theta\cos 2\phi$
	$\left\|nd_{xz}\right\rangle$	$-\cos\theta\sin\phi$
	$\left\|nd_{yz}\right\rangle$	$\cos\theta\cos\phi$
	$\left\|nd_{z^2}\right\rangle$	0
$\left\|\tilde{nd}_{xy}(\theta,\phi)\right\rangle$	$\left\|nd_{x^2-y^2}\right\rangle$	$-2\cos\theta\sin\phi\cos\phi$
	$\left\|nd_{xy}\right\rangle$	$\cos\theta\cos 2\phi$
	$\left\|nd_{xz}\right\rangle$	$\sin\theta\sin\phi$
	$\left\|nd_{yz}\right\rangle$	$-\sin\theta\cos\phi$
	$\left\|nd_{z^2}\right\rangle$	0

Tab. B.3: Rotation of atomic $\left|nd\right\rangle$ orbitals with arbitrary principal quantum number n by polar and azimuthal angles of θ and ϕ, respectively. The rotations are expressed as angle-dependent linear combinations of atomic orbitals that share the same principal and angular momentum quantum numbers n and $l = 2$. The coefficients have been derived by operation of the rotation matrices $\hat{\boldsymbol{R}}_y(\theta)$ and $\hat{\boldsymbol{R}}_z(\phi)$ upon the corresponding orbital.

	Orbitals	**Coefficients**
$\left\|\tilde{nd}_{x^2-y^2}(\theta,\phi)\right\rangle$	$\left\|nd_{x^2-y^2}\right\rangle$	$\frac{1}{2}\cdot\left(\cos^2\theta+1\right)\cdot\cos 2\phi$
	$\left\|nd_{xy}\right\rangle$	$\left(\cos^2\theta+1\right)\cdot\sin\phi\cos\phi$
	$\left\|nd_{xz}\right\rangle$	$-\sin\theta\cos\theta\cos\phi$
	$\left\|nd_{yz}\right\rangle$	$-\sin\theta\cos\theta\sin\phi$
	$\left\|nd_{z^2}\right\rangle$	$\frac{\sqrt{3}}{2}\sin^2\theta$

Tab. B.4: Rotation of atomic $\left|nf\right\rangle$ orbitals with arbitrary principal quantum number n by polar and azimuthal angles of θ and ϕ, respectively. The rotations are expressed as angle-dependent linear combinations of atomic orbitals that share the same principal and angular momentum quantum numbers n and $l = 3$. The coefficients have been derived by operation of the rotation matrices $\hat{\boldsymbol{R}}_y(\theta)$ and $\hat{\boldsymbol{R}}_z(\phi)$ upon the corresponding orbital.

	Orbitals	**Coefficients**
$\left\|\tilde{nf}_{z^3}(\theta,\phi)\right\rangle$	$\left\|nf_{x(x^2-3y^2)}\right\rangle$	$\sqrt{\frac{5}{8}}\sin^3\theta\cos 3\phi$
	$\left\|nf_{y(3x^2-y^2)}\right\rangle$	$\sqrt{\frac{5}{8}}\sin^3\theta\sin 3\phi$
	$\left\|nf_{z(x^2-y^2)}\right\rangle$	$\frac{\sqrt{15}}{2}\sin^2\theta\cos\theta\cos 2\phi$
	$\left\|nf_{xyz}\right\rangle$	$\sqrt{15}\sin^2\theta\cos\theta\sin\phi\cos\phi$
	$\left\|nf_{xz^2}\right\rangle$	$\frac{1}{2\sqrt{6}}\cdot\left(\sin^3\theta+4\sin 3\theta\right)\cdot\cos\phi$
	$\left\|nf_{yz^2}\right\rangle$	$\frac{1}{2\sqrt{6}}\cdot\left(\sin^3\theta+4\sin 3\theta\right)\cdot\sin\phi$
	$\left\|nf_{z^3}\right\rangle$	$\frac{1}{2}\cdot\left(\cos^3\theta+\cos 3\theta\right)$

Tab. B.5: Rotation of atomic $\left|nf\right\rangle$ orbitals with arbitrary principal quantum number n by polar and azimuthal angles of θ and ϕ, respectively. The rotations are expressed as angle-dependent linear combinations of atomic orbitals that share the same principal and angular momentum quantum numbers n and $l = 3$. The coefficients have been derived by operation of the rotation matrices $\hat{\boldsymbol{R}}_y(\theta)$ and $\hat{\boldsymbol{R}}_z(\phi)$ upon the corresponding orbital.

	Orbitals	**Coefficients**
$\left\|\tilde{nf}_{xz^2}(\theta,\phi)\right\rangle$	$\left\|nf_{x(x^2-3y^2)}\right\rangle$	$\frac{\sqrt{15}}{4}\sin^2\theta\cos\theta\cos 3\phi$
	$\left\|nf_{y(3x^2-y^2)}\right\rangle$	$\frac{\sqrt{15}}{4}\sin^2\theta\cos\theta\sin 3\phi$
	$\left\|nf_{z(x^2-y^2)}\right\rangle$	$\frac{1}{8}\sqrt{\frac{5}{2}}\cdot\left(3\sin 3\theta-\sin\theta\right)\cdot\cos 2\phi$
	$\left\|nf_{xyz}\right\rangle$	$\frac{1}{4}\sqrt{\frac{5}{2}}\cdot\left(3\sin 3\theta-\sin\theta\right)\cdot\sin\phi\cos\phi$
	$\left\|nf_{xz^2}\right\rangle$	$\frac{1}{16}\cdot\left(15\cos 3\theta+\cos\theta\right)\cdot\cos\phi$
	$\left\|nf_{yz^2}\right\rangle$	$\frac{1}{16}\cdot\left(15\cos 3\theta+\cos\theta\right)\cdot\sin\phi$
	$\left\|nf_{z^3}\right\rangle$	$-\frac{1}{8}\sqrt{\frac{3}{2}}\cdot\left(5\sin 3\theta+\sin\theta\right)$
$\left\|\tilde{nf}_{yz^2}(\theta,\phi)\right\rangle$	$\left\|nf_{x(x^2-3y^2)}\right\rangle$	$-\frac{\sqrt{15}}{4}\sin^2\theta\sin 3\phi$
	$\left\|nf_{y(3x^2-y^2)}\right\rangle$	$\frac{\sqrt{15}}{4}\sin^2\theta\cos 3\phi$
	$\left\|nf_{z(x^2-y^2)}\right\rangle$	$-\sqrt{10}\sin\theta\cos\theta\sin\phi\cos\phi$
	$\left\|nf_{xyz}\right\rangle$	$\sqrt{\frac{5}{2}}\sin\theta\cos\theta\cos 2\phi$
	$\left\|nf_{xz^2}\right\rangle$	$\frac{1}{4}\cdot\left(1-5\cos^2\theta\right)\cdot\sin\phi$
	$\left\|nf_{yz^2}\right\rangle$	$-\frac{1}{4}\cdot\left(1-5\cos^2\theta\right)\cdot\cos\phi$
	$\left\|nf_{z^3}\right\rangle$	0
$\left\|\tilde{nf}_{xyz}(\theta,\phi)\right\rangle$	$\left\|nf_{x(x^2-3y^2)}\right\rangle$	$-\sqrt{\frac{3}{2}}\sin\theta\cos\theta\sin 3\phi$
	$\left\|nf_{y(3x^2-y^2)}\right\rangle$	$\sqrt{\frac{3}{2}}\sin\theta\cos\theta\cos 3\phi$
	$\left\|nf_{z(x^2-y^2)}\right\rangle$	$-2\cos 2\theta\sin\phi\cos\phi$
	$\left\|nf_{xyz}\right\rangle$	$\cos 2\theta\cos 2\phi$
	$\left\|nf_{xz^2}\right\rangle$	$\sqrt{\frac{5}{2}}\sin\theta\cos\theta\sin\phi$
	$\left\|nf_{yz^2}\right\rangle$	$-\sqrt{\frac{5}{2}}\sin\theta\cos\theta\cos\phi$
	$\left\|nf_{z^3}\right\rangle$	0

Tab. B.6: Rotation of atomic $\left|nf\right\rangle$ orbitals with arbitrary principal quantum number n by polar and azimuthal angles of θ and ϕ, respectively. The rotations are expressed as angle-dependent linear combinations of atomic orbitals that share the same principal and angular momentum quantum numbers n and $l = 3$. The coefficients have been derived by operation of the rotation matrices $\hat{\boldsymbol{R}}_y(\theta)$ and $\hat{\boldsymbol{R}}_z(\phi)$ upon the corresponding orbital.

	Orbitals	**Coefficients**
$\left\langle \tilde{nf}_{z(x^2-y^2)}(\theta,\phi) \right\vert$	$\left\vert nf_{x(x^2-3y^2)} \right\rangle$	$\sqrt{\frac{3}{8}} \sin\theta \cdot \left(\cos^2\theta + 1 \right) \cdot \cos 3\phi$
	$\left\vert nf_{y(3x^2-y^2)} \right\rangle$	$\sqrt{\frac{3}{8}} \sin\theta \cdot \left(\cos^2\theta + 1 \right) \cdot \sin 3\phi$
	$\left\vert nf_{z(x^2-y^2)} \right\rangle$	$-\frac{1}{2} \cdot \left(\cos\theta - 3\cos^3\theta \right) \cdot \cos 2\phi$
	$\left\vert nf_{xyz} \right\rangle$	$-\left(\cos\theta - 3\cos^3\theta \right) \cdot \sin\phi \cos\phi$
	$\left\vert nf_{xz^2} \right\rangle$	$-\frac{1}{8}\sqrt{\frac{5}{2}} \cdot \left(3\sin 3\theta - \sin\theta \right) \cdot \cos\phi$
	$\left\vert nf_{yz^2} \right\rangle$	$-\frac{1}{8}\sqrt{\frac{5}{2}} \cdot \left(3\sin 3\theta - \sin\theta \right) \cdot \sin\phi$
	$\left\vert nf_{z^3} \right\rangle$	$\frac{\sqrt{15}}{2} \cos\theta \sin^2\theta$
$\left\langle \tilde{nf}_{x(x^2-3y^2)}(\theta,\phi) \right\vert$	$\left\vert nf_{x(x^2-3y^2)} \right\rangle$	$\frac{1}{16} \cdot \left(15\cos\theta + \cos 3\theta \right) \cdot \cos 3\phi$
	$\left\vert nf_{y(3x^2-y^2)} \right\rangle$	$\frac{1}{16} \cdot \left(15\cos\theta + \cos 3\theta \right) \cdot \sin 3\phi$
	$\left\vert nf_{z(x^2-y^2)} \right\rangle$	$-\sqrt{\frac{3}{8}} \sin\theta \cdot \left(\cos^2\theta + 1 \right) \cdot \cos 2\phi$
	$\left\vert nf_{xyz} \right\rangle$	$-\sqrt{\frac{3}{2}} \sin\theta \cdot \left(\cos^2\theta + 1 \right) \cdot \sin\phi \cos\phi$
	$\left\vert nf_{xz^2} \right\rangle$	$\frac{\sqrt{15}}{4} \sin^2\theta \cos\theta \cos\phi$
	$\left\vert nf_{yz^2} \right\rangle$	$\frac{\sqrt{15}}{4} \sin^2\theta \cos\theta \sin\phi$
	$\left\vert nf_{z^3} \right\rangle$	$-\sqrt{\frac{5}{8}} \sin^3\theta$
$\left\langle \tilde{nf}_{y(3x^2-y^2)}(\theta,\phi) \right\vert$	$\left\vert nf_{x(x^2-3y^2)} \right\rangle$	$-\frac{1}{4} \cdot \left(3\cos^2\theta + 1 \right) \cdot \sin 3\phi$
	$\left\vert nf_{y(3x^2-y^2)} \right\rangle$	$\frac{1}{4} \cdot \left(3\cos^2\theta + 1 \right) \cdot \cos 3\phi$
	$\left\vert nf_{z(x^2-y^2)} \right\rangle$	$\sqrt{6} \sin\theta \cos\theta \sin\phi \cos\phi$
	$\left\vert nf_{xyz} \right\rangle$	$-\sqrt{\frac{3}{2}} \sin\theta \cos\theta \cos 2\phi$
	$\left\vert nf_{xz^2} \right\rangle$	$-\frac{\sqrt{15}}{4} \sin^2\theta \sin\phi$
	$\left\vert nf_{yz^2} \right\rangle$	$\frac{\sqrt{15}}{4} \sin^2\theta \cos\phi$
	$\left\vert nf_{z^3} \right\rangle$	0

References

[1] Nobel Media AB 2014, *The Nobel Prize in Physics 1914*, Retrieved 24 July 2018, URL `http://www.nobelprize.org/nobel_prizes/physics/laureates/1914`.

[2] Nobel Media AB 2014, *The Nobel Prize in Physics 1915*, Retrieved 24 July 2018, URL `http://www.nobelprize.org/nobel_prizes/physics/laureates/1915`.

[3] P. Emma, R. Akre, J. Arthur, R. Bionta, C. Bostedt, J. Bozek, A. Brachmann, P. Bucksbaum, R. Coffee, F.-J. Decker, et al., Nat. Photon. **4**, 641 (2010).

[4] T. Ishikawa, H. Aoyagi, T. Asaka, Y. Asano, N. Azumi, T. Bizen, H. Ego, K. Fukami, T. Fukui, Y. Furukawa, et al., Nat. Photon. **6**, 540 (2012).

[5] European XFEL, *Facts and Figures*, Retrieved 24 July 2018, URL `http://www.xfel.eu/facility/overview/facts_amp_figures/index_eng.html`.

[6] Paul Scherrer Institut, *SwissFEL Accelerator*, Retrieved 24 July 2018, URL `https://www.psi.ch/swissfel/swissfel-accelerator`.

[7] D. Arnlund, L. C. Johansson, C. Wickstrand, A. Barty, G. J. Williams, E. Malmerberg, J. Davidsson, D. Milathianaki, D. P. DePonte, R. L. Shoeman, et al., Nat. Methods **11**, 923 (2014).

[8] M. P. Minitti, J. M. Budarz, A. Kirrander, J. Robinson, T. J. Lane, D. Ratner, K. Saita, T. Northey, B. Stankus, V. Cofer-Shabica, et al., Faraday Discuss. **171**, 81 (2014).

[9] M. P. Minitti, J. M. Budarz, A. Kirrander, J. S. Robinson, D. Ratner, T. J. Lane, D. Zhu, J. M. Glownia, M. Kozina, H. T. Lemke, et al., Phys. Rev. Lett. **114**, 255501 (2015).

[10] K. H. Kim, J. G. Kim, S. Nozawa, T. Sato, K. Y. Oang, T. W. Kim, H. Ki, J. Jo, S. Park, C. Song, et al., Nature **518**, 385 (2015).

[11] M. Levantino, G. Schiró, H. T. Lemke, C. Grazia, J. M. Glownia, Z. Diling, M. Chollet, H. Ihee, and A. C. amd M. Cammarata, Nat. Commun. **6**, 6772 (2015).

[12] J. G. Kim, T. W. Kim, J. Kim, and H. Ihee, Accounts Chem. Res. **48**, 2200 (2015).

[13] J. M. Budarz, M. P. Minitti, D. V. Cofer-Shabica, B. Stankus, A. Kirrander, J. B. Hastings, and P. M. Weber, J. Phys. B: At. Mol. Opt. Phys. **49**, 034001 (2016).

[14] K. Haldrup, W. Gawelda, R. Abela, R. Alonso-Mori, U. Bergmann, A. Bordage, M. Cammarata, S. E. Canton, A. O. Dohn, T. B. van Driel, et al., J. Phys. Chem. B **120**, 1158 (2016).

[15] E. Biasin, T. B. van Driel, K. S. Kjær, A. O. Dohn, M. Christensen, T. Harlang, P. Chabera, Y. Liu, J. Uhlig, M. Pápai, et al., Phys. Rev. Lett. **117**, 013002 (2016).

[16] A. A. Zholents and W. M. Fawley, Phys. Rev. Lett. **92**, 224801 (2004).

[17] T. Tanaka, Phys. Rev. Lett. **110**, 084801 (2013).

[18] D. J. Dunning, B. W. J. McNeil, and N. R. Thompson, Phys. Rev. Lett. **110**, 104801 (2013).

[19] E. Prat and S. Reiche, Phys. Rev. Lett. **114**, 244801 (2015).

[20] C. C. Pemberton, Y. Zhang, K. Saita, A. Kirrander, and P. M. Weber, J. Phys. Chem. A **119**, 8832 (2015), URL `http://dx.doi.org/10.1021/acs.jpca.5b05672`.

[21] J. Cao and K. R. Wilson, J. Phys. Chem. A **102**, 9523 (1998).

[22] U. Lorenz, K. B. Møller, and N. E. Henriksen, New J. Phys. **12**, 113022 (2010).

[23] K. B. Møller and N. E. Henriksen, Struct. Bond. **142**, 185 (2012).

[24] T. Northey, N. Zotev, and A. Kirrander, J. Chem. Theory Comput. **10**, 4911 (2014).

[25] G. Dixit, O. Vendrell, and R. Santra, Proc. Natl. Acad. Sci. U.S.A. **109**, 11636 (2012).

[26] M. Ben-Nun, T. J. Martínez, P. M. Weber, and K. R. Wilson, Chem. Phys. Lett. **262**, 405 (1996).

[27] M. Ben-Nun, J. Cao, and K. R. Wilson, J. Phys. Chem. A **101**, 8743 (1997).

[28] S. Bratos, F. Mirloup, R. Vuilleumier, and M. Wulff, J. Chem. Phys. **116**, 10615 (2002).

[29] N. E. Henriksen and K. B. Møller, J. Phys. Chem. B **112**, 558 (2008).

[30] U. Lorenz, K. B. Møller, and N. E. Henriksen, Phys. Rev. A **81**, 023422 (2010).

[31] G. Dixit and R. Santra, J. Chem. Phys. **138**, 134311 (2013).

[32] M. Kowalewski, K. Bennett, and S. Mukamel, Struct. Dyn. **4**, 054101 (2017).

[33] K. Bennett, M. Kowalewski, J. R. Rouxel, and S. Mukamel, Proc. Natl. Acad. Sci. U.S.A. **115**, 6538 (2018).

[34] J. M. Glownia, A. Natan, J. P. Cryan, R. Hartsock, M. Kozina, M. P. Minitti, S. Nelson, J. Robinson, T. Sato, T. van Driel, et al., Phys. Rev. Lett. **117**, 153003 (2016).

[35] K. Bennett, M. Kowalewski, and S. Mukamel, Phys. Rev. Lett. **119**, 069301 (2017).

[36] J. M. Glownia, A. Natan, J. P. Cryan, R. Hartsock, M. Kozina, M. P. Minitti, S. Nelson, J. Robinson, T. Sato, T. van Driel, et al., Phys. Rev. Lett. **119**, 069302 (2017).

[37] G. Dixit and R. Santra, Phys. Rev. A **96**, 053413 (2017).

[38] F. Schnaidt, Annalen der Physik **413**, 89 (1934).

[39] J. J. Sakurai, *Advanced Quantum Mechanics* (Addison-Wesley Publishing Company, 1967), pp. 32, 36, 39–41.

[40] J. J. Sakurai, *Modern Quantum Mechanics* (Addison-Wesley Publishing Company, 1994), pp. 325-332.

[41] J. Als-Nielsen and D. McMorrow, *Elements of Modern X-ray Physics* (John Wiley & Sons, 2011), pp. 11–13, 290, 345–347, 355–359.

[42] S. P. Hau-Riege, *Nonrelativistic Quantum X-Ray Physics* (Wiley-VCH, 2015), pp. 149–150, 263–264.

[43] S. P. A. Sauer, *Molecular Electromagnetism: A Computational Chemistry Approach* (Oxford University Press, 2011), pp. 44–47.

[44] R. Loudon, *The Quantum Theory of Light* (Oxford University Press, 2000), pp. 57–60, 95, 139–141, 148, 173–177, 374–375.

[45] C. Cohen-Tannoudji, J. Dupont-Roc, and G. Grynberg, *Atom-Photon Interactions: Basic Processes and Applications* (Wiley-VCH, 2004), pp. 139, 380, 626–627, 527–529.

[46] C. Cohen-Tannoudji, J. Dupont-Roc, and G. Grynberg, *Photons and Atoms: Introduction to Quantum Electrodynamics* (Wiley-VCH, 1997), pp. 171–173, 184–188.

[47] T. Helgaker, P. Jørgensen, and J. Olsen, *Molecular Electronic-Structure Theory* (John Wiley & Sons, 2012), pp. 64–66.

[48] E. Prince, *International Tables for Crystallography, Volume C: Mathematical, Physical and Chemical Tables* (Kluwer Academic Publishers, 2004), p. 554.

[49] I. Waller and D. R. Hartree, P. R. Soc. Lond. A **124**, 119 (1929).

[50] G. Friedel, C. R. Hebd. Acad. Sci. **157**, 1533 (1913).

[51] H. A. Bethe and E. E. Salpeter, *Quantum Mechanics of One- and Two-Electron Atoms* (Springer, 1957).

[52] M. Abramowitz and I. A. Stegun, *Handbook of Mathematical Functions* (Dover Publications, 1964).

[53] V. Devanathan, *Angular Momentum Techniques in Quantum Mechanics* (Springer, 1999).

[54] D. A. Varshalovich, A. N. Moskalev, and V. K. Khersonskii, *Quantum Theory of Angular Momentum* (World Scientific, 1988).

[55] A. Erdélyi, W. Magnus, F. Oberhettinger, and F. G. Tricomi, *Tables of Integral Transforms Vol. I* (McGraw-Hill, 1954).

[56] M. Simmermacher, N. E. Henriksen, and K. B. Møller, Phys. Chem. Chem. Phys. **19**, 19740 (2017).

[57] H.-J. Werner and P. J. Knowles, J. Chem. Phys. **82**, 5053 (1985).

[58] P. J. Knowles and H.-J. Werner, Chem. Phys. Lett. **115**, 259 (1985).

[59] T. H. Dunning, J. Chem. Phys. **90**, 1007 (1989).

[60] D. E. Woon and T. H. Dunning, J. Chem. Phys. **100**, 2975 (1994).

[61] H.-J. Werner, P. J. Knowles, G. Knizia, F. R. Manby, and M. Schütz, WIREs Comput. Mol. Sci. **2**, 242 (2012).

[62] H.-J. Werner, P. J. Knowles, G. Knizia, F. R. Manby, M. Schütz, P. Celani, W. Györffy, D. Kats, T. Korona, R. Lindh, et al., *Molpro, version 2015.1, a package of ab initio programs* (2015), see http://www.molpro.net.

[63] J. A. Fleck, J. R. Morris, and M. D. Feit, Appl. Phys. **10**, 129 (1976).

[64] M. D. Feit, J. A. Fleck, and A. Steiger, J. Comput. Phys. **47**, 412 (1982).

[65] B. Schmidt and U. Lorenz, Comput. Phys. Commun. **213**, 223 (2017).

[66] D. Kosloff and R. Kosloff, J. Comput. Phys. **52**, 35 (1983).

[67] A. R. Bainbridge, J. Harrington, A. Kirrander, C. Cacho, E. Springate, W. A. Bryan, and R. S. Minns, New J. Phys. **17**, 103013 (2015).

[68] L. Wolniewicz, J. Chem. Phys. **103**, 1792 (1995).

[69] G. Staszewska and L. Wolniewicz, J. Mol. Spectrosc. **212**, 208 (2002).

[70] L. Wolniewicz and G. Staszewska, J. Mol. Spectrosc. **217**, 181 (2003).

[71] L. Wolniewicz, T. Orlikowski, and G. Staszewska, J. Mol. Spectrosc. **238**, 118 (2006).

[72] A. M. Carrascosa and A. Kirrander, Phys. Chem. Chem. Phys. **19**, 19545 (2017).

[73] L. Wolniewicz and K. Dressler, J. Chem. Phys. **100**, 444 (1994).

[74] L. Wolniewicz, J. Mol. Spectrosc. **169**, 329 (1995).

[75] L. Wolniewicz and G. Staszewska, J. Mol. Spectrosc. **220**, 45 (2003).

[76] H.-J. Werner and P. J. Knowles, J. Chem. Phys. **89**, 5803 (1988).

[77] P. J. Knowles and H.-J. Werner, Chem. Phys. Lett. **145**, 514 (1988).

[78] P. J. Knowles and H.-J. Werner, Theor. Chim. Acta **84**, 95 (1992).

[79] K. Kaufmann, W. Baumeister, and M. Jungen, J. Phys. B: At. Mol. Opt. Phys. **22**, 2223 (1989).

[80] E. Biasin, T. B. van Driel, K. S. Kjær, A. O. Dohn, M. Christensen, T. Harlang, P. Chabera, Y. Liu, J. Uhlig, M. Pápai, et al., Phys. Rev. Lett. **117**, 013002 (2016).

[81] E. Biasin, T. B. van Driel, G. Levi, M. G. Laursen, A. O. Dohn, A. Moltke, P. Vester, F. B. K. Hansen, K. S. Kjaer, T. Harlang, et al., J. Synchrotron Radiat. **25**, 306 (2018).

[82] J. S. Baskin and A. H. Zewail, ChemPhysChem **7**, 1562 (2010).